

Compliant 3D Hydrogel Bead Scaffolds to Study Cell Migration and Mechanosensitivity *in vitro*

Dissertation

zur Erlangung des akademischen Grades Doktoringenieur (Dr.-Ing.)

vorgelegt an der
Technischen Universität Dresden
Fakultät Maschinenbau und Verfahrenstechnik

eingereicht von

Katrin Wagner

geboren am 14.04.1988 in Rostock

Betreuende Hochschullehrer und Gutachter:

Prof. Dr. Thomas Bley

Prof. Dr. Jochen Guck

Prof. Dr. Katja Bühler

Dresden, den 13.04.2018

“So the Patrician never planned. Plans often got in the way.”

Terry Pratchett – Jingo

Zusammenfassung

Gewebe sind nicht nur durch ihre biochemische Zusammensetzung definiert, sondern auch durch ihre individuellen mechanischen Eigenschaften. Inzwischen ist es weithin akzeptiert, dass Zellen ihre mechanische Umgebung spüren und darauf reagieren. Zum Beispiel werden Zellmigration und die Differenzierung von Stammzellen durch die Umgebungssteifigkeit beeinflusst. Um diese Effekte *in vitro* zu untersuchen, wurden viele Zellkulturstudien auf 2D Hydrogelsubstraten durchgeführt. Zusätzlich dazu steigt die Anzahl von Studien an, die hydrogelbasierte 3D-Scaffolds nutzen, um 2D Studien zu validieren und die experimentellen Bedingungen der Situation *in vivo* anzunähern. Jedoch erweist es sich weiterhin als schwierig den Effekt von Mechanik in 3D *in vitro* zu untersuchen, da in den gemeinhin genutzten 3D Hydrogelsystemen immer eine Kopplung zwischen Gelporosität und Steifigkeit besteht. Zusätzlich hängt die Konzentration der biologisch aktiven Bindungsstellen für Zellen oft ebenfalls von der Steifigkeit ab.

Diese Arbeit präsentiert die Entwicklung und Optimierung neuer 3D Hydrogelkugel-Scaffolds, in denen die Steifigkeit von der Porosität schließlich entkoppelt wird. Mit Hydrogelkugeln als Scaffold-Bausteine ist es nun möglich 3D Scaffolds mit definierten mechanischen Eigenschaften und konstanter Porengröße zu generieren. Während der Methodenentwicklung wurden verschiedene Prinzipien und Kultivierungskammern konstruiert und überarbeitet, gefolgt von der theoretischen Betrachtung der Sauerstoffdiffusion, um die Eignung der gewählten Kammer hinsichtlich Zellvitalität und Zellwachstum zu überprüfen. Eine Kombination aus mehreren getesteten Filtern wurde ausgewählt um Hydrogelkugel-Scaffolds erfolgreich in der ausgewählten Kammer zu generieren. Im Weiteren wurden verschiedene Hydrogelmaterialien untersucht hinsichtlich der erfolgreichen Produktion monodisperser Hydrogelkugeln und der Erzeugung stabiler Scaffolds. Hydrogelkugeln aus Polyacrylamid (PAAm) wurden als Scaffold-Bausteine ausgewählt um damit die Eignung des entwickelten Systems zu demonstrieren lebende Zellen zu mikroskopieren. Außerdem wurde das Überleben von Fibroblasten über vier Tage in unterschiedlich steifen Hydrogelkugel-Scaffolds erfolgreich gezeigt. Weiterhin war es möglich erste Zellmigrationsexperimente durchzuführen. Dafür wurden sowohl einfache PAAm-Hydrogelkugeln als auch mit Adhäsionsmolekülen funktionalisierte Hydrogelkugeln genutzt, um unterschiedlich steife Schichten in einem Scaffold zu erzeugen. Dadurch war es möglich nicht nur Zellmigration anhand von Zelladhäsion in 3D Scaffolds mit Steifigkeitsgradienten zu beobachten, sondern auch Zellmigration ohne Zelladhäsion.

Abstract

Tissues are defined not only by their biochemical composition, but also by their distinct mechanical properties. It is now widely accepted that cells sense their mechanical environment and respond to it. For example, cell migration and stem cell differentiation is affected by stiffness. To study these effects *in vitro*, many cell culture studies have been performed on 2D hydrogel substrates. Additionally, the amount of 3D studies based on hydrogels as 3D scaffold is increasing to validate 2D *in vitro* studies and adjust experimental conditions closer to the situation *in vivo*. However, studying the effects of mechanics *in vitro* in 3D is still challenging as commonly used 3D hydrogel assays always link gel porosity with stiffness. Additionally, the concentration of biologically active adhesion sides often also depends on the stiffness.

This work presents the development and optimization of novel 3D hydrogel bead scaffolds where the stiffness is finally decoupled from porosity. With hydrogel beads as scaffold building blocks it was possible to generate 3D scaffolds with defined mechanical properties and a constant pore size. During the method development, different culture devices were constructed and revised, followed by oxygen diffusion simulations to proof the suitability of the chosen device for cell survival and growth. A combination of different filter approaches was selected to generate hydrogel bead scaffolds in the culture device. Furthermore, different hydrogel materials were investigated regarding successful production of monodisperse beads and stable scaffold generation. Polyacrylamide (PAAm) hydrogel beads were chosen as scaffold building blocks to demonstrate live-cell imaging and successful cell survival over four days in differently compliant hydrogel bead scaffolds. Moreover, first cell migration experiments were performed by using plain PAAm hydrogel beads as well as PAAm hydrogel beads functionalized with adhesion molecules with differently stiff layers in one scaffold. Thereby fibroblast migration was observed not only in adhesion-dependent migration manner, but also in an adhesion-independent mode.

List of publications resulting from work of this thesis

Traeber N, Uhlmann K, Girardo S, Kesavan G, Wagner K, Friedrichs J, Goswami R, Bai K, Brand M, Werner C, Balzani D, Guck J.: **Polyacrylamide Bead Sensors for in vivo Quantification of Cell-Scale Stress in Zebrafish Development.** *bioRxiv* 2018, doi: <https://doi.org/10.1101/420844>

Girardo S, Traeber N, Wagner K, Cojoc G, Herold C, Goswami R, Schlüßler R, Abuhattum S, Taubenberger A, Reichel F, Mokbel D, Herbig M, Schuermann M, Mueller P, Heida T, Jacobi A, Ulbricht E, Thiele J, Werner C & Guck J.: **Standardized microgel beads as elastic cell mechanical probes.** *J. Mater. Chem. B* **6**: 6245–6261(2018), doi: <http://dx.doi.org/10.1039/C8TB01421C>

Rosendahl P, Plak K, Jacobi A, Kraeter M, Toepfner N, Otto O, Herold C, Winzi M, Herbig M, Ge Y, Girardo S, Wagner K, Baum B & Guck J.: **Real-time fluorescence and deformability cytometry.** *Nature Methods* **15**: 355–358 (2018), doi: <http://dx.doi.org/10.1038/nmeth.4639>.

Acknowledgements

First of all, I want to thank my supervisor Jochen Guck as he offered to me this project. Together with the project idea and lots of input, he made my development and my independent work possible and supported me all the time. He was always open for problems and pointed me into important directions when I struggled.

I want to thank Nicole Träber for her passion and our shared story with the hydrogel beads. It made this tragicomedy worth it and without her help I would have not reached this point of submitting the thesis. She was such an amazing help in the AFM work and worked a lot on the stiffness characterization of hydrogel beads. Sharing and discussing ideas and problems as well as writing together a manuscript was always a pleasure and the support we gave each other was so great.

A very big thank you goes to Salvatore Girardo. With his amazing microfluidic knowledge and passion to generate suitable hydrogel beads, he was making this work possible at all. Without him, I would have never reached the point of generating successful scaffolds within these five years of thesis work. He was always open for ideas and discussions, shared his knowledge and introduced me to the field of polymer theory and droplet generation.

Big thanks also to Ruchi Goswami, who produced all the PAAm hydrogel beads I needed during the last year of work.

I want to thank Philipp Rosendahl for performing the RT-fDC measurements.

I also thank Robert Stange and Tim Lauterbach for their input and help with the oxygen simulations and the implementation into COMSOL.

I thank my TAC members Carsten Werner, Gerd Kempermann and Thomas Bley for their support, ideas and discussions. I also thank Thomas Bley for his official supervision and realising my wish to submit my work at the engineering faculty.

I thank Paul Müller for his help and support for the PMMA scaffold characterization. By writing a Python script, he made this part so much easier. Over three years sharing an office, he never complained about my habits and was great company.

Special thanks go to Elke Ulbricht, as she always had an open ear not only for my biological questions, but also for any other struggles, problems, needs of feedback and discussion points. Sharing an office was so much fun and our shared love to the same books and authors made it very special for me.

I want to thank the whole Guck Lab for all their input, suggestions, discussions, distractions and making the time during the thesis work worth it. Without them, the hard times in the lab would not have been vanished in the large amounts of great memories. It is so amazing when colleagues evolve to friends.

Thanks to all my friends and family members as they were always supportive and made my life to the life I love. I especially thank my parents who supported me all my life time and made everything possible I did by their undistracted love and believe in me.

Very special thanks go to my beloved husband Oli and to my son Maurice who were always calm and supportive, when I had a hard time. They made me laugh and always came up with something to cheer me up. They were always understanding and made my life so much easier and brighter, especially in the last months. Thanks for all your love!

Table of Content

1	Introduction.....	1
1.1	Mechanics play a role in biology	1
1.2	3D cultures and scaffolds	2
1.3	3D hydrogel systems to study effects of mechanics	4
1.4	Decoupling stiffness and porosity in 3D scaffolds	7
2	Materials	9
3	Methods	12
3.1	Laser scanning microscopy and microscopy data processing	12
3.2	Atomic force microscopy (AFM)	12
3.3	Refractive index matching of PMMA beads.....	14
3.4	Regular PMMA bead scaffolds for developing analysis algorithm.....	14
3.5	Cell culture standards	15
3.6	Fluorescent labelling of ULGP agarose	16
3.7	Production of polydisperse ULGP agarose beads	17
3.8	Hydrogel bead production via microfluidics.....	19
3.9	PAAm bead functionalization	20
3.10	Real-time fluorescence and deformability cytometry (RT-fDC).....	21
3.11	3D scaffolds made from hydrogel beads	22
3.12	Statistics.....	31
4	Results.....	32
4.1	Design of a suitable scaffold device.....	32
4.2	Theoretical oxygen supply in 3D culture system is sufficient for cell survival and proliferation	35
4.3	Further optimization of 3D scaffold device.....	41
4.3.1	PMMA beads can be arranged in stable scaffolds.....	41
4.3.2	Regular PMMA bead scaffolds can be achieved and analysed	44
4.3.3	PMMA bead scaffolds and agarose bead scaffolds act as combined filter to stack up hydrogel beads.....	47
4.4	PAAm hydrogel beads produced by microfluidics are suitable to create compliant 3D scaffolds.....	49
4.5	Reproducible, regular and stable 3D scaffolds made of hydrogel beads	56
4.6	NIH-3T3/GFP cell migration within 3D hydrogel bead scaffolds	64
5	Discussion and Concluding Remarks	71
6	Bibliography	79
	List of Figures	87

List of Tables	92
Eigenständigkeitserklärung	93
Appendix A	1
Appendix B	1
FIJI macro for FFT analysis maxima:.....	1
Python script to determine regularity of PMMA bead scaffolds.....	2
Excel macro to determine number of peaks for regularity analysis	19

1 Introduction

Progress in engineering and development is always driven by new ideas, the spirit to perform better or the will to understand mechanisms and procedures in detail, and thereby leads to a continuous evolution of new methods and systems in every research field. Every time a field is evolving based on new insights, novel connections are made and existing ones are developed. This goes together with the development and optimization of established and new technologies.

Such evolution is also now happening in the interdisciplinary fields of biology, biophysics, polymer chemistry and material science with respect to the mechanical properties of biological systems and how to study and use its parameters, effects and outcomes.

With the newly developed method of compliant 3D hydrogel bead scaffolds presented in this thesis, a contribution to the fast-evolving field is made to promote further understandings of mechanosensitivity in biology.

1.1 Mechanics play a role in biology

Over the last decades, researchers investigated intensively if and how cells and tissue stiffness is altered during diseases, how this affects processes like wound healing and regeneration and how important mechanical properties are for biological processes. It is now starting to get accepted that tissue stiffness is an additional important key player for biological processes as migration, differentiation and proliferation [1–3].

It has been shown that cells sense their mechanical environment and respond to it, a process also called “mechanosensing”. Stem cells differentiated into neurogenic lineage or into myogenic lineage when cultured on collagen-coated substrates with stiffness comparable to the respective tissue [1]. Fibroblasts demonstrated directional migration towards stiffer polyacrylamide substrates [2] and inflammatory response was increased with higher stiffness [4]. These are just some examples of the increasing amount of performed studies about effects of substrate stiffness and mechanisms of mechanosensing *in vitro* and *in vivo*.

In order to survey *in vivo* cell behaviour reproducible together with limiting animal experiments as well as to simulate the *in vivo* situation, different 2D and 3D *in vitro* cell culture systems have been developed. Using 2D systems (i.e. growing cells on plane substrates) is often less cost intensive and relatively easy in performance. However, they might simplify the *in vivo* situation too much and can introduce artefacts [5–7]. Thus, the observed cell behaviour might not reflect the natural situation [8]. To overcome this issue and to converge *in vitro* closer to *in vivo*, the third dimension can be introduced to the 2D systems [9]. By this, the complexity

1.2 3D cultures and scaffolds

of *in vitro* cell culture systems is increased and still various of existing *in vivo* interactions can be decoupled and studied independently *in vitro*. These advantages lead to an increasing amount of different 3D *in vitro* model systems to address diverse questions [10–13], e.g. mechanosensitivity in 3D [14].

1.2 3D cultures and scaffolds

Three-dimensional cultures in its variants have been used for more than a century, initially driven by the motivation to understand organogenesis [13]. Based on technical advances and the understanding of the importance of 3D for functional cells and tissues, mimicking the third dimension is under intensive development, especially in the field of tissue engineering [9,15]. Components of the *in vivo* 3D microenvironment are extracellular matrix (ECM), neighbouring cells as well as different soluble factors [16]. The interlinked factors of a complex cell-laden *in vivo* microenvironment are shown in Figure 1. The orange-coloured parts illustrate different parameters that are involved in the mechanical status of the microenvironment, whereas the blue-coloured areas mark other factors that can guide cell function [6,14–18]. The individual effects on cell function are in this complexity hard to identify, as previously mentioned [18]. Thus, 3D *in vitro* model systems are chosen to study how one factor, e.g. stiffness, or a defined combination of several factors is affecting cell function.

To generate a functional 3D culture model, it is important to take into account certain engineering parameters [7,19]. To provide a third dimension for cells *in vitro*, a scaffold as support structure is needed. First, a suitable scaffold material has to be chosen. The biomaterial needs to be biocompatible and should provide tuneable mechanical (e.g. stiffness) and (bio)chemical properties (e.g. adhesion sites) similar to the *in vivo* microenvironment. Other important attributes are porosity and permeability of the scaffold to ensure transport of nutrients, waste and oxygen as well as cell spreading and growth.

1.2 3D cultures and scaffolds

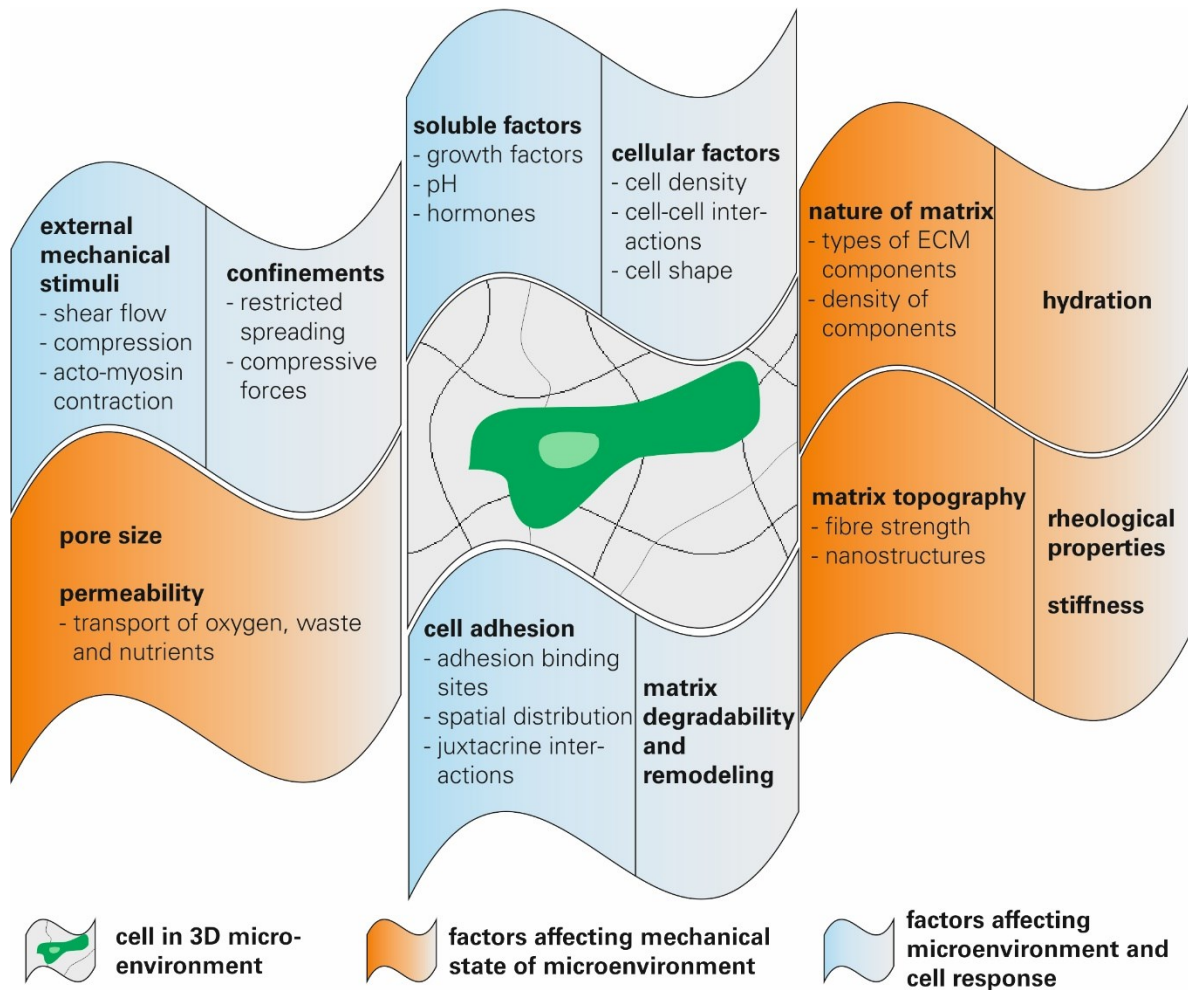


Figure 1: Schematic representation of various biochemical and mechanical parameters that characterize the complex *in vivo* microenvironment of cells. The parameters are interacting with each other and represent cues to guide cell function [6,14–18]. The orange-coloured parts illustrate the parameters affecting the mechanical properties of the microenvironment, whereas the blue-coloured parts label other factors guiding cell function.

Possible biomaterials, that were already used as in stem cell research and tissue engineering, cover a broad range of materials. Biomaterials can be metals, ceramics, inorganic porous materials (e.g. graphene foams, carbon nanotubes) as well as polymers. Within the polymers, it is differentiated between natural polymers (e.g. gelatin, laminin, chitosan, alginate, collagen, hyaluronic acid) and synthetic polymers (e.g. polyurethane, poly(ethylene glycol), polylactic acid, polyglycolic acid) [7,20–23]. For most tissues and cells polymer hydrogels are seen as a highly suitable biomaterial for *in vitro* studies. Hydrogels are biocompatible, can be functionalized with (bio)chemical molecules, are porous and provide a certain permeability. It is also possible to adjust the mechanical properties of hydrogels, which is one of the major key points to study mechanosensitivity [8].

1.3 3D hydrogel systems to study effects of mechanics

Hydrogels are defined as three-dimensional polymeric networks that swell in water [24]. Based on their tuneable stiffness in combination with the possibility to adjust (bio)chemical properties, they have been the material of choice for multiple mechanosensitivity studies.

Available hydrogel systems can be divided into natural ones (e.g. collagen, Matrigel, agarose and fibrin), synthetic ones (e.g. poly(ethylene glycol) (PEG), polyacrylamide (PAAm)) and hybrid materials that combine the first two [25–27]. Table 1 summarizes reported advantages and disadvantages researchers have to consider when choosing the appropriate hydrogel system for their study. Lee et al. reviewed in 2017 numerous natural and synthetic hydrogel systems regarding positive and negative aspects as well as their use as 3D model applications [8,25,28].

Natural hydrogels like collagen, agarose and gelatine are biocompatible and bioactive. By their presentation of endogenous factors, they can promote cell adhesion and cell function. However, depending on the type of hydrogel, it might result in limited cell adhesion, unwanted degradation processes or contractions. Tuning of the hydrogels' mechanical properties to cover a broad range of stiffness can be challenging. Due to their complexity as natural polymer systems, it can be difficult to determine the acting signal for the observed cell behaviour. Based on the natural source, batch-to-batch variabilities can occur resulting in different cell responses for the same system.

Table 1: Summarized advantages and disadvantages of natural and synthetic hydrogels as scaffolds for 3D *in vitro* cell culture models. Lee et al. listed these for individual hydrogels [8,25,28]

	Natural hydrogels	Synthetic and hybrid hydrogels
+	biocompatible, bioactive present endogenous factors degradation possible	highly reproducible simple tuning of mechanics modification with additional biologically active molecules possible
-	complex, sometimes ill-defined tuning of mechanics & possible range can be difficult batch-to-batch variability too fast degradation or unwanted contraction possible	lack endogenous factors appropriate formation process must be chosen to avoid creation of damaging molecules non-degradability possible degradation products might be toxic might be cytotoxic

Synthetic hydrogel systems as PAAm or PEG are reported to be highly reproducible. Their mechanical properties can be tuned in simple ways and cover a broad range. They can be modified by addition of molecules for adhesion and degradation or with growth factors to enhance their biocompatibility. Some synthetic hydrogels lack endogenous factors or might

1.3 3D hydrogel systems to study effects of mechanics

be non-degradable. On the other side, synthetic hydrogels might be cytotoxic or products resulting from the formation or degradation process might result in cell damaging molecules. Many hydrogel systems (2D and 3D) have been evolved for mechanosensitivity studies over the last decades, resulting in an increased amount of data on observed effects of hydrogel mechanics on cell behaviour for different hydrogels and various cell types. It has been demonstrated that human mesenchymal stem cells cultured on differently stiff PAAm substrates (coated with collagen) differentiated into different lineages (neurogenic: 0.1 – 1 kPa; myogenic: 8 – 17 kPa; osteogenic: 25 – 40 kPa) [1]. When human mesenchymal stem cells were grown in differently stiff 3D collagen-hyaluronic acid-scaffolds, the cells differentiated into glial (10 kPa) or neuronal (1 kPa) lineages [29]. Another study illustrated that also murine embryonic stem cells differentiated into glial and neuronal lineages when cultured in different 3D scaffolds and highlighted the large impact of matrix type (i.e gelatine, collagen, hyaluronic acid), composition, stiffness combined with concentration and type of used signalling molecules on the differentiation outcome [30].

Fibroblasts demonstrated durotactic behaviour on PAAm substrates (coated with collagen), meaning they migrated towards the stiff area of the prepared 2D hydrogels [2]. Also in 3D collagen gels fibroblasts migrated towards stiffer regions reproducing the durotactic behaviour also in 3D [31]. Another study using fibroblasts illustrated with 3D alginate hydrogels the effect of additional adhesion components on cellular behaviour. By complementing alginate hydrogels with Matrigel and generating RGD-conjugated alginate hydrogels respectively, it was possible to change the fibroblast migration mode from mesenchymal migration (Matrigel) to amoeboid migration (RGD-conjugates) for comparable stiffness ranges. Additionally, compliant scaffolds led to fibroblast elongation and stiffening of the gel led to inhibition of elongation independently of the used hydrogels [32].

Mouse preosteoblasts were cultured in 3D PEG hydrogels with matrix metalloproteases (MMP) sensitive and insensitive linkers to form degradable and non-degradable hydrogels respectively. It was demonstrated that 3D cell migration depended on biochemical (MMP degradable or not) and biophysical properties. Migration speed was decreased with increasing stiffness, more for non-degradable than for degradable hydrogels [33].

When studying neuronal cells on different stiff 2D PAAm substrates coated with laminin, it was demonstrated that astrocytes were small and lacked stress fibres on compliant PAAm substrates but showed highly spread morphology on stiff ones. Neurons grew well on compliant PAAm substrates and had 30% more F-actin structures compared to the stiff PAAm substrates. However, neurite outgrowth showed only insignificant differences when grown

1.3 3D hydrogel systems to study effects of mechanics

on the stiffer hydrogels. [34]. Others published that neurite branching decreased with increasing stiffness on 2D PAAm substrates coated with Matrigel [35] and the elongation of chick dorsal root ganglia was lower in stiffer 3D agarose hydrogels than in compliant ones [36]. For an even deeper insight, several reviews can be recommended [14,18,25,27,37].

Taken the published observations in mechanosensitivity studies together, it is clear that cell behaviour is affected among others by the mechanics of the microenvironment. However, due to the large variety and complexity of available 3D *in vitro* models, it is a big challenge to figure out the underlying mechanisms as well as the effect explicitly evoked by mechanical changes.

One important challenge while studying the effect of mechanics on cell behaviour is the coupling of stiffness with porosity and adhesion binding sites (Figure 2), that has been described in detail by Trappmann and Chen in 2013 [26].

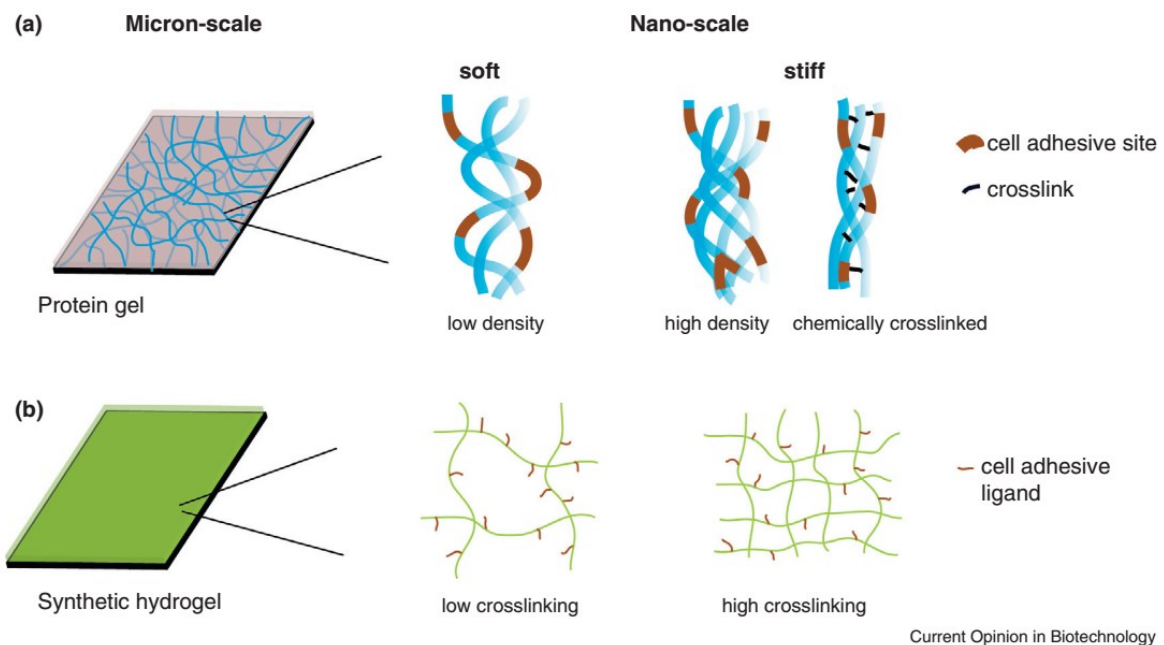


Figure 2: “Structural features of protein gels (a) and synthetic hydrogels (b) at the micron-scale and nano-scale. Substrate mechanics influence matrix density, ligand availability (a) and hydrogel pore size (b).” Reprinted from [26].

While in natural gels a stiffness increase is a result of either a higher crosslinking ratio or a higher protein concentration together with an elevated amount of cell adhesion sites, stiffer synthetic gels can be generated by an increase of their crosslinking ratio while keeping the cell adhesion sites constant. Shan et al. extensively reviewed possibilities how mechanics can now be changed independently from functional adhesive sites for different hydrogel systems. However, there is very often a change in pore size of the polymer network while

adjusting the stiffness. This entanglement makes it hard to identify the explicit effect of mechanics on cells [8,25,26,38].

1.4 Decoupling stiffness and porosity in 3D scaffolds

The need to decouple the effects of porosity and scaffold mechanics on cell behaviour is now evident and ways of decoupling are developed to generate scaffolds with constant porosity and tuneable stiffness. In 2010 da Silva et al. extended rigid inverted colloidal crystal scaffolds [39,40] into inverted colloidal crystals made from PAAm hydrogels. Thereby scaffolds were generated that were able to be used for mechanosensitivity studies [41]. These inverse colloidal crystals still come with some challenges: mainly static cultures are possible, the scaffold is relatively small and layers of different stiffness in one scaffold are hard to achieve. Another approach to decouple porosity and stiffness is to use colloidal crystals directly as

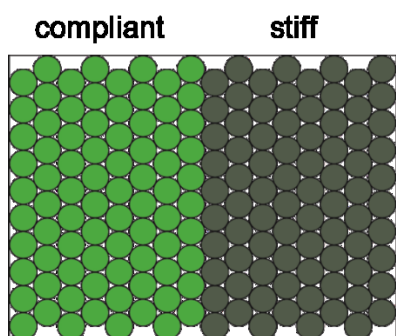


Figure 3: Scaffolds generated from hydrogel beads as building blocks with different mechanical properties but same diameter.

scaffold. By using beads of same size but with different mechanical properties as scaffold building blocks, a differently stiff microenvironment can be built, where the constant microporous voids between the microbeads served as growth volume for cells (Figure 3).

Pautot et al. published in 2008 a possible approach to use rigid silica beads as scaffold building blocks for 3D neuronal networks. The authors generated bead-neuron-scaffolds by repeatedly adding silica beads and neurons into a cavity making use of the self-arrangement of monodisperse particles in solution [42]. However, these scaffolds were only stable due to the cellular network. The silica beads were not additionally annealed with each other to form a steady scaffold. To generate stable scaffolds as *in vitro* models, microbeads would either have to be trapped into a confined space or annealed in some way. Since almost two decades microbead scaffolds have been used in tissue regeneration, especially, but not exclusively in bone regeneration. It turned out that one of the biggest challenges was (and still is) annealing of the beads [20,43]. The group of Tatiana Segura extended approaches of microbead sintering as well as hydrogel bead production and utilizing them as scaffold building blocks [44] to combine them into covalently linked 3D hydrogel scaffolds as injectable scaffolds for wound healing applications [45]. To the best knowledge, this was the first direct decoupling of scaffold stiffness and porosity by generating microporous annealed particle (MAP) scaffolds from PEG [45]. The microbeads were produced by microdroplet formation in a microfluidic device. In the following two years, they demonstrated their ability to form annealed hydrogel bead scaffolds from hyaluronic acid

1.4 Decoupling stiffness and porosity in 3D scaffolds

hydrogels to enhance the application capacity in tissue regeneration of their injectable hydrogel bead scaffolds [46,47]. By using hydrogel as microbead material, it was possible to cover the tissue-specific stiffness ranges necessary for wound healing applications. However, the focus of this group lies on tissue engineering and they demonstrated the biocompatibility of the system *in vitro* with fibroblasts.

To use this approach for more complex questions as to unravel the mechanosensitivity mechanisms *in vitro* in detail, the published system would need further extensions. The possible stiffness range as well as the annealing behaviour with changing mechanical properties were not determined so far and the generation of differently stiff layers within one scaffold was not established. Thus, there is a need for an advanced 3D *in vitro* hydrogel system that decouples porosity and stiffness.

Independent from the work of Tatiana Segura and colleagues, the here presented compliant 3D hydrogel bead scaffolds was developed, optimized and characterized to provide a method to perform mechanosensitivity studies *in vitro*. The methodical approach to generate 3D hydrogel bead scaffolds by using monodisperse hydrogel beads with tuneable stiffness as scaffold building blocks, resulted in *in vitro* scaffolds with the possibility to form layers of different stiffness within one scaffold (as depicted in Figure 3). Thereby, an advanced 3D hydrogel bead scaffold was built where stiffness and porosity was finally decoupled.

Now the effects of stiffness on cell behaviour can be investigated independently from porosity. The system provides scaffold layers of different mechanical properties and thereby an additional advanced method to unravel the complex mechanisms behind mechanosensitivity. Furthermore, the possibility of different ways of culturing cells (i.e. static and dynamic cell cultures) favours a broad field of applications. For example, it will be possible to rebuild tissue structures in their mechanical features to investigate developmental or regeneration processes *in vitro* as well as to study migration processes within defined compliant 3D scaffolds.

2 Materials

Table 2: General materials

Name	Company	Order No.
10 mM MEM non-essential Amino Acids (MEMNEAA)	life technologies	11140-035
1H,1H,2H,2H-Perfluoro-1-octanol (PFO)	Sigma Aldrich Chemie GmbH	370533-25G
2,2-Thiodiethanol (TDE)	Sigma Aldrich Chemie GmbH	88561-1L
absolute Ethanol (absolute EtOH)	VWR	1117272500
accutase	life technologies	A6967-100ML
acrylamide (AAM)	Sigma Aldrich Chemie GmbH	A8887
acrylic acid N-hydroxysuccinimide ester, \geq 90% (NHS)	Sigma Aldrich Chemie GmbH	A8060
agarose (Type IX Ultra-low Gelling Temperature) (ULGP agarose)	Sigma Aldrich Chemie GmbH	A5030-5G
AlexaFluor®488 hydrazide (1 mg)	Life technologies ("molecular probes")	A30634
ammonium persulphate (APS)	GE Healthcare	17131101
Aquapel®	Pittsburgh Glass Works LLC	
Blasticidin	life technologies	R210-01
bovine serum albumine (BSA)	Sigma Aldrich Chemie GmbH	A7906-100G
CellTak, Cell and Tissue Adhesive	Fisher Scientific	CB-40240
DMEM (high glucose), no pyruvate, no glutamine (Gibco)	life technologies	11960-085
fetal bovine serum (FBS), Lot: 426273K	life technologies	10270
fluorescent diacetate	Sigma Aldrich Chemie GmbH	F7378
glycerol	Merck	1040921000
HEPES (PUFFERAN®) \geq 99.5 %	Carl Roth	6762.1
hexane	Carl Roth	KK48.1
HFE-7500	3M	
L-Glutamine	life technologies	25030081
N, N', N'-Tetramethylethylenediamine (TEMED)	Sigma Aldrich Chemie GmbH	T9281
N,N'-Methylenebisacrylamide (BIS)	Sigma Aldrich Chemie GmbH	146072
NIH3T3/GFP (10^6 cells)	Hözel diagnostika	AKR-214
penicillin-Streptomycin (Pen-Strep)	life technologies	15140-122
Picosurf-1 (FC40 + 2%)	Dolomite	3200215
Poly-L-Lysine FITC labeled	Sigma Aldrich Chemie GmbH	P3543-25MG
Poly-D-lysine hydrobromide	Sigma Aldrich Chemie GmbH	P7280
Poly-L-Lysine, Cy3 labeled (PLL-Cy3)	Nanocs Inc.	PL1-S3-1
Poly-L-Lysine, Cy5 labeled (PLL-Cy5)	Nanocs Inc.	PL1-S5-1
Propidium Iodide	Sigma Aldrich Chemie GmbH	P4170
Rhodamine-6G chloride (Lot 562009)	invitrogen	R634 1g
Sodium acetate ($C_2H_3NaO_2 \cdot 3H_2O$)	Sigma Aldrich Chemie GmbH	S-9513
sodium(meta)periodate ($NaIO_4$)	Sigma Aldrich Chemie GmbH	31878-25G
Span® 80	Sigma Aldrich Chemie GmbH	85548

2 Materials

Table 3: Solutions

Name	Composition
acrylamide stock solution (AAM)	40% w/w in Tris-buffer
ammonium Krytox® surfactant	prepared at Institute for Polymer Research [48], see also chapter 3.8
APS stock solution	0.05% w/w in Tris-buffer
bis-acrylamide stock solution (BIS)	2% w/w in Tris-buffer
HEPES	50 mM, pH 8.02
NIH3T3/GFP medium	DMEM (high glucose) + 10% FBS + 0.1 mM MEMNEAA + 2 mM L-glutamine + 1% Pen-Strep (+ optional 10 µg/mL Blasticidin to sort for fluorescence)
PBS	without Mg ²⁺ and Ca ²⁺
PBS ⁺	with Mg ²⁺ and Ca ²⁺
periodate solution	10 mM NaIO ₄ in 100 mM sodium acetate buffer (pH 5.5). Store in fridge. Attention! Periodate is toxic!
Tris-buffer	10 mM, pH 7.48

Table 4: Equipment

Name	Brand	Order No.
15 mL tubes	GBO	188261
2 mL Micrewtube®, selfstanding	Simport GmbH	T341-6T
27 µm PMMA beads	microparticles GmbH	PMMA-F-27.0
33 mm syringe filter, hydrophilic PVDF 0.22 µm membrane	Merck Chemicals GmbH	SLGV033RS
42 µm PMMA beads	microparticles GmbH	PMMA-F-42.0
5 µm PS beads	microparticles GmbH	PS-F-5.0
50 µm PMMA beads	microparticles GmbH	PMMA-F-50.0
50 mL tubes	GBO	227261
Abbe-refractometer 2WAJ	Arcarda GmbH	ABBE-2WAJ
epoxy glue	Faserverbundwerkstoffe ®	1551000
cantilever ArrowTL1x20-50, nominal spring constant k = 0.035 - 0.045 N/m	NanoAndMore GmbH	
cellulose fibre filter	Ziczac (cigarette filters slim)	
centrifuge with 50 mL and 2 mL tube holder & moving arms	Eppendorf	Centrifuge 5804 R
CMOS camera (part of RT-DC setup)	Mikrotron	EoSens® CL
cover slides (ø 18 mm)	Carl Roth	HKH7.1
elbow Luer Connector	ibidi GmbH	10802
Eppendorf tubes with safety lock (1.5 mL)	VWR	211-2140DE
FEP tubing (ID 250 µm, OD 1.5 mm)	Postnova Analytics GmbH	Z-JR-T-6812C
Fluigent MFCS™-EX microfluidic controller	Fluigent	

2 Materials

Name	Brand	Order No.
forceps (unsharp tweezer tips)	Fine Science Tools	11220-21
microscope slides	VWR	631-1552
glassbottom petri dishes (FluoroDish, 35 mm)	World Precision Instruments	FD35-100
ibidi μ -slide VI ^{0.4} Uncoated (#1.5 polymer coverslip, hydrophobic, sterilized.)	ibidi	80601
inverted microscope (part of RT-DC setup)	Zeiss	
luer Lock Connector Female	ibidi GmbH	10825
luer Plug Male (stopper)	ibidi GmbH	10822
magnetic stirrer	IKA®-Werke	KM2 basis
Nanowizard I AFM	JPK Instruments	
oven/heating cabinet	Memmert	UM 200
Parafilm		
peristaltic pump (REGLO Digital)	Ismatec	ISM597
petri dish (10 cm diameter, height 2 cm)	Nunc	172931
PetriDish Heater	JPK Instruments	
polystyrene beads	microparticles GmbH	PS-F-51.0
surgical disposable scalpel (Type 10)	VWR (Braun)	233-5310
silica beads	Whitehouse Scientific	MS0040
silica beads (sicastar) Lot: 1791343-01	micromod	43-00-204
silicone tubing (ID 1.6 mm)	ibidi GmbH	10842
Silikon Tube Tube, DC 732 RTV CLEAR (Dow Corning)	Distrelec	110-41-156
stirring bars (15 x 4.5 mm)	VWR	442-4522
T75 flask	GBO	658175
Temperature control (PID control)	Belektronig	K20
VitraPOR Spezialfilterplatte, Por. F, rechteckige Form 3 mm x 3 mm \pm 0.25 mm. Stärke biplan 1.5 mm \pm 0.25 mm, Kanten fein gesägt	ROBU Glasfilter - Geräte GmbH	16999
<u>Light Microscopy Facility systems:</u>		
Microscope (inverted) Axiovert 200M	Zeiss	
Microscope (inverted) DMI6000	Leica	
Leica HC PL APO 10x 0.4	Leica	
Leica HC PL APO 20x 0.7 Imm Corr	Leica	
Zeiss Plan-Apochromat 20x 0.8	Zeiss	
Zeiss C-Apochromat 40x 1.2 W	Zeiss	
Zeiss Plan-Apochromat 10x 0.45	Zeiss	

3 Methods

3.1 Laser scanning microscopy and microscopy data processing

To perform fluorescence imaging (3D images and time lapse) confocal laser scanning microscopes were chosen.

For scaffold characterization an inverted Axiovert200M from Zeiss equipped with 10x and 20x air objectives was used. When working with air objectives and z-stacks, the refractive index correction included in the ZEN software needed to be adopted to achieve correct 3D objects. For PMMA bead scaffolds a refractive index correction factor of 1.49 was used and for aqueous samples 1.33. Additionally, manual brightness correction with spline interpolation and extrapolation was applied to realize the best images possible.

Microscopy data were processed using FIJI [49]. For the characterization of PLL-Cy5 functionalized PAAm hydrogel bead scaffolds, the objective C-Apochromat 40x 1.2 W (Zeiss) was used. 1 μm z-step size was chosen, laser power of the 633 nm laser was 6.5% and the sum of two lines was acquired. The resulting 3D images (first 30 slices) were filtered with a 3D median filter (2 px, 2 px, 2 px), the brightness and contrast was adjusted (min: 0 and max: 109) and the threshold algorithm "minimum" with the setting 36 – 255 was applied to generate a binary image. The plugin "Voxel counter" was then applied to the binary image. To compare PAAm scaffolds with regular PMMA lattices, filtering of PMMA images was not necessary. Brightness and contrast was adjusted (min: 0 and max: 157) and the threshold algorithm "minimum" was applied (0 – 131 for first data set, 0 – 159 for second data set)

For overnight time lapse imaging an inverted DMI6000 from Leica equipped with a high resonant scanner to enhance imaging speed was used. For resonant scanner imaging, a line average of 8 was taken to decrease the blurring. In addition to time lapse imaging of z-stacks, multiple areas were imaged over the whole time (using "Mark and Find" function). Maximum projections as well as 3D views were generated with FIJI.

3.2 Atomic force microscopy (AFM)

AFM indentation measurements are performed using a Nanowizard I AFM (JPK Instruments) mounted on an inverted microscope (Axiovert 200, Zeiss). Cantilevers used for elasticity measurements were modified by gluing polystyrene beads (radius (R_i) of 2.5 μm or 5 μm) to the end of the tip-less cantilever (ArrowTL1x20-50) using a two-component epoxy glue. The cantilevers were calibrated by thermal noise method prior to each experiment. The beads to

measure were immobilized in a petri dish by coating the dish bottom with 1 μ L CellTak and adding the beads onto the bottom. Then 2 – 3 mL of PBS were carefully added into the dish to avoid beads floating away and the beads were incubated for at least 10 min. All measurements were performed in PBS at room temperature, if not indicated differently (dish was heated with PetriDish Heater).

During the experiments the cantilever tip was positioned over the center of the bead and individual force-distance curves were acquired with up to 3 μ m/s approach and retract velocity and with a contact force ranging from 1 – 12 nN.

The apparent Young's modulus E was extracted from approach force-distance curves using JPK data processing software and analysing only the first 1 – 2 μ m indentation depth. The tip geometry (parabolic indenter with respective radius from equ. (2)) was adjusted according to the experiment. The resulting data were additionally corrected by the so-called "double contact mode" [50] taking the deformation of the bottom part of the hydrogel bead also into account. It expands the conventional Hertz model by a factor k (compression from the substrate) and prevents significant underestimations of the bead's Young's modulus E_B [48].

$$\delta(F_c) = \left[\frac{3 F_c (1 - \nu_B)^2}{4 E_B R_{IB}^{1/2}} \right]^{2/3} \times \frac{1}{k} \quad (1)$$

$$\text{with } k = \frac{R_{BS}^{1/3}}{R_{IB}^{1/3} + R_{BS}^{1/3}}$$

F_c represents the acting force on the cantilever resulting in an indentation depth δ . For the used hydrogel beads a Poisson ratio ν_B of 0.5 was assumed indicating an incompressible material. The factor k is influenced by geometrical dimensions of indenter bead radius (R_I), hydrogel bead radius (R_B) and the infinite radius of the substrate (R_S) (eqn. (2) and (3)).

$$\frac{1}{R_{IB}} = \frac{1}{R_I} + \frac{1}{R_B} \quad (2)$$

$$\frac{1}{R_{BS}} = \frac{1}{R_B} + \frac{1}{R_S} \quad (3)$$

3.3 Refractive index matching of PMMA beads

- Mix 100 μL of 17 μm PMMA beads (stock from company) with 100 μL EtOH
- wash 2x in EtOH (200 μL)
- pipet 1.5 μL of bead suspension (200 μL) on glass slide and distribute (be sure to mix the solution properly directly before you take them out)
- let EtOH evaporate
- add mixed dH_2O -TDE-solution to the beads
- cover with cover slides
- observe under microscope with phase contrast

The refractive index of the beads was reached when the beads switched from dark to bright in their appearance.

The refractive index of the solution was determined by means of a manual refractometer.

3.4 Regular PMMA bead scaffolds for developing analysis algorithm

For regular PMMA bead scaffolds in ibidi μ -slide VI^{0.4} chambers, 50 μm PMMA beads were used.

Preparation:

- Prepare bead-EtOH-suspension by washing 1.5 mL bead stock 3x with 1.5 mL EtOH
- Remove paper from cellulose filter, cut lengthways into half and immerse in small tube filled with EtOH. Take one filter half out, place it on petri dish lid and cut into 3 mm long pieces with the help of tweezers and scalpel.
- Prepare staining solution Rhodamine-6G-TDE:
8.15 mL TDE + 1.85 mL 5 mM Rhodamine-6G in dH_2O . Mix properly and filter it with a 0.45 μm filter

Creating regular bead scaffolds:

- Fill all 6 channels of the ibidi μ -slide^{IV} with pure EtOH and place a filter piece into each channel outlet
- Degas for 5 min
- Add 100 – 120 μL into each inlet to fill the channel completely with beads
- Plug inlet and outlet with EtOH-filled stopper and cover back of the channels with Parafilm
- Place the μ -slide in the slide holder and incubate in ultrasound bath (in cold room) for 4.5 h
- Transfer the slide holder in oven (37°C) overnight

- Fill 5 mL syringe with staining solution and connect a 5 cm silicone tubing + elbow connector to it
- Remove the parafilm from the back and remove the stopper by pulling them out fast
- Plug the elbow connector of the filled syringe in the inlet and carefully fill in ~ 300 μ L into each channel. Remove the liquid from the outlet with a pipet
- Let the staining equilibrate in the dark overnight to enable imaging heights of up to 400 μ m

3.5 Cell culture standards

Cell thawing and seeding

Medium for cells to seed was prewarmed in water bath to 37°C. Cells in cryo tube (10^6 cells) from liquid nitrogen were slowly thawed in the hand. 5 mL warm medium was added into 15 mL tube and the liquid cell suspension was transferred into the tube. The cells were added dropwise and the cryo tube was flushed with 1 mL medium. The cells were spun down at 800 rpm for 5 min. Meanwhile a T75 tissue culture flask was filled with 14 mL warm medium. The supernatant from the tube was removed, the cell pellet was resuspended in 1 mL warm medium and transferred into the T75 flask. Incubation took place at 37°C and 5% CO₂.

Splitting cells

The medium was preheated in the water bath. The old medium was removed from 90% confluent T75 flask and the cell layer was flushed carefully with 10 mL PBS to remove any dead cells. 5 mL Accutase was added into the flask and incubated for 5 min (in the incubator). The flask was flushed with 10 mL medium to detach any remaining cells from the flask bottom. The cell suspension was transferred into 50 mL tube and the flask was washed with 10 mL medium to catch any cells left in the flask. The cells were spun down at 800 rpm and 5 min. The supernatant was discarded and the cell pellet was resuspended in 1 mL warm medium. The cells were counted and 0.5 – 1 x 10⁶ cells were transferred into a new T75 flask filled with 14 mL warm medium. Incubation took place at 37°C and 5% CO₂.

3.6 Fluorescent labelling of ULGP agarose

Fluorescent labelling of agarose was based on the functionalization protocol from Spencer et al. [51].

Table 5: Material for fluorescent labelling of ULGP agarose

Material	Company
PBS ⁺	
ULGP agarose	Sigma Aldrich Chemie GmbH
6 cm glass petri dish with lid	
100 mL Schott flask	
6-well plates (2 – 4 pieces)	Nunc
Cell strainer (Nylon mesh with 70 µm pore size; Falcon 70µm Cell Strainer)	Corning

Preparation of stock solutions:

Periodate solution – 10 mM NaIO₄ in 100 mM sodium acetate buffer (pH 5.5). Store in fridge.
Attention! Periodate is toxic!

Dye stock – dissolve 1 mg dye (AlexaFluor®488 hydrazide (1 mg)) in 300 µL dH₂O (final conc. 3.33 mg/mL). Store at -20°C

Agarose film preparation for 2 mL of 1% ULGP agarose stock:

- 0.02 g of ULGP agarose into 100 mL Schott flask. Add 2 mL of PBS⁺
- Close flask and heat consecutively in microwave until the powder is dissolved
- Place the glass petri dish on a scale (set to zero) and take the liquid out of the flask by using a pipet (usually around 1.2 g)
- Add 500 µL to the flask and “wash” the bottom to get all the agarose out. Fill the liquid also into the dish. Fill up the petri dish until 2 g are reached.
- Mix carefully with the tip in the dish (avoid air bubbles) and ensure a wetting of the whole dish. Thereby a thin agarose layer is created
- Let the agarose solidify in the fridge (around 1 h)

Creating reactive aldehyde groups on the agarose film:

- Fill 2 mL of cold periodate solution onto the agarose film and incubate overnight in the fridge. Store 500 mL PBS⁺ as well in a fridge.
- Next day: Carefully detach the film from the glass dish by moving a small round spatula under the agarose.
- Place the cell strainer into a well of a 6-well plate and pour all agarose with the periodate solution into the strainer. The agarose film (and its fragments) will stay in the strainer, whereas the liquid will be collected in the well. Fill the rest of the wells

with cold PBS⁺ (10 mL into each well) and transfer the strainer with the agarose into the next well. Try to avoid big air bubbles below the strainer. Wash 10 min in the well (just leave it in the well) while keeping in the fridge.

- Every 10 min, transfer the cell strainer into a new well until you washed with at least 250 mL PBS⁺ (24-30 washing steps). (Keep always cold!)
- Discard the used PBS⁺ in a waste bottle suitable for toxic material and discard according to the rules (periodate waste).

Fluorescent labelling:

- Mix 120 µL of the dye stock with 1.88 mL dH₂O to get a dye solution of 0.2 mg/mL
- Carefully transfer all parts of the agarose film back into the petri dish with the help of the spatula.
- Add the 2 mL dye solution to the agarose film and incubate over night at room temperature and in the dark.
- Repeat washing procedure from day before (wash with at least 250 mL PBS⁺).
- Discard the used PBS⁺ in a waste bottle suitable for toxic material and discard according to the rules (hydrazide waste).

The stained and washed agarose was transferred into a 2 mL Eppendorf tube. To heat up agarose to ~ 90-95°C a Thermomix (usually used for PCR) was used. A tube with safety lock was used to avoid liquid evaporation. When the agarose was liquid, it was mixed properly and aliquoted (150 – 200 µL aliquots). Storage at 4°C until usage.

3.7 Production of polydisperse ULGP agarose beads

Polydisperse ULGP agarose beads were used as filter beads to generate 3D hydrogel bead scaffolds.

Table 6: Material for polydisperse ULGP agarose beads

Material	Company
2% ULGP agarose	
Picosurf-1 (new or 1x used and filtered with 0.1 µm filter)	Dolomite
Sterile PBS ⁺	
1 very small magnetic stirrer and 1 small magnetic stirrer	
2 mL Micrewtube® + lid	
Thermomixer	
Magnetic mixer	
1H,1H,2H,2H-Perfluoro-1-octanol (PFO)	Sigma

1. Production of polydisperse agarose beads

- Preheat 200 μ L agarose aliquot in Thermomixer at 95°C (Figure 4)
- Place the magnetic stirrers into the tube as shown in Figure 5.



Figure 4: Agarose aliquot in Thermomixer



Figure 5: Magnetic stirrer in tube

- Tape the tube with the magnetic stirrers on the magnetic mixer (Figure 6)
- Add 200 μ L of the Picosurf-1 into the tube
- Start mixing with \sim 1000 rpm
- Add 200 μ L of liquid agarose solution into the tube, close the tube with the lid (Figure 7)
- Mix 20 min at maximum rotation (1100 rpm) (will get milky, Figure 8)
- Store in fridge for at least 2 h to get all agarose solidified.

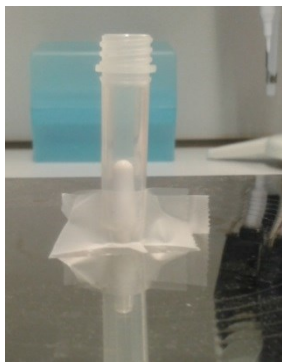


Figure 6: Tube taped on magnetic mixer

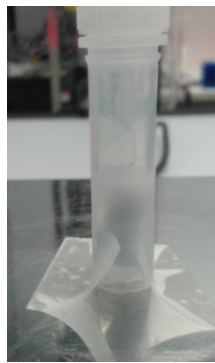


Figure 7: Mixing of oil and agarose



Figure 8: After mixing for 20 min

2. Purification of polydisperse agarose beads

- Move to sterile hood
- Add 400 μ L of sterile PBS⁺ into the tube (beads will now be a white layer between the oil and the PBS⁺)

- Add 100 μL PFO to transfer the beads from the oil phase into the water phase (chemical is taking the surfactant from the beads and allows them to move into the water phase)
- Tilt tube and mix the two solutions carefully, so that the PFO is distributed well everywhere
- Incubate for 30 min or until no white layer is existing anymore
 - i. If this is not happening, add another 50 μL PFO
- Transfer the upper, now clear layer into a sterile 1.5 mL tube. Be careful not to suck up any oil.
 - i. It helps to tilt the tube to get the last rest of the upper layer without taking up oil.

Clean the magnetic stirrers with water, Hellmanex and EtOH.

3.8 Hydrogel bead production via microfluidics

PAAm beads, non-covalent starPEG heparin beads and ULGP agarose beads were produced together with the μ -structure Facility of the CRTD/CMCB and Dr. Salvatore Girardo. Hydrogel beads were produced via microfluidics. The principle sketch of the microfluidic droplet generator chip is shown in Figure 9. Both phases were filtered before they entered the droplet production area as demonstrated in the channel of the discontinuous polymer phase.

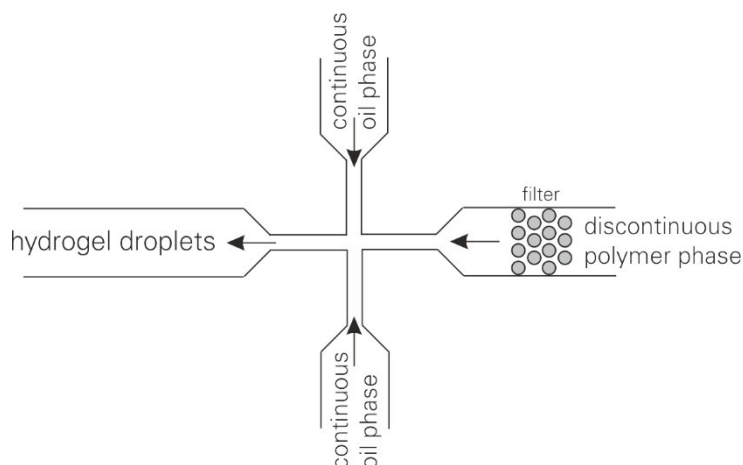


Figure 9: Principle sketch of microfluidic droplet generator chip

The microfluidic devices were produced by the μ -structure Facility and their “inner walls were functionalized by flushing Aquapel® inside the microchannel. The solution was removed by blowing the device with an air gun and leaving it in the oven at 65°C for 10 min.” [48] The

continuous oil phase consisted of fluorinated oil (HFE-7500) with 1.5% w/w ammonium Krytox® surfactant or of Picosurf-1 (FC40 + 2% surfactant). They were filtered before using through a 33 mm syringe filter (0.22 μm membrane). The discontinuous phase consisted of the respective polymer solution. “Two vials containing respectively 1 mL of oil and 100 μL of hydrogel solutions were connected to the inlet chambers of the device via FEP tubing. The flow, through the tubing towards the device, was activated and controlled by pressurizing the

liquids inside the vials by using the Fluigent MFCS™-EX microfluidic controller. It was equipped with two channels able to provide a maximum pressure of 1000 mbar. The resulting gel mixture in oil emulsion was collected in a 1.5 mL Eppendorf® tube through a FEP tubing connected to the outlet chamber of the device.” [48] For agarose, additional temperature control of the polymer reservoir tube was established.

For PAAm beads, 0.4% v/v TEMED was added into the oil solution as well as 0.1% w/v N-hydroxysuccinimide ester for NHS-modified beads. The polymer solution was obtained by mixing acrylamide (AAm), bis-acrylamide (BIS) and ammonium persulphate (APS) in different amounts to reach the respective total monomer concentration c_T (% w/v) with a constant crosslinking to monomer concentration of 3.25%. The molar ratio of BIS to AAm was kept constant at 1:61.5. The final volume of each PAAm solution was adjusted to 545 μ L by adding Tris-buffer to the mixture. The produced droplets were incubated at 65°C for 12 h to complete polymerization. “The final hydrogel beads in oil were washed three times via centrifugation (5000 rcf, 1 min) with each of 20% v/v PFO in HFE-7500, 1 %v/v Span® 80 in Hexane and 1x PBS (without Mg and Ca) solutions. The final bead suspension in PBS was stored at 4°C.” [48]

For non-covalent starPEG beads [52], KA₇-RGDSP-starPEG (2.5 mM) with and without covalent fluorescein was mixed together with heparin (0.1 mM – 0.5 mM). The solutions were prepared by Dr. Robert Wieduwild (BCube). The produced droplets were stored in the fridge over night to complete polymerization. The final hydrogel beads were washed by adding PBS and 20% PFO to the bead-oil mixture. The upper layer was transferred with a pipet into a new tube.

For ULGP agarose beads, ULGP agarose aliquot was preheated in Thermomixer at 95°C (Figure 4) for at least 45 min and shaking at 300 rpm. The agarose vial was heated during production by heat foil at 56°C set point. The actual temperature was 10 K higher. The control settings for temperature control were P: 3.1 V/°C, t_N : 2 s, t_V : 1 s and T1: 1 s. The produced droplets were stored in the fridge over night to complete polymerization. The final hydrogel beads were washed by adding PBS and 20% PFO to the bead-oil mixture. The upper layer was transferred with a pipet into a new tube.

3.9 PAAm bead functionalization

PAAm beads were modified with NHS during their production. HEPES was used to activate the NHS groups and to remove NHS from the solution as this is cytotoxic. Poly-L-Lysine (PLL)

molecules were then interacting with the activated groups and bound via ionic interactions to PAAm. This functionalization was working for all proteins containing amine groups.

- Prepare 1.5 mL Eppendorf tubes with Parafilm (wrap 2x folded Parafilm piece around the upper part in order to fit the tubes in the centrifuge holder (centrifuge with moving arms!))
- Use 100 μL of vortexed bead stock ($\sim 70 \times 10^6$ beads)
- Centrifuge 1 min at ~ 4000 rcf
- Optional: label pellet height on the tube wall
- Remove ~ 50 μL supernatant (change tips for different samples!)
- Add 500 μL HEPES (50 mM, pH 8.0), vortex and centrifuge again
- Remove the supernatant and wash 5x
- After last centrifugation step remove 450 μL supernatant: ~ 100 μL bead solution with 50 mM HEPES
- Add 40 μL of PLL stock (4 mg/mL \rightarrow 0.3 mg/mL final concentration) or functionalization molecule you want (undiluted) to the solution and vortex.
- Incubate in the fridge at least overnight, better several days
- Wash the functionalized beads as before
- Centrifuge as before, remove supernatant, fill up with 500 μL PBS⁺ and repeat the washing step 5x
- Last step: remove supernatant and resuspend pellet in 50 μL PBS⁺

3.10 Real-time fluorescence and deformability cytometry (RT-fDC)

RT-fDC was used to determine PAAm hydrogel bead deformability and fluorescence intensity in parallel [53]. In short, a microfluidic chip with channel width of 20 μm was used. The buffer (0.5% methylcellulose in PBS) was filtered with 0.22 μm syringe filter and centrifuged afterwards to remove all possible crystals. The sheath flow syringe was filled with buffer and the chip was filled with the solution. 100 μL of buffer were filled in an Eppendorf tube (1.5 mL) and 5 μL of PAAm bead pellet was added. The solution was carefully mixed by slow pipetting up and down. The sample syringe was filled with 500 μL buffer and the attached tubing as well. Then 50 μL of the sample were sucked into the syringe through the tubing without any air bubbles trapped in the tubing (~ 2 $\mu\text{L}/\text{s}$). Specific ShapeIn parameters were min. length & height: 10; min. aspect ratio: 0; max. aspect ratio: 2; min grey value: 1 (for $c_T = 7.9\%$) and 2 (for $c_T = 9.9\%$ and 11.8%).

Experiments were run at different flow rates (0.024 $\mu\text{L/s}$, 0.04 $\mu\text{L/s}$, 0.08 $\mu\text{L/s}$, 0.12 $\mu\text{L/s}$, 0.24 $\mu\text{L/s}$). The 640 nm laser was set to 100% power and detection was taking place at 700 nm. For all experiments 5000 events were recorded.

Data analysis was done in ShapeOut with an area ratio 1.0 – 1.5. Deformability between 0.005 and 0.05 were selected for further analysis.

3.11 3D scaffolds made from hydrogel beads

The following protocol was developed and optimized to generate reliable and stable 3D hydrogel bead scaffolds.

Table 7: Material to create 3D hydrogel bead scaffolds

Material
ibidi μ -slide VI ^{0.4} Uncoated (#1.5 polymer coverslip, hydrophobic, sterilized.)
cellulose filter (slim cigarette filter)
scalpel, tweezer (unsharp tweezer tips)
parafilm (whipped with EtOH to sterilize, cut into small rectangles, ~ 1 cm x 1 cm)
absolute EtOH, 15% EtOH (in dH ₂ O)
Sterile dH ₂ O
petri dish (10 cm diameter, height 2 cm, e.g. Nunc: 172931), can be reused
6-10 stopper (ibidi: Luer Plug Male. Order no. 10822), reuse them!
27 μm PMMA beads
42 μm PMMA beads
slide holder (red 3D printed holder)
sterile PBS and medium
filter beads: polydisperse beads made from 2% ULGP agarose (production see production protocol for polydisperse agarose beads)
hydrogel beads for the hydrogel scaffold according to experimental plan

Necessary Lab Equipment:

- Vacuum box to degas filled chamber and liquid
- Centrifuge with 50 mL tube holder + balance equipment
- Oven at 115 – 117°C

Declaration of inlet and outlet in ibidi chamber

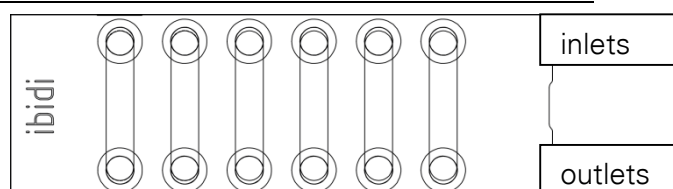


Figure 10: Declaration of inlet and outlet

Usually 2 – 4 channels were needed per experiment. All 6 channels were prepared to have a backup, if something was not working as expected. Unused channels with filter stacks could be kept for further experiments as long as they were not dried out (i.e. closed with Parafilm).

1. Preparation of PMMA Filter Stack (1 day in advance to cell culture experiment!)

- Remove paper from cellulose filter, cut lengthways into half and immerse in small tube filled with EtOH
- Degas 15% EtOH solution for approx. 5 min
- Meanwhile take one filter half out, place it on petri dish lid and cut into 3 mm long pieces with the help of tweezers and scalpel
- Use tweezers to place one filter piece into each outlet (see declaration in Figure 10). Squeeze filter pieces down to bottom. By this, the channel will be filled with pure EtOH. If the channel is not completely filled, add as much EtOH to the outlet as needed to fill the channel but NOT the reservoirs (if the reservoirs are filled, empty them carefully)
- Add 50 μ L of degassed 15% EtOH to outlets and let equilibrate (~ 1 min), so that the inlet is starting to fill with liquid
- Move to vacuum in closed petri dish and degas for 5 min (chamber lid NOT on the reservoirs)
 - If channels are empty, fill the channel again with absolute EtOH and add 50 μ L of degassed 15% EtOH into outlets again
 - Degas again for 5 min (repeat maybe again until all channels are still filled after degassing)
- Close inlets with parafilm pieces
- Fill a stopper with 15% EtOH without any air bubbles, fill the outlet with 15% EtOH and close the outlet with the stopper by merging the two liquids. Take care that no large air bubbles appear in the stopper.
- **Important:** Pull slightly on the stopper to check, if it is tightly closing the outlet. If you can pull it out easily, repeat the closing procedure with another stopper or wrap a small piece of parafilm around the stopper to seal it properly. If outlets are not properly closed, air will come in easily during the next steps.
- Repeat this for all channels

Goal by degassing: No or only few small air bubbles in the channels. Tilt channel with the inlet upwards to try to move them into the inlet.

- Prepare the centrifuge as shown in Figure 11.



Figure 11: Centrifuge preparation. Place the lead in tissue paper into the tube holder, position the chamber on the tube holder with outlets at the bottom and stopper/reservoirs facing outwards. Take care that the holders are properly inserted into the centrifuge.

- Shortly centrifuge the chamber to move all remaining air bubbles upwards into the inlet (press “short” on centrifuge for 3-4 sec)
 - Move to sterile hood if not already done
 - Remove parafilm from inlet
 - Add PMMA beads to channel (place pipet tip directly at the channel inlet in the inlet).
- Important:** Only swirl the flask to disperse the beads in their bottle. Tilt them up and down to check whether all beads are detached from the bottom. Do NOT use the vortexer as this is introducing too much air into the system! Take care that the beads are always well suspended in the flask before you take the corresponding volume out
- First 10 μL of 27 μm PMMA beads directly into the channel inlet
 - Then 30 μL of 42 μm PMMA beads into the reservoir
- Close inlets again with parafilm
 - Centrifuge 1 min at 500 rpm
 - If the degassing was working properly, the beads are NOT sticking to the channel walls! That’s how it should be (see Figure 12)

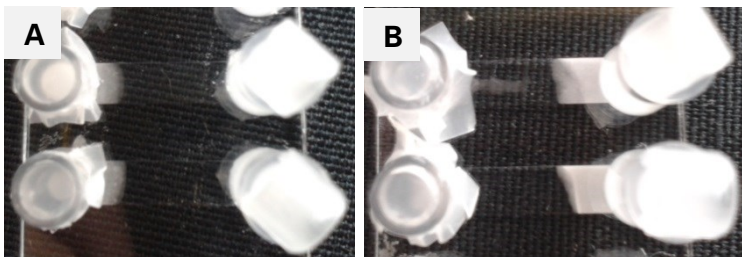


Figure 12: PMMA beads before (A) and after (B) first centrifugation. Beads are not sticking everywhere in the channel.

- Let the beads settle for ~ 5 min
- Centrifuge 2x 1 min at 500 rpm. Maybe let the chamber fall on the table from little height to detach the beads from the inlet wall. Wait 2-3 min before you centrifuge again. Take care that no beads are left in the inlet.

- Place the chamber in the slide holder (vertically! Figure 13A) and bake in an oven at 117°C for 7min (technical drawing of slide holder in Appendix)
- Take the holder out (holder hot!). If the chamber is turned upside down, the beads should not fall apart. The beads should not be distributed in the whole channel or melted together so they appear transparent (Figure 13B). If this is the case, they were boiling (maybe due to a large air bubble in the outlet stopper) and you can't use this channel.



Figure 13: **A**) Position of chamber in holder before baking. **B**) First channel is unusable as the bottom part is melted together completely after baking (indicated by transparent appearance). The second channel is ok, but a few beads are in the channel above the stack. **C**) Perfect channel with no beads in the channel after baking.

- Move back to sterile hood. Remove parafilm from the inlets with the help of the tweezers. Remove remaining liquid from the inlet and fill 130 μ l of sterile PBS into each inlet to wash out the leftover EtOH
- Remove stoppers from the outlet
- Place the chamber lid with the open area upwards into the dish and place the chamber into the dish on the positioned lid. Close the dish lid and store in incubator at 37°C.
- Wash 2 times with PBS by filling up the inlet and emptying the outlet. Use filter paper to enhance washing efficiency. Place a rolled piece of filter paper into the outlet and the liquid will be sucked through due to acting capillary forces.
- Wash 2 times with cell culture medium according to the planned experiment and keep the lid in the petri dish in the incubator until usage, so that the bottom of the chamber has direct contact to the air (at least overnight to saturate the medium with oxygen). If dead cells shall be stained, add 5 μ g/mL propidium iodide (PI) into the medium.

Note: Take care that the liquid level of the outlet is always lower or equal to the inlet one. If not, the equilibration of the liquid levels from outlet to inlet might cause instabilities.

- If the created stacks are now checked under the microscope, one will see a mixture of PMMA beads with pores in between and a small gap between stack and channel

wall on one side of the stack (Figure 14). This gap is caused by swelling of the PMMA beads in EtOH and shrinkage when transferred back to aqueous medium.

- If the bead mixture is not perfect, the first layers might be mainly of small beads. These are not melted properly together, so that they can fall little bit apart. This is fine as the introduced 2nd filter stack will catch and hold those beads.

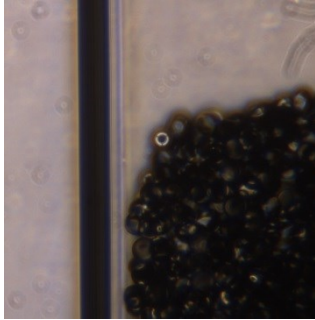


Figure 14: Gap between channel wall and PMMA filter stack

2. Preparation of 2nd Filter Stack

The 2nd filter stack was used to block the occurring gap between stack and channel wall, to catch free PMMA beads and to decrease the pore size of the PMMA stack in order to finally stack up the small hydrogel beads for the scaffold.

- Close all unneeded channels with parafilm (first outlet, then inlet. Leave liquid in the reservoirs.)

For all channels needed for the experiment:

- Close the nearly filled outlets with parafilm
- Add ~ 5 μ L of filter beads (2% ULGP agarose, directly from the dense pellet) into inlet, directly towards the channel (depending on the density of the bead stock, a bit more or less might be useful)
- Close inlet with parafilm
- Centrifuge 1 min at 550 rpm
- Let the beads settle for ~ 5 min (best in incubator)
- Centrifuge 3 min at 550 rpm
- Let the beads settle again for ~ 5 min (best in incubator)
- Centrifuge 3 min at 550 rpm
- Now a proper layer of beads should have established in front of the PMMA filter stack. You can see this by holding the chamber against the light and under the microscope. There will be always a few agarose beads still attached to the channel bottom. You can try to increase the speed to 550 or 600 rpm (NOT higher) and centrifuge again, to

move more into the stack. However, you will always have some agarose beads at the bottom.

Note: If one channel is going to dry out during centrifugation, fill up the inlet with new medium (tilt the chamber slightly and carefully fill medium directly into the channel to avoid air trapped in the channel) and renew the parafilm on outlet and inlet. The drying is caused by leaking liquid.

3. Scaffold Assembly and Static Cell Culture Experiment

Depending on the experimental design different hydrogel beads were used to create scaffolds and layers of differently stiff scaffolds. However, the procedure of scaffold generation was the same for all. Go ahead with the scaffolds after finishing the last filter stack centrifugation.

- Remove parafilm from the inlet and all medium from the inlet to remove any remaining agarose beads. Fill up with ~ 20 μ L warm medium.
- Add ~ 4 μ L of the dense hydrogel bead pellet towards the channel and close inlets again with parafilm.
- Centrifuge 1 min at 550 rpm
- You can check under the microscope, if the new bead layer starts to form while the beads in the inlet are settling down (~ 2-5 min)
- Centrifuge again 3 min at 550 rpm → now a proper layer should have built up. If this is not the case, add more beads and repeat the centrifugation.
- Keep the chamber tilted in the dish in the incubator (place the chamber lid on the bottom of the petri dish, place the closed and filled chamber with the inlet side on the lid (Figure 15))
- Detach cells and count them.
 - Note: For fibroblast experiments, 20 000 cells per channel were fine for an 18 – 20 h experiment (e.g. overnight imaging)
- Depending on the experimental plan, you can seed the cells in two ways.
 - For a stack without any stiffness gradient (Figure 16A), add 2 – 3 μ L of the hydrogel bead pellet into



Figure 15: Tilted chamber position during degassing

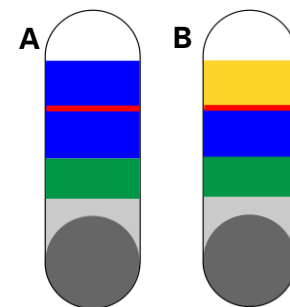


Figure 16: Two different experimental plans

the inlet and add 20 000 cells on top (note seeding time for your experiment if necessary)

- For a stack with two different stiffness (Figure 16B), empty inlet (to remove any left beads), add 30 μL new medium and only the cells and centrifuge immediately after closing inlet.
- Close inlet again with parafilm and wait ~ 1 min
- Centrifuge 3 min at 550 rpm \rightarrow a layer of mixed cells and beads should occur (check at microscope) or a single cell layer. This is also visible by eye as a slightly opaquer layer (cells) when holding against the light.
- Open inlet again and add second bead layer by adding $\sim 3 - 5$ μL of hydrogel bead pellet into the inlet towards the channel
- Close inlet again with parafilm and wait ~ 2 min
- Centrifuge again 3 min at 550 rpm (twice)
- Open inlet again and add 5 – 8 μL of PLL-coated stopper beads into the inlet to hold the scaffolds in place. Close inlet again with parafilm and centrifuge 3 min at 550 rpm (three times)
- Keep the inlet and outlet closed with parafilm. Place the chamber on the lid in the petri dish so that the bottom has contact with the air and incubate until you start imaging. Incubate at least 2 h before start imaging as the stack is still relaxing.
- When using uncoated PAAm beads, an additional PLL-coated PAAm layer has to be added to prevent the stack from fading out too much.

4. Imaging and Analysis

Notes:

- For overnight imaging at 37°C, the microscope should be heated up in advance (at least 2 hours) as the optical components expand a bit.
- Time lapse imaging + z-stack were done at SP5-MP (in the CRTD) \rightarrow used high resonant scanner speed up imaging time (6 stacks ~ 200 μm each take around 10 – 15 min with 488 nm laser only), but needed line average of 8 and one-directional scanning. Otherwise it got too blurry.
- For static culture and over-night imaging, in- and outlets were closed with parafilm to avoid liquid evaporation. Another solution would be to overlay the medium in in- and outlet with oil. But it has to be kept in mind that mineral oil is destroying the bottom of the chamber.

- Medium can be refilled by placing a rolled piece of filter paper into the outlet and filling the inlet.
- **For long-term culture**, where manual medium exchange is not working, it is the easiest way to build up the whole pump system in the incubator to ensure warm medium and the right CO₂ concentration (Figure 17A-D). This system can also be transferred to the microscope (Figure 17E,F). It is possible to time pump stops with the imaging times to avoid too strong movement of the stack due to pumping in new medium.
 - To set up the flow conditions, have a look at Figure 17.
 - Fill the medium into a 100 mL Schott-flask and use it as shown in Figure 17B. By this, air can flow in sterile through the filter and the medium is flowing into the tubing, supported by the height difference of bottle and chamber [54]. Tubing clamps are used to set up the bottle without spilling liquid.
 - Before connecting the tubing to the filled chambers, take care that all tubings are filled without any air bubbles. The medium will flow into the tubings without connecting the pump (due to the height difference).
 - Connect first the tubing to the inlets by elbow connectors, then connect the outlets (outlets filled with medium)
 - Position the pump behind the chamber as the sucking of medium is with less pulsation as the pushing of the peristaltic pump after the pump. The pump can be programmed regarding pumping time, pause time, amount of liquid pumped through.
 - Preincubate tubing and medium 1 day before you start the cultivation in order to saturate everything with oxygen. This is very crucial to avoid any air bubbles in the tubing in front of the culture chamber.
 - After long-term culture, clean the tubing with water, Mikrozid and again water and autoclave everything.
 - Use the orange holder to place the chamber horizontally in a transport plastic box and to have it more stable. It doesn't have to be tilted with the orange holder. It's only shown here for better visibility (Figure 17C and D).

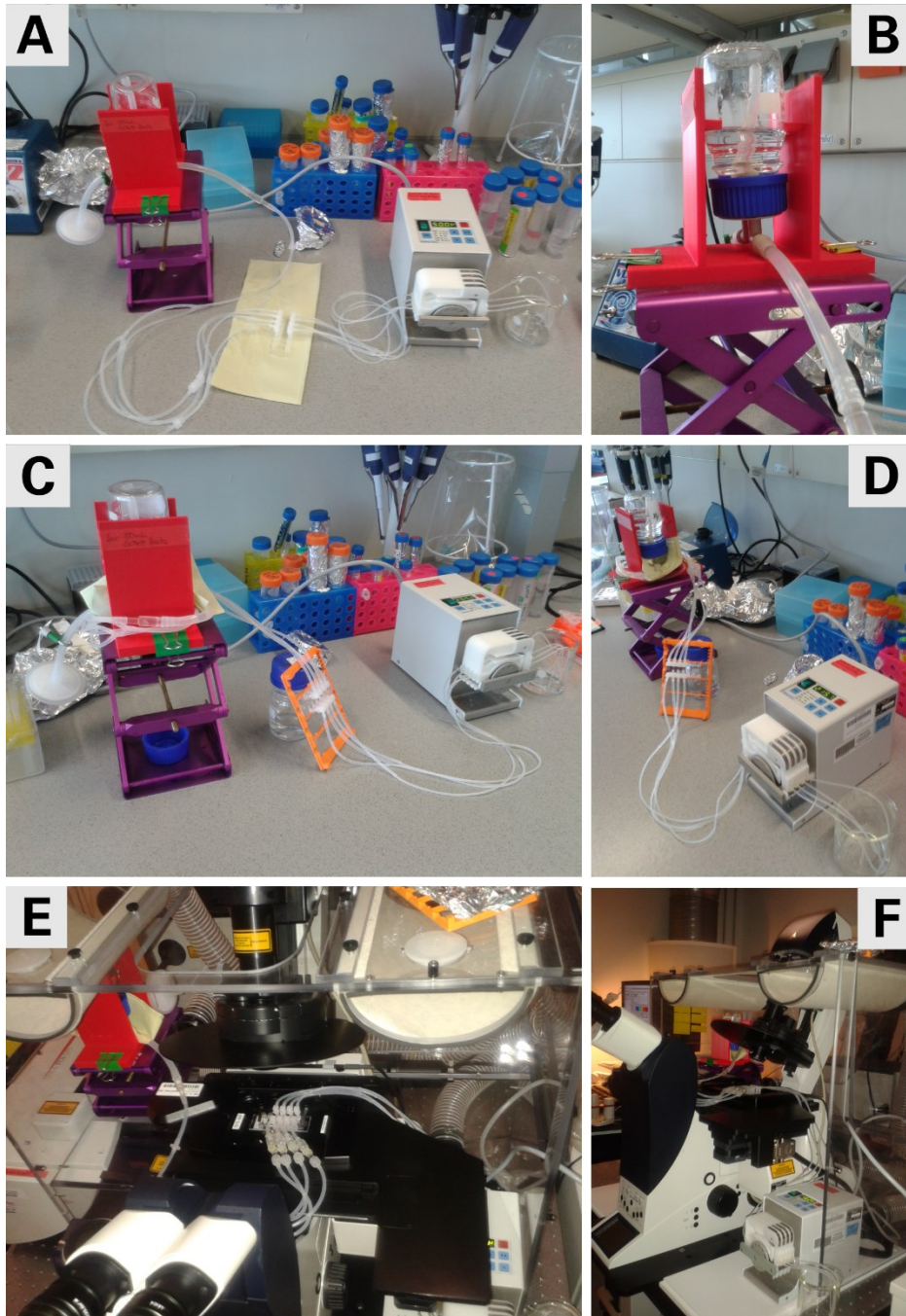


Figure 17: Flow setup for long-term culture and over-night imaging. **A)** Overview of flow setup for long-term culture. From left to right: medium bottle on stage, inlet tubing connected to flow chamber (on beige tissue), outlet tubing connected to peristaltic pump and waste beaker. **B)** Close up of medium bottle positioned in bottle holder on stage to avoid air bubbles in the flow setup. **C, D)** Flow setup that can be used to stack up hydrogel beads. Flow chamber is fixed in slide holder (from Microfluidic ChipShop) to ensure stable position during stacking, but also during cell culturing. **E)** For live-imaging, medium bottle in red flask holder is placed in the microscope incubator to keep temperature and CO₂ concentration constant. Tubings are placed carefully on the microscope stage (inlets facing towards the user) and the chamber itself is clamped onto the microscope stage to ensure stable positions during stage movement. Outlet tubing (facing to the back to the microscope arm) are connected to the peristaltic pump (**F)**, which is also placed in the microscope incubator to limit tubing length.

3.12 Statistics

All box plots were generated with the software OriginPro 9.1. Median was displayed as straight line, the mean as small box and the box (interquartile regime) was defined between 25% and 75% of the data points. Whisker definitions were given at the individual figures as well as the sample number (n). Data points outside the whiskers were defined as outliers. For statistical analysis, non-parametrical Mann-Whitney test was used.

4 Results

4.1 Design of a suitable scaffold device

The proposed 3D cell culture system is based on hydrogel beads as scaffold building blocks. The first step towards stable hydrogel bead scaffolds is the availability of a device that can serve as frame for the scaffold. Two concepts to create bead stacks were investigated, that were also among published methods to generate colloidal crystals [40]. Figure 18A shows the concept of cell culture inserts where the filter mesh at the bottom serves as barrier to block the hydrogel beads. Figure 18B displays the concept of flow chambers where a filter mesh is introduced into the outlet area to block the hydrogel beads in the channel.

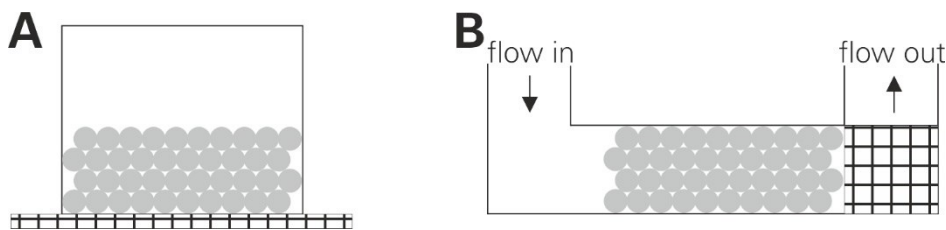


Figure 18: Concepts to create 3D bead scaffolds. **A)** shows concept of cell culture inserts where the filter at the bottom serves as barrier to block beads. **B)** shows a flow chamber with introduced filter in the outlet that serves as barrier to block beads.

These two concepts have been investigated regarding several design considerations listed in Table 8. One important aspect was the existence of a filter to block the hydrogel beads and thereby to create a bead stack. The scaffold had to be at least 150 μm high to ensure 3D culture conditions for cell growth. Additionally, the optical access for at least 50 μm into the bead stack without destroying the device was crucial for live imaging to study cell migration and mechanosensitivity in detail.

Table 8: Design considerations for 3D hydrogel bead scaffold device

Design considerations
Introduction of filter to stop and stack up beads
High enough for 3D culture (at least 150 μm)
Optical access to bead stack w/o destroying device for at least 50 μm
Static culture and long-term cultures
Oxygen content in the channel, diffusion of gas
Handling

Taken all design considerations together, concept A (cell culture inserts) was not followed in detail as the optical access deep into the scaffold was hard to achieve. Cell culture inserts e.g. ThinCert™ from Greiner bio-one, Figure 19, with membrane pores of 3 μm resulted in bead layers on the membrane. The difficulty was then however, that one needed to take out the insert from the medium onto a cover slip to image the stack through the membrane.

Moreover, after imaging the first scaffold layer, it was necessary to image through this to reach the next scaffold layer. This could lead to extensive bleaching of the complete scaffold and cells inside. Optical access was also limited by the working distance of the objectives available at the microscopes.

The development of the scaffold device was therefore focused on the flow chamber concept.



Figure 19: ThinCert™ from Greiner bio-one. Image from <https://shop.gbo.com/en/row/products/bioscience/cell-culture-products/thincert-cell-culture-inserts/>

First ideas were based on a biofilm flow chamber [55], where a cover glass is glued onto the chamber to close the channels. Based on the cover glass top, optical access was ensured. The channel dimensions got smaller compared to the initial design and different ways of introducing filters were tested (Figure 20). Prototype devices were manufactured by selective laser sintering at PTZ-Prototypenzentrum GmbH, Dresden, and polyamide was used as material for the prototypes.

As first filter pieces, special glass filter plates (pore size 4 – 5.5 μm) from ROBU Glasfilter – Geräte GmbH were checked. However, no successful filter plate incorporation into the flow chamber was achieved by gluing filters into prepared molds (Figure 20A) with silicone sealant (Dow Corning). The biggest issue was that liquid always leaked out. Another approach was the use of cellulose fiber filters cut into small pieces, but still larger than the actual filter area. These pieces were pushed into the channel before closing with cover slip or connecting with tubing (performed at design shown in Figure 20B). This method turned out to be very easy and independent from the actual device design. Thus, all further device designs worked with this filter approach.

Based on the adapted biofilm flow chamber designs, developed flow channels became

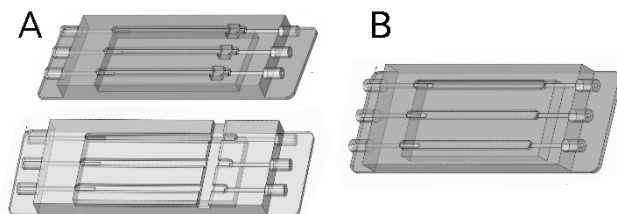


Figure 20: Adapted biofilm flow chambers as potential scaffold devices (design based on [55]). **A)** Flow chambers with different ways of introducing filter pieces by gluing. **B)** Flow chamber for cellulose fibre filter introduction. Technical drawings with exact dimensions can be found in Appendix A.

smaller during the design process to decrease the number of beads needed to fill the channel. 3D printing was tested to produce newly designed devices as their size and detail resolutions reached the limits of the SLS technique available at PTZ-Prototypenzentrum GmbH. EnvisionTEC GmbH used Digital Light

Processing (DLP) and manufactured different prototypes of devices like flow cells (Figure 21B) and static chambers (Figure 21C) as well as masks (Figure 21D) or parts for assemblies (Figure 21E) (technical drawings available in appendix). All devices shared the drawback of leaking after assembly. The use of 3D printed masks to create PDMS-based fluidic chips (Figure 21D) had the weakness of too rough mask surfaces to properly attach a PDMS chip, made from the mask, to glass slides via plasma bonding. Even spin-coating of the glass slide with PDMS did not work out. The use of micro structuring to create 200 – 400 μm high channels was not followed up, as another device came into the view. The commercially available flow chamber “ $\mu\text{-Slide VI}^{0.4}$ ” (Figure 21F) from ibidi GmbH showed ideal properties to work as scaffold device.

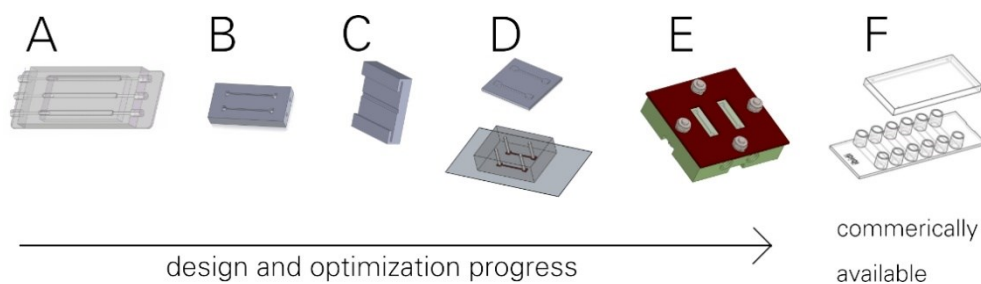


Figure 21: Design and optimization steps during development of scaffold device. Shown devices represent concepts and assemblies, but not in their correct scales (technical drawings can be found in the appendix). **A** is the adapted biofilm flow chamber manufactured by PTZ-Prototypenzentrum Dresden GmbH. **B - E** show different designs produced by envisionTEC GmbH. **F** shows the commercially available flow chamber “ $\mu\text{-Slide VI}^{0.4}$ ”. Technical drawings of **A** and **E** with exact dimensions can be found in Appendix A.

The ibidi $\mu\text{-Slide VI}^{0.4}$ contained six channels with a height of 400 μm . The bottom of the chamber is made of “ibidi Polymer Coverslip”, which is gas diffusible allowing additional oxygen supply by diffusion. This point was always hard to achieve for the custom-made devices, as they were usually closed with a glass coverslip to enable microscopy. However, oxygen cannot properly diffuse through glass. The ibidi Polymer Coverslip enables additionally microscopy techniques as confocal microscopy and provides a standard coverslip thickness of 180 μm . The system allows also the possibility of static and dynamic cultures as inlet and outlet are compatible with luer connectors.

Thus, all considerations for a scaffold device are taken into account with the commercially available flow chamber “ $\mu\text{-Slide VI}^{0.4}$ ”. To characterize the theoretical amount of oxygen available in the flow channel and to investigate oxygen consumption in these 3D cultures, a simulation of oxygen supply was performed.

4.2 Theoretical oxygen supply in 3D culture system is sufficient for cell survival and proliferation

Appropriate oxygen supply in 3D cultures is important as limitations in oxygen affect cell survival and proliferation, and can also result in changes in cell behavior as migration [56,57]. Thus, it was investigated, if the theoretical supply of oxygen by diffusion through the “ibidi Polymer Coverslip” was sufficient for the chosen ibidi chamber. After implementing the diffusion problem with an inward flux of oxygen, $\dot{N}_{o,c}$, an oxygen consumption rate, \dot{R}_i , (Figure 22) and its parameters (Table 9) into COMSOL Multiphysics 5.2, the correct implementation was checked by tuning diffusion coefficient, D , and cell concentration, n_{cell} .

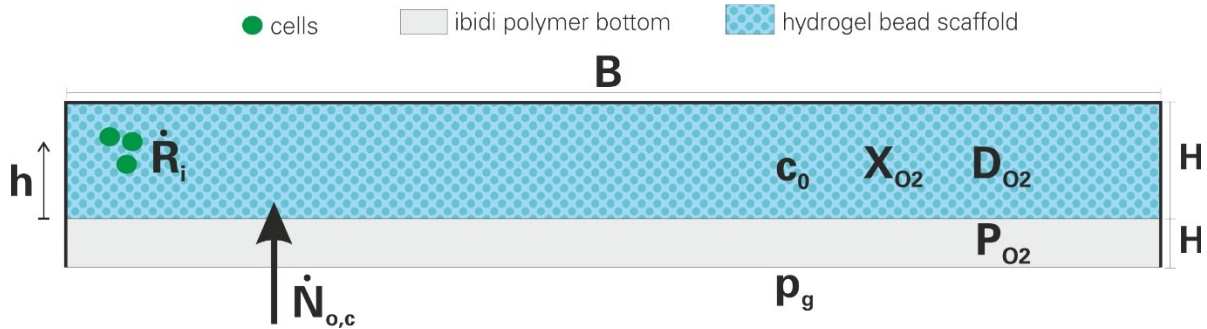


Figure 22: Schematic diagram of cross-section of ibidi μ -Slide VI^{0.4} (channel width B , channel height H_1 , bottom height H_2) with oxygen diffusion parameters (initial oxygen concentration c_0 , ambient partial pressure of oxygen p_g , mole fraction solubility for oxygen in water X_{O_2} , diffusion coefficient D_{O_2} and permeability of plastic bottom P_{O_2}), inward flux $\dot{N}_{o,c}$ and oxygen consumption rate \dot{R}_i .

Oxygen diffuses through different materials with different speed. Therefore it is important to consider the material properties when defining the oxygen influx, $\dot{N}_{o,c}$. Corresponding to ibidi GmbH (personal communication) oxygen diffuses through their polymer bottom (“ibidi Polymer Coverslip”). They determined its area-related permeability for foils and membranes, P , at 23°C, $P_{23^\circ C} = 153 \frac{\text{cm}^3}{(\text{m}^2 \cdot \text{d} \cdot \text{bar})}$. Permeability $P = \frac{100 \text{ cm}^3}{(\text{m}^2 \cdot \text{d} \cdot \text{bar})}$ is defined as 100 cm³ oxygen gas (at norm conditions) diffusing through the sample volume with defined thickness for defined area (1 m²), time (24 h = 1 d) and oxygen partial pressure difference (1 bar) [58,59]. It is stated that permeability increases drastically with temperature [60]. Oxygen permeability at 37°C could only be estimated as it was not determined by ibidi GmbH. By assuming a direct proportional dependence between permeability and temperature, the oxygen permeability at 37°C, $P_{37^\circ C} = 2.8487 \cdot 10^{-3} \frac{\text{cm}^3}{(\text{m}^2 \cdot \text{s} \cdot \text{bar})}$, was extrapolated. This value probably underestimated the actual permeability. In addition, the oxygen volume “cm³” was transformed into “mole” to ensure compatible units for the simulation equations. Considering oxygen as ideal gas, the general gas equation $p \cdot V = n \cdot R \cdot T$ was used to determine the molar mass, n , of 1 cm³

4.2 Theoretical oxygen supply in 3D culture system is sufficient for cell survival and proliferation

oxygen at 37°C as $n_{O_2}(1 \text{ cm}^3, 310,15 \text{ K}) = 1 / 25450 \text{ mol}$. Therefore, the final oxygen permeability used for the oxygen simulations was $P_{37^\circ\text{C}} = 1.1193 \cdot 10^{-7} \frac{\text{mol}}{(\text{m}^2 \cdot \text{s} \cdot \text{bar})}$.

It was assumed that diffusion of oxygen through hydrogels is similar to oxygen diffusion in water [61]. Even though a diffusion coefficient of oxygen in aqueous solutions $D_{O_2} = 3.0 \cdot 10^{-9} \frac{\text{m}^2}{\text{s}}$ is often used [62], it has been shown that medium components such as salts and sugar decrease the diffusion coefficient [63]. Thus, the effective oxygen diffusion coefficient in cell culture medium, $D_1 = 2.69 \cdot 10^{-9} \frac{\text{m}^2}{\text{s}}$, was defined for 37°C from the literature [64].

The mole fraction solubility for oxygen in water, X_{O_2} , was used to determine the amount of oxygen dissolved in the medium after diffusing into the channel, meaning it transformed the ambient partial pressure of oxygen, p , into oxygen concentration, c , within the channel ($p \cdot X_{O_2} = c$). The mole fraction solubility at 1 atm for 37°C, $X_{O_2} = 1.9358 \cdot 10^{-5} \frac{\text{mole } O_2}{\text{mole } H_2O}$, was further adapted to the molar volumes of water and oxygen at 37°C and 1 atm [65], resulting in $X_{O_2} = 1.053 \frac{\text{mole } O_2}{\text{m}^3 \cdot \text{bar}}$. The calculated and used value for mole fraction solubility is comparable with values used in different studies [64,66].

An area, A , of $3.8 \cdot 10 \text{ mm}^2$ was studied, which displayed a small area of the channel where cells were distributed homogeneously. The channel itself was $400 \mu\text{m}$ high (H_1) and the ibidi polymer bottom was $170 \mu\text{m}$ high (H_2).

Oxygen consumption rates (OCR) depend highly on the cell type [67] and can also depend on the medium [61] as well as on the dimension of the microenvironment (2D vs. 3D) [68]. For fibroblasts, an experimentally determined OCR from human dermal fibroblasts in 3D was chosen [68]. Oxygen uptake rates are often modeled with the Michaelis-Menten kinetic, which describes the dependence of the maximum uptake rate (here OCR) on the actual oxygen concentration, c , and the Michaelis-Menten constant for oxygen, $k_{MO} = 1 \mu\text{M}$ [61,62,67–69]. Michaelis-Menten constant, k_m , describes the concentration where the maximum uptake rate is halved. It was assumed, that glucose, which is usually used as substrate for cell growth, was always available.

Table 9: Parameters for oxygen simulation performed in COMSOL

Parameter	Value	Unit	Definition
D_1	$2.69 \cdot 10^{-9}$	$[m^2/s]$	Oxygen diffusion coefficient in medium at 37°C [64]
OCR	$1.19 \cdot 10^{-17}$	$[mol/(s)]$	Oxygen consumption rate (OCR) per fibroblast [68]
n_{cell}	20 000		Cell number
A	$3.8 \cdot 10$	$[mm^2]$	Area
H_1	400	$[\mu m]$	Liquid height/channel height
P	$1.1193 \cdot 10^{-7}$	$[mol/(m^2 \cdot s \cdot bar)]$	Permeability (personal communication with ibidi GmbH)
H_2	170	$[\mu m]$	Height membrane
X_{O_2}	1.053	$[mol/(m^3 \cdot bar)]$	mole fraction solubility
p_g	0.21	$[bar]$	Ambient partial pressure oxygen
K_{mO}	$1.0 \cdot 10^{-3}$	$[mol/m^3]$	Michaelis-Menten Constant for Oxygen, [67]
B	3.8	$[mm]$	Channel width
μ_{max}	$9.627 \cdot 10^{-6}$	$[1/s]$	Maximal growth rate NIH3T3
$D_{1,small}$	$2.69 \cdot 10^{-13}$	$[m^2/s]$	Small diffusion coefficient
D_2	$1.6 \cdot 10^{-9}$	$[m^2/s]$	Reduced oxygen diffusion coefficient for hydrogels [70]
P_1	$5 \cdot 10^{-7}$	$[mol/(m^2 \cdot s \cdot bar)]$	Permeability
P_2	$2 \cdot 10^{-7}$	$[mol/(m^2 \cdot s \cdot bar)]$	Permeability
P_3	$1.5 \cdot 10^{-7}$	$[mol/(m^2 \cdot s \cdot bar)]$	Permeability

For first simulations to check whether oxygen supply was sufficient for short cell culture experiments (around 20 h), cell proliferation was not taken into account. To simulate the oxygen diffusion and its concentration evolution over time, the channel cross-section geometry was defined as rectangle with 3.8 mm width, B, and 400 μm height, H_1 (Figure 22). As material for the channel content “water” was selected. To implement the oxygen concentration change over time, physics of “Transport of diluted species (tds)” was selected, equ. (4), with user defined reaction R_i (consumption of oxygen by cells). By applying the mentioned Michaelis-Menten kinetic on the oxygen uptake, the reaction term for the total volume was defined in equ. (5).

$$\frac{\partial c_i}{\partial t} + \nabla \cdot (-D_i \nabla c_i) = R_i \quad (4)$$

$$\frac{\partial c}{\partial t} + \nabla \cdot (-D \nabla c) = - \left(OCR \cdot \left(\frac{c}{K_{mO} + c} \right) \right) \cdot \frac{n_{cell}}{A \cdot H_1} \quad (5)$$

The initial value for oxygen concentration was $c_0 = p_g \cdot X_{O_2}$ and an isotropic diffusion coefficient, D_1 , was assumed. For the boundary conditions, only one inward flux of oxygen

was defined as equ. (6), corresponding to oxygen diffusion through the ibidi Polymer bottom (Figure 22).

$$N_{O,C} = P \cdot \left(p_g - \frac{c}{x_{O_2}} \right) \quad (6)$$

The simulation mesh was of user controlled size with maximum element size of 20 μm and minimum element size of 0.076 μm . Time unit for time dependent study was seconds and the time range was (0, 100, 72000) s – starting at 0 s, going in 100 s steps towards 72000 s.

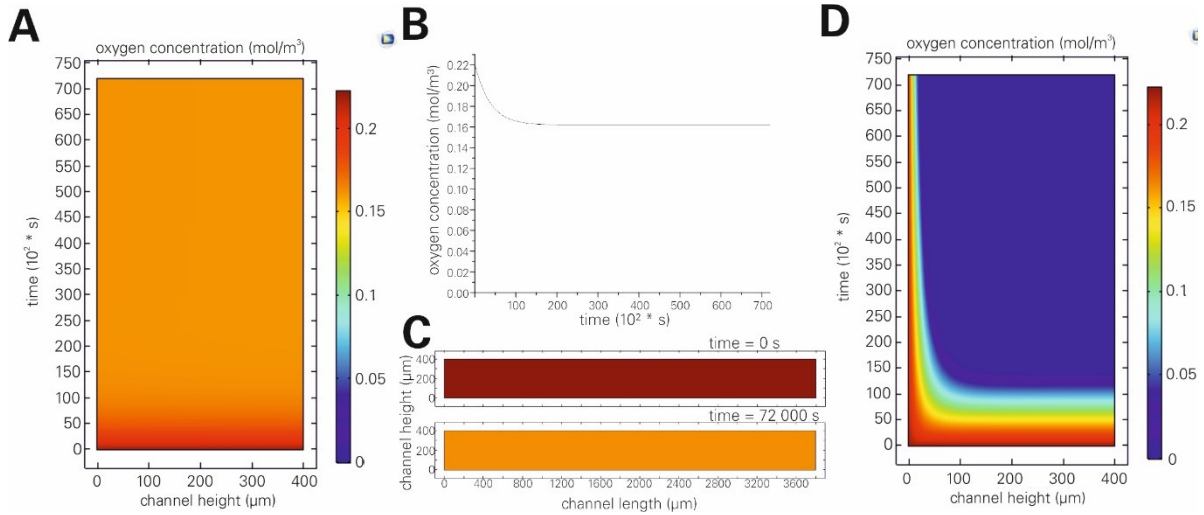


Figure 23: Simulation of oxygen concentration (mol/m³) with cell maintenance. **A)** Evolution of oxygen concentration over time and channel height (μm) with D_1 , 20 000 cells and P . **B)** Evolution of oxygen concentration over time for a random point within the channel with D_1 , 20 000 cells and P . **C)** Starting point ($t = 0$ s) and end point ($t = 72\,000$ s) of oxygen concentration evolution over time for complete channel cross-section. **D)** Evolution of oxygen concentration over time and channel height (μm) with $D_{1,\text{small}}$, 20 000 cells, and P . Colour scales are for all images the same.

The oxygen concentration evolution over 20 h is shown in Figure 23. The oxygen content reached a plateau in the whole channel depth at around 22000 s (6.1 h) and stayed constant over the whole time at around 0.162 M (Figure 23A and B). Comparing the initial oxygen concentration in the channel with the final one (Figure 23C), it is obvious that the oxygen diffusion was fast enough to keep the concentration at a steady-state and no gradient occurred due to limited inward flux of oxygen. When decreasing the oxygen diffusion rate D_1 to $D_{1,\text{small}}$, a gradient in oxygen over time and channel depth established (Figure 23D). This gradient was determined by inhibited oxygen diffusion through the top of the channel and too slow diffusion through the channel volume from the bottom towards the top. This demonstrated a correctly implemented model and cells should survive at least 20 h cultivation assuming a diffusion coefficient D_1 . However, until then only cell maintenance was considered, but no cell proliferation. To implement cell growth, it was published to exchange Michaelis-Menten kinetic with Monod kinetic [71,72], equ. (7) and (8):

$$R_i = -\frac{1}{Y_{X/O_2}} \cdot \mu \cdot C_x(t) , \quad (7)$$

$$\mu = \mu_{max} \cdot \frac{C_s}{K_{mS}+C_s} \cdot \frac{C_{O_2}}{K_{mO}+C_{O_2}} = \mu_{max} \cdot \frac{C_{O_2}}{K_{mO}+C_{O_2}} , \quad (8)$$

where μ_{max} is the maximal cell growth rate, $C_x(t)$ covers cell growth by proliferation and Y_{X/O_2} the yield of cells per unit oxygen. The substrate limitation by $\frac{C_s}{K_{mS}+C_s}$ with $K_{ms} \ll C_s$ was neglected based on the already made assumption that glucose was always available.

$C_x(t)$ was evolved by solving the differential equ. (9) and applying the initial cell concentration $C_{x,0}(t = 0) = \frac{n_{cell}}{A \cdot H_1}$ into equ. (10).

$$\frac{dC_x}{dt} = \mu \cdot C_x \quad (9)$$

$$C_x(t) = \frac{n_{cell}}{A \cdot H_1} \cdot \exp\left(\mu_{max} \cdot \frac{C_{O_2}}{K_{mO}+C_{O_2}} \cdot t\right) \quad (10)$$

$\mu_{max} = 9.627 \cdot 10^{-6} s^{-1}$ was determined using equ. (10) and a published doubling time of 20 h for NIH3T3 fibroblasts (German Collection of Microorganisms and Cell Culture, DSMZ, Braunschweig). Combining these equations, the oxygen consumption rate R_i with cell growth resulted in equ. (11).

$$R_i = -OCR \cdot \frac{C_{O_2}}{K_{mO}+C_{O_2}} \cdot \frac{n_{cell}}{A \cdot H_1} \cdot \exp\left(\mu_{max} \cdot \frac{C_{O_2}}{K_{mO}+C_{O_2}} \cdot t\right) \quad (11)$$

The simulation (Figure 24A) visualized a continuous decrease of oxygen within the channel with increasing time and cell concentration by cell growth. Thus, for long-term culture (i.e. longer than overnight), manual medium exchange to reboot the system with oxygen to the initial state every 24 h or the implementation of a slow continuous or discontinuous flow would be recommended. Hulst1989 showed that diffusion coefficient is decreasing with increasing gel density (e.g. agarose at 30°C) from 2.6 to 1.6 ($\cdot 10^{-9} m^2/s$), D_2 [70]. Colom et al. (2014) also showed a decrease of the diffusion coefficient in gels compared to water [69]. This slight decrease led to no effect in the simulated oxygen concentration (Figure 24B). Thus, the assumption using oxygen diffusion coefficient of medium for diffusion problems [61] hold true also for the here presented system. By tuning initial cell concentration to 40 000 cells and 10 000 cells, the effect of cell growth on available oxygen in the chamber was visualized (Figure 24D, E). It became obvious that cellular oxygen consumption is one limiting factor as seeding 40 000 cells into the chamber resulted in a very low oxygen concentration already after 5.5 h.

4.2 Theoretical oxygen supply in 3D culture system is sufficient for cell survival and proliferation

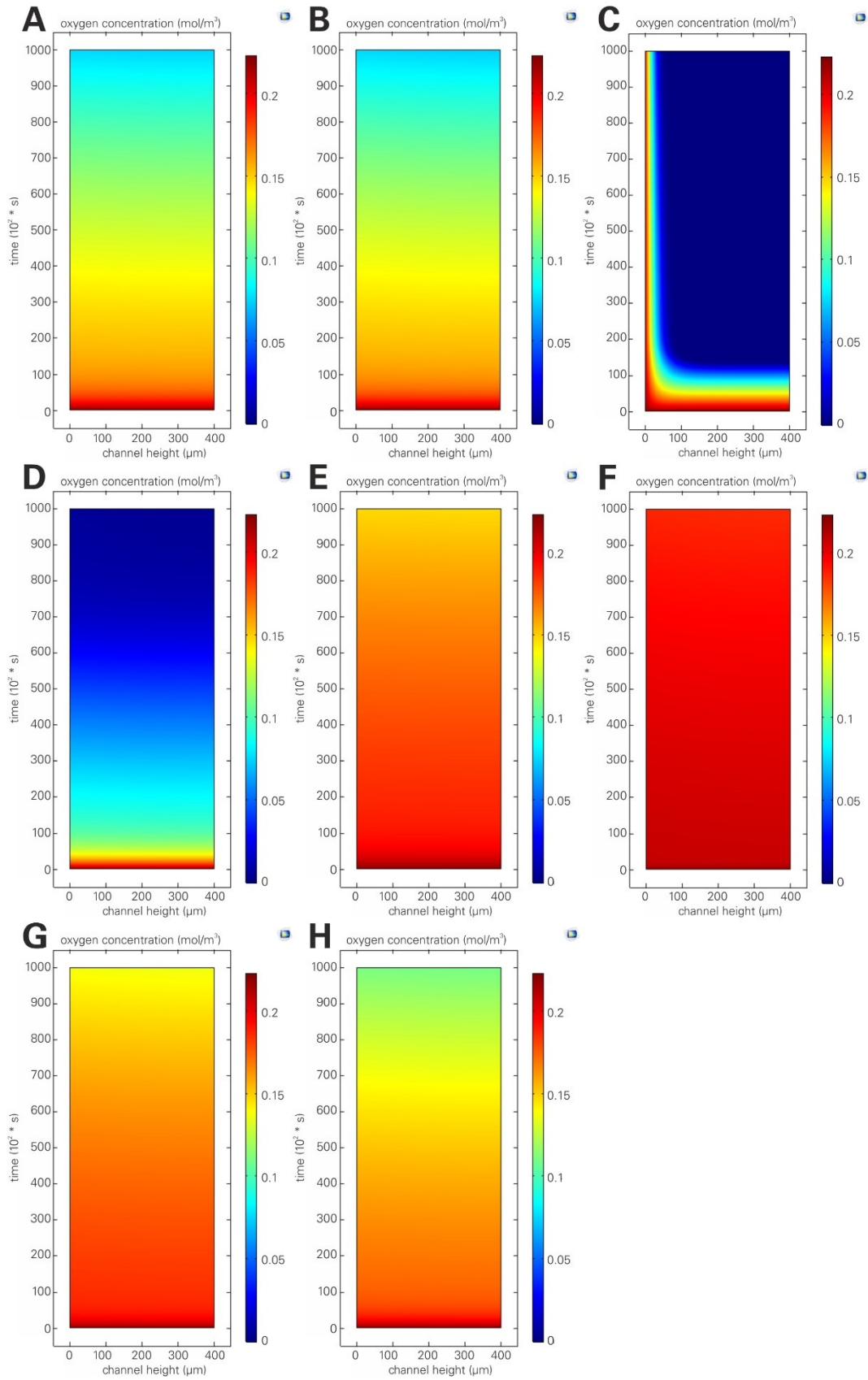


Figure 24: Simulation of oxygen concentration (mol/m³) over time and channel height with cell growth implemented for different diffusion constants (D), cell numbers (n) and permeabilities (P). **A)** D_1, n, P . **B)** D_2, n, P . **C)** $D_{1,small}, n, P$. **D)** $D_1, 2n, P$. **E)** $D_1, n/2, P$. **F)** D_1, n, P_1 . **G)** D_1, n, P_2 . **H)** D_1, n, P_3 . All parameters were defined in Table 9.

The here presented simulation showed cell survival even though the permeability at 37°C was probably underestimated [60]. With higher permeability, more oxygen would diffuse into the channel. How strong the permeability is affecting the available oxygen was investigated by tuning the permeability, P , from $P_1 = 5 \cdot 10^{-7} \frac{\text{mol}}{\text{m}^2 \cdot \text{s} \cdot \text{bar}}$ to $P_3 = 1.5 \cdot 10^{-7} \frac{\text{mol}}{\text{m}^2 \cdot \text{s} \cdot \text{bar}}$ (Figure 24F – H). Already a small increase in P (from P to P_3) led to an increase of oxygen concentration from 0.078 mol/m^3 to 0.115 mol/m^3 after 27 h (Figure 24H). It has been reported that cells respond with anaerobic metabolic processes at hypoxic conditions, defined with 5 – 15 mmHg O_2 (corresponding to $\sim 0.02 \text{ mol/m}^3$) [73]. Considering these facts, cellular function should stay in physiological conditions even for the lower oxygen concentration presented here (for D_1 , n and P).

The developed oxygen diffusion model in the chosen device for parameters defined from literature demonstrated theoretical cell survival and ability to proliferate. Based on these observations, the optimization of the 3D device was extended.

4.3 Further optimization of 3D scaffold device

In order to use the ibidi chamber as 3D scaffold device, beads have to be blocked in the channel to form a scaffold. It had to be determined what kinds of filters are suitable for this. As first filter layer a cellulose fiber filter was used to stop beads in the channel as it was easy to adjust in the chamber by pushing it into the inlet. This filter was however causing problems with small compliant hydrogel beads, because they could squeeze through the fibers and thereby disappeared. Thus, a second filter layer will be necessary. This is generated by small rigid plastic beads that were commercially available and easy to use.

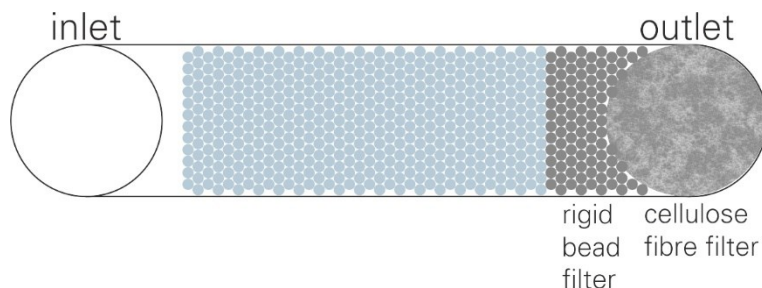


Figure 25: Principle of creating a regular scaffold in the chosen device

4.3.1 PMMA beads can be arranged in stable scaffolds

To block small compliant hydrogel beads in the chamber, stable 3D scaffolds of rigid beads were generated by annealing beads. Additionally, the obtained scaffolds should be used to establish an algorithm to characterize regular 3D scaffolds. Therefore, they also needed to be imageable by fluorescence microscopy by using refractive index matched medium to enable large imaging depth.

Different rigid monodisperse beads available on the market (Table 10) have been analyzed regarding handling like annealing as well as refractive index n_D . To ensure stable filter scaffolds made from rigid beads, the beads have to be able to be annealed. This can be done either by high temperatures (melting the material) or by means of chemicals (gluing the material). However, the treatment also has to leave pores open in the bead scaffolds as liquid still needs to pass through to allow washing steps and medium exchange. To enable scaffold characterization, the bead's refractive index has to be able to be matched with a liquid to minimize light scattering during microscopy. So optical imaging depth can be increased and scaffold heights corresponding to channel height of 400 μm can be visualized.

Table 10: Rigid beads and their corresponding refractive index n

Material	Refractive index n_D (according to company data)
Silica (Whitehouse Scientific)	1.52
Silica (sicastar, biomod)	1.45
Polystyrene (PS)	1.59
Polymethylmethacrylate (PMMA)	1.48

Combining the described needs, Polymethylmethacrylate (PMMA) beads have been selected as the material of choice. Annealing temperatures for silica beads were too high for the ibidi chamber and resulted in destroyed chambers. Also chemicals like Poly-L-Lysine were not able to glue these beads together successfully. An additional problem was that the beads stick to pipet tips and surfaces during handling. Polystyrene (PS) as material for beads was not chosen for filter scaffolds since it did not allow the development of regularity analysis as the material's refractive index was very high with 1.59. PMMA beads could be annealed into scaffolds by means of ethanol incubation, since ethanol leads to swelling of the material and the beads become sticky. This combined with a higher temperature (37°C up to 119°C) creates stable scaffolds. Additionally, the refractive index of PMMA beads was low enough with 1.48 to allow the search for refractive index matching solutions. Thus, PMMA scaffolds were used further.

To match the refractive index of PMMA beads, different solutions were tested for their ability to match a refractive index of around 1.48 and 2,2-Thiodiethanol (TDE) was finally selected. With this, the refractive index of PMMA beads of around 1.488 was determined. Alginate solutions in PBS (10 g/L, 40 g/L, 50 g/L and 100 g/L) resulted in refractive indices between 1.38 and 1.348. Glycerol had a starting refractive index of 1.473, which was still too low for PMMA beads. Also bovine serum albumin (BSA) resulted in a too low refractive index of 1.422 for an 80% (w/v) solution. Producing a 90% (w/v) solution was too viscous and sticky to get

reliable data from. In 2007 a water soluble mounting medium for high resolution microscopy, 2,2-Thiodiethanol, has been published [74]. 2,2-Thiodiethanol has an initial refractive index of 1.521 what allows a refractive index matching by diluting TDE with water. Additionally, its viscosity is low enough to work with compared to high concentrated BSA solutions and it is compatible with fluorescent dyes. Thus, TDE was used to obtain PMMA matched solutions. By mixing TDE and water in variable concentration together, solutions with different refractive indices have been created. The refractive index n_D of each solution was determined with a refractometer. Afterwards washed and dried PMMA beads have been immersed in the respective solution and imaged with a phase contrast microscope. The refractive index of the PMMA beads was defined by the switch of bead appearance from dark to bright (compared to the background). The results are shown in Figure 26. It is clearly visible that the beads become brighter for $n_D = 1.4865$ compared to lower n_D and appear brighter than the background for $n_D = 1.4895$. This results in an approximate refractive index of 1.488 for PMMA beads.

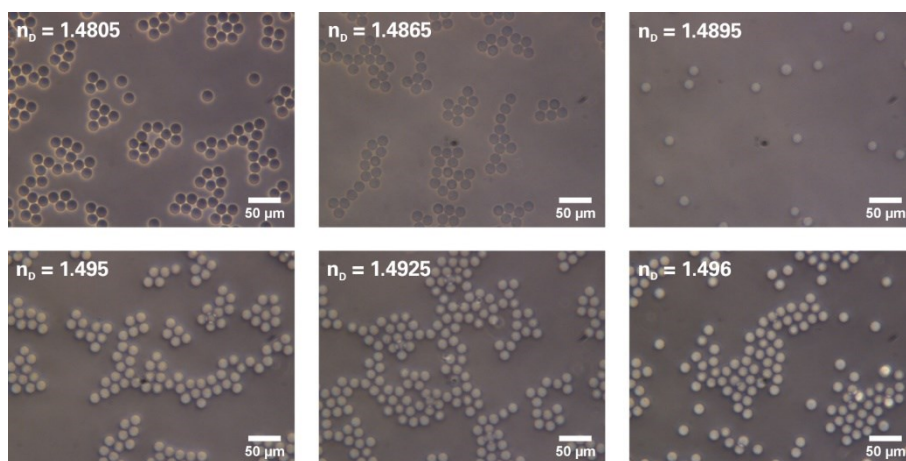


Figure 26: Refractive index matching of 17 μm PMMA beads with 2,2-Thiodiethanol water mixtures with defined refractive index n_D . The refractive index of PMMA beads is defined by the switch of bead appearance from dark to bright in phase contrast. Scale bar 50 μm .

The next step to visualize and characterize rigid PMMA scaffolds was to introduce a staining of either the bead surface or the interstitial space to enable confocal laser scanning microscopy. A homogeneous staining of PMMA bead surfaces with PLL-FITC (before as well as after stacking) was not achieved, but the staining of the interstitial space with Rhodamine-6G-TDE solution was successful. To image the complete stack height, several things had to be kept in mind. The refractive index matched Rhodamine-6G-TDE solution needed to equilibrate in the PMMA bead stack over night after filling it into the stack with the help of a syringe. This ensured a complete filling of the interstitial space with the staining solution by diffusing into the smallest areas of the pores during this time. By applying this method, a

Rhodamine-6G-TDE solution with $n_D = 1.4885$ enabled 400 μm imaging depth and thereby visualization of the complete PMMA bead scaffold. Furthermore, while imaging large scaffold areas with z-stacks and with a low magnification air objective, additional refractive index correction should be applied in the microscope software, if available (ZEN software, ZEISS GmbH). By this, the different scattering of the light in liquid than in air is taken into account when creating the z-stack stacks. A correction of 1.488 was applied for the here presented experiments and by this the beads appeared spherical and not distorted in z-direction.

With the help of Rhodamine-6G-TDE solutions and PMMA beads, stable rigid bead scaffolds were created and imaged. These data were then further processed and analyzed to create regular scaffolds and to develop a way to characterize this regularity.

4.3.2 Regular PMMA bead scaffolds can be achieved and analysed

In order to characterize regular scaffolds and to find out what stacking steps do create a regular rigid bead scaffold, obtained PMMA scaffolds were filled with TDE-Rhodamine solution and imaged after the solution has been equilibrated in the scaffold (over-night). The acquired images were processed and analyzed with a regularity analysis algorithm.

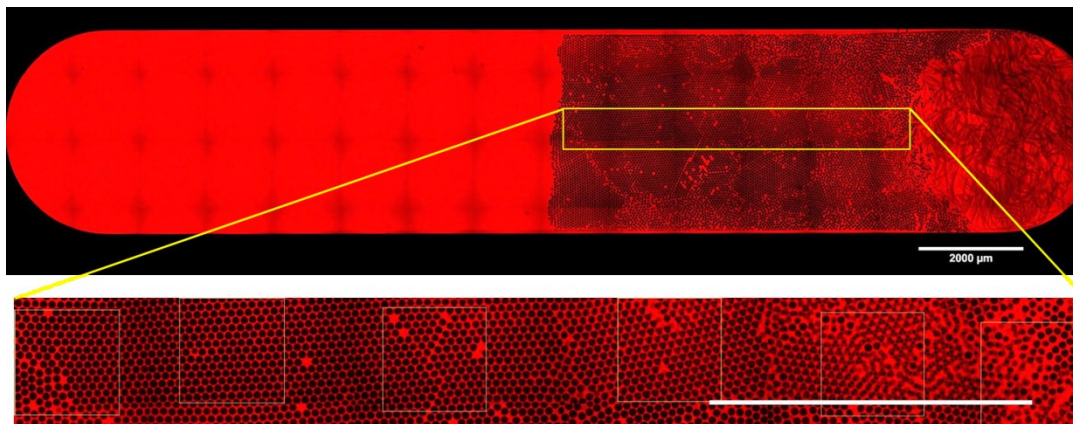


Figure 27: Stable regular PMMA bead scaffolds stained with Rhodamine-6G-TDE solution. 50 μm PMMA beads were used to create these scaffolds. In the close-up six random stacks are shown, demonstrating also small defects and grain boundaries in regular scaffolds. The right end demonstrates irregular structures resulting from the fibre filter. Scale bar 2000 μm .

Six stacks per channel (randomly taken from beginning of the stack to the end) have been acquired. The last stack was not used for regularity analysis as there were lots of artefacts resulting from the fiber filter (Figure 27). These areas were not relevant for any experiments so far and could be neglected for the regularity analysis.

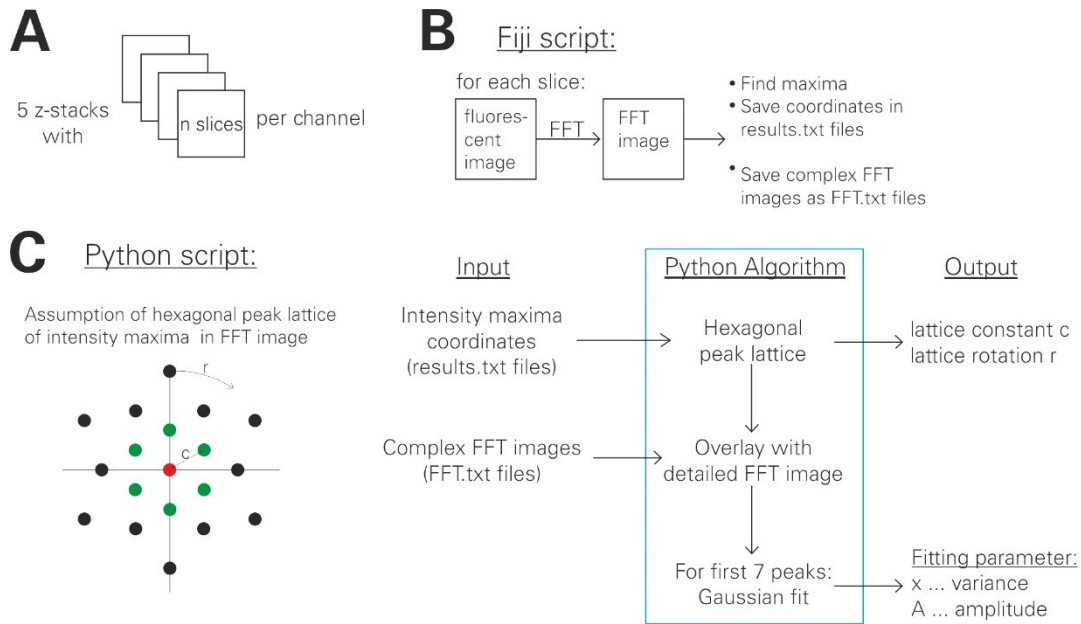


Figure 28: Work flow of regularity characterization **A)** Amount of available data of a bead stack per channel. **B)** Work flow of Fiji script to obtain all necessary data from fluorescent microscopy images of the z-stacks. **C)** Work flow of the Python script (written by Paul Müller) to obtain the fitting parameter (variance x and amplitude A) of the first 7 peaks (red and green peaks) that are used to characterise the regularity of perfectly ordered bead stacks.¹

The regularity analysis employed custom-made algorithms in Fiji and Python (Figure 28, Appendix B). The analysis assumed that monodisperse beads arrange in a hexagonal or cubic close-packed structure to form a perfectly ordered crystal. Upon Fourier transformation, this structure will yield a hexagonal peak lattice of intensity maxima in the Fourier image. Using all acquired images (Figure 28A), a Fiji macro obtained all necessary information from every slice (Figure 28B) by creating for each slice the Fourier image, counting intensity maxima and storing these information additionally to the complex Fourier images. The Python script (written by Paul Müller) used these information (Figure 28C) to create the assumed hexagonal peak lattice and to overlay it with the complex Fourier image. It processed the very first seven peaks (green and red peaks in Figure 28C) as they describe the regularity of the bead stack. By performing a Gaussian fit of these peaks, the resulting output files contained the fitting parameter variance (x) and amplitude (A). They characterize the stack regularity. By using an artificial bead structure image for theoretical analysis, a perfect crystal was defined as “7 peaks have $x < 2$ and $A > 0$ ”. The number of peaks with $x < 2$ and $A > 0$ was determined for all slices per stack and the median per stack was calculated using a custom made MS Office Excel macro (Appendix B). It has to be mentioned that resulting values can only cover 0, 1, 3, 5 and 7 as a result of the internal symmetries of the FFT images.

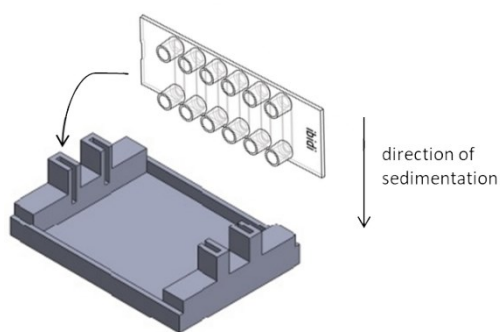


Figure 29: Chamber position in slide holder to generate regular scaffolds

To form regular scaffolds two parameters were investigated in detail. The scaffolds were generated by introducing PMMA beads in EtOH-filled channels and placing the closed chamber in the slide holder as demonstrated in Figure 29. The slide holder was then placed in an ultrasonic bath after a defined sedimentation time. Sedimentation time before ultrasonic treatment was varied as well as ultrasonic treatment time itself. Comparing the median number of peaks

($x < 2$ and $A > 0$) of all stacks for different sedimentation times and ultrasonic treatment times, 4.5 h ultrasonic treatment achieved the result closest to perfect arrangement (7 peaks with $x < 2$ and $A > 0$) (Figure 30). The beads arranged in a regular close-packed structure,

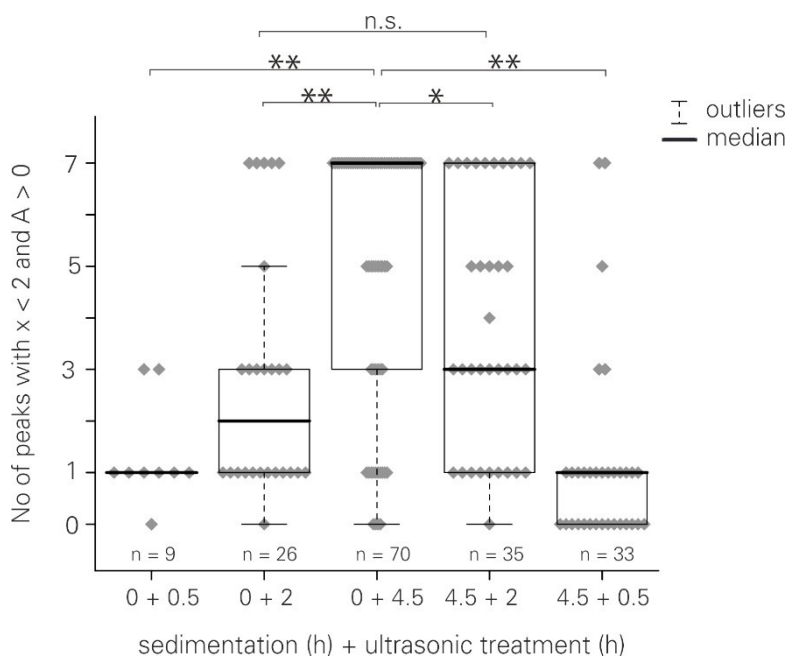


Figure 30: Effect of sedimentation time and ultrasonic treatment time on PMMA bead stack regularity, where a value of 7 represents a perfectly ordered bead stack. Median distribution of n bead stacks from 2-3 independent experiments are analysed by Mann-Whitney Test. The boxes represent 25% to 75% interquartile of the distribution. n represents the number of analysed stacks. * $p < 0.05$, ** $p < 0.01$. Whiskers are defined as 1.5x interquartile regime and outliers as data points outside the whiskers.

based on the ultrasonic treatment immediately after closing the channels and placing the chamber in the slide holder. The ultrasound rearranged the beads until they could not move any more, which was usually the position in the close-packed structure. The variation in medians for 0 h sedimentation and 4.5 h ultrasonic treatment was based on grain boundaries and very small defects within the regular scaffolds (also shown in Figure 27).

The obtained results are in correlation with already observed crystal growth behavior under oscillatory shear conditions [75].

As demonstrated with these stable regular PMMA bead scaffolds and the comparison with the artificial bead crystal, the Python algorithm was able to determine very regular bead scaffolds built from monodisperse beads. For the function as filter scaffold, the stable PMMA bead scaffolds did not need to be highly regular. Therefore, the following filter scaffolds were produced without ultrasonic treatment, but with an optimized protocol to generate stable PMMA bead scaffolds with smaller pores to block small hydrogel beads by centrifuging PMMA beads onto the cellulose fiber filter.

4.3.3 PMMA bead scaffolds and agarose bead scaffolds act as combined filter to stack up hydrogel beads

During production of stable PMMA bead scaffolds and their functional test as filter, the appearance of a gap between scaffold and channel wall was observed (Figure 31). This gap affected stacking efficiency of small hydrogel beads, because they could easily flow through the gap into the cellulose fiber filter and disappeared by this. Thus, the generated PMMA bead scaffolds, that serve as filter to block small hydrogel beads in the channel, could only be used with an additional filter layer as they were not able to cover all necessary functions alone. The stable PMMA bead scaffolds shrank, when the EtOH was replaced with aqueous

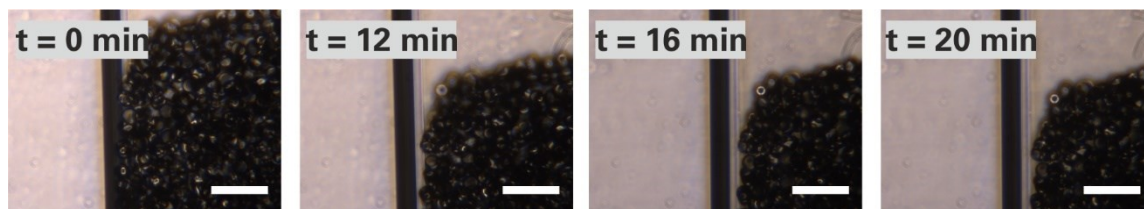


Figure 31: Generation of gap between PMMA bead (50 μm) scaffold and channel wall over time by bead shrinkage, when replacing EtOH with PBS. Scale bar: 200 μm

solutions. The beads swell a little when immersed in EtOH (not stable without swelling regarding company data) and shrink again when transferred back into aqueous solution. As the annealing of the scaffold happens in the swollen state, the whole scaffold shrinks back resulting in a gap between PMMA bead scaffold and channel wall.

As stacking in EtOH was necessary to form a stable scaffold with PMMA beads, this step could not be changed. However, by adjusting EtOH concentration from 100% to 15%, the gap could be minimized while PMMA bead scaffolds were still stable. To overcome the disappearance of small hydrogel beads through this gap, an additional filter layer containing polydisperse beads made of ultra-low gelling point agarose (ULGP agarose) was established. These ULGP agarose beads were produced by emulsification (i.e. vortexing oil-surfactant solution with liquid ULGP agarose). After polymerization and transferring into PBS, these

beads were introduced into the channel. They were centrifuged on top of the washed and stable PMMA bead scaffold to form a third filter in form of a second filter scaffold. As the bigger ULGP beads have more weight, they are faster at the PMMA bead scaffold during centrifugation than the smaller ones. Big ULGP agarose beads then blocked the gap and smaller ones piled up in front of them. However, it was observed that smaller ULGP agarose beads flowed through the pores of the 50 μm PMMA bead scaffold. Therefore, the PMMA bead scaffold composition was adjusted to hinder smaller hydrogel beads to flow through the scaffold pores. This was successfully achieved with a mixture of 27 μm and 42 μm PMMA beads (ratio 1:3). This ratio is important to keep as the PMMA bead scaffold will not be stable otherwise.

In addition, it was observed that a successful and reproducible generation of stable PMMA bead scaffolds highly depended on appropriate degassing of chamber and stacking medium (decrease of air bubbles during annealing) and annealing time in the oven.

Thus, to stack up small compliant hydrogel beads, that would squeeze through the cellulose fiber filter, the knowledge of stacking and stabilizing PMMA beads was used to generate first a stable PMMA bead scaffold in front of the cellulose fiber filter, containing 27 μm and 42 μm PMMA beads (ratio 1:3). The problem of the gap between this bead scaffold and the channel wall was overcome by using polydisperse ULGP agarose beads as second filter scaffold which closed the gap. This combination of different filters allowed the production of hydrogel scaffold made of small hydrogel beads (Figure 32).

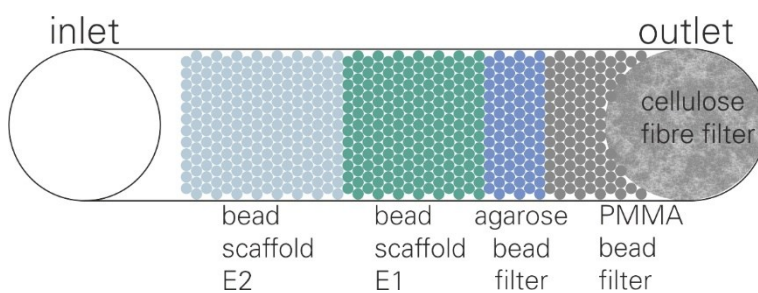


Figure 32: Principle of generating bead scaffold with different stiffness (E) and the applied filter layers (i.e. cellulose fibre filter, PMMA bead filter and agarose bead filter).

4.4 PAAm hydrogel beads produced by microfluidics are suitable to create compliant 3D scaffolds

After successful determination of scaffold device and optimizing it regarding the applied filters, it was necessary to specify suitable hydrogel systems to generate hydrogel beads as scaffold building blocks. Appropriate hydrogel beads had to be stable in production to generate beads with monodisperse size in the range of cells and low variation in stiffness within produced batches. Their overall stiffness needed to be tunable to create scaffolds with different stiffness and ideally the hydrogel system would also offer the possibility of incorporating adhesion molecules to enhance cell attachment.

One of the first questions regarding hydrogel beads was, what bead diameter was actually needed to obtain a regular 3D scaffold (with a hexagonal or cubic close-packed structure) where pores between the beads served as growth area for cells. As the theoretical scaffold structure was assumed to be a close-packed structure, theoretical pore size dimensions in a colloidal crystal could be determined based on the colloidal radius (r_{bead}) using basics of solid state chemistry [76]. In a close-packing of equal spheres, the volume of the pore is defined by the size of the largest sphere that can fit into the void. In close-packed structures, two pore types exist: tetrahedral and octahedral pores (Figure 33). Radius of tetrahedral pores x_t is defined as $0.225 * r_{\text{bead}}$ and radius of octahedral pores $x_o = 0.414 * r_{\text{bead}}$. Considering that cells need a certain amount of space to migrate without disrupting their compartments (i.e. pore cross-section above $7 \mu\text{m}^2$) [77], a pore radius of approx. $2 \mu\text{m}$ (pore cross-section $\sim 12.5 \mu\text{m}^2$) was chosen. This led to a working bead diameter of $10 - 17 \mu\text{m}$.

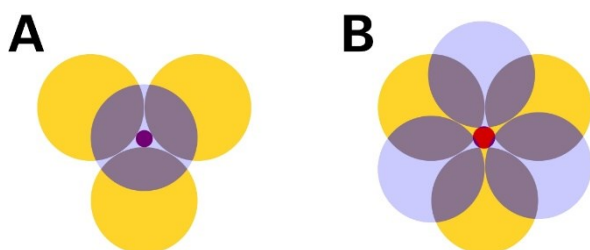


Figure 33: Theoretical pore size dimensions in regular colloidal crystals with the largest sphere (red) that fits into the void. **A)** Tetrahedral pore. **B)** Octahedral pore.

Hydrogel beads of different materials were produced by microfluidic approach (non-covalent poly(ethylene glycol) (PEG) [52], ultra-low gelling point (ULGP) agarose, and polyacrylamide (PAAm)) or by a mesofluidic approach (starPEG [78]). The mesofluidic approach was based on a publication in 2009 [79] and developed and realized at the Institute for Polymer Research (IPF) in Dresden (Figure 34). The microfluidic approach was established at the Microstructure Facility (CMCB, TU Dresden) in co-operation with Dr. Salvatore Girardo as Head of the Facility.

4.4 PAAm hydrogel beads produced by microfluidics are suitable to create compliant 3D scaffolds

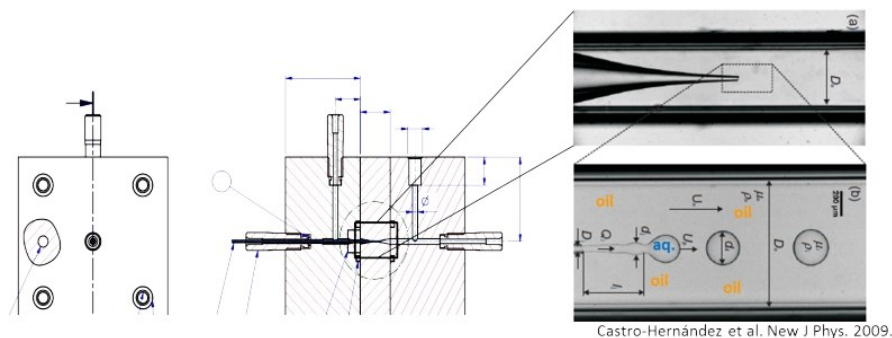


Figure 34: Mesofluidic approach to produce hydrogel beads with a Co-Flow device at the Institute for Polymer Research (IPF), Dresden. Image courtesy: Steffen Vogler

The microfluidic approach used a flow-focusing PDMS-based microfluidic device, where the flows of the oil-surfactant phase (continuous phase) and polymer phase (dispersed phase) was controlled by a pressurized pump. By tuning channel geometry as well as pressure of these two phases different droplet sizes could be generated (Figure 35) [48]. These droplets polymerized afterwards to form hydrogel beads and were transferred by various washing steps from oil phase into aqueous phase. During optimization of droplet production, it turned out that the right choice of oil and surfactant was important to get a stable and fast production.

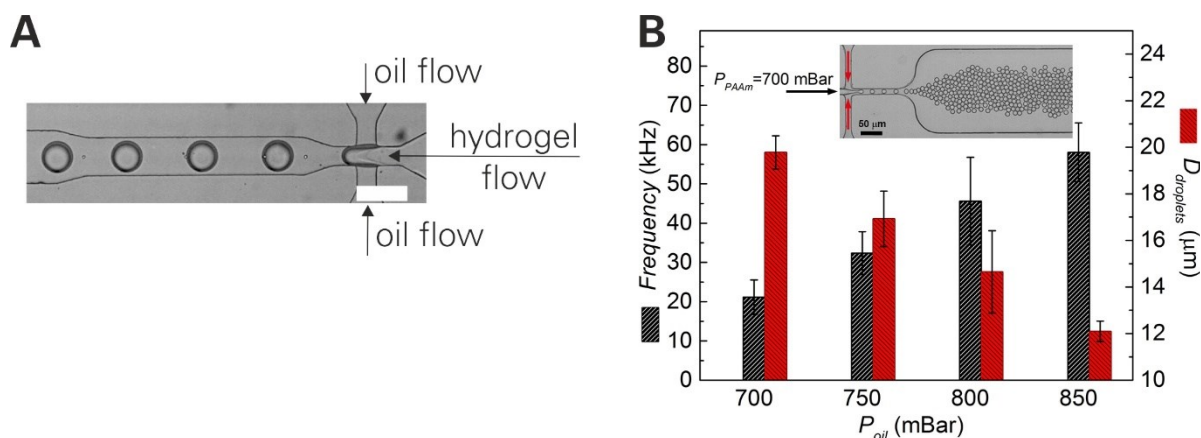


Figure 35: Hydrogel bead production with microfluidic approach (i.e. flow-focusing PDMS-microfluidic device). **A)** Demonstration of flow focussing principle. Scale bar: 100 μm . **B)** Production frequency and droplet diameter depend on the used pressure of the oil phase at constant hydrogel flow pressure (700 mBar) (scale bar in inset: 50 μm). Reprinted from [48].

Four different materials that were already used as hydrogel systems for cell cultures [36,41,52,80,81] were available and investigated as possible candidates for hydrogel beads as scaffold building blocks. For this, hydrogel bead production as well as stiffness determination by atomic force microscopy (AFM), visualization by fluorescence microscopy and the possibility to functionalize with adhesion molecules was studied for all chosen materials. The observations are summarized in Table 11.

Table 11: Investigation of hydrogel bead qualification as scaffold building blocks for covalent starPEG heparin (produced at IPF [78]), non-covalent starPEG heparin (material provided from Dr. Robert Wieduwild, BCube, Dresden [52]), ultra-low gelling point agarose and polyacrylamide.

Material	Observations
Covalent starPEG heparin (IPF) [78]	<ul style="list-style-type: none"> ❖ unstable in production and material properties ❖ extensive swelling ❖ smallest diameter 60 μm possible (status 2016) ❖ polydisperse bead size within one batch ❖ high adhesion (at AFM measurements) ❖ cell attachment
Non-covalent starPEG heparin (Dr. Wieduwild, BCube, Dresden) [52]	<ul style="list-style-type: none"> ❖ unstable in production efficiency and material properties ❖ monodisperse bead size ❖ fluorescent label possible ❖ cell attachment
Ultra-low gelling point (ULGP) agarose	<ul style="list-style-type: none"> ❖ heating (vial) during production necessary ❖ slightly unstable production due to changing viscosity (polymer started gelling despite vial heating) ❖ partly monodisperse bead size (two fractions) ❖ high stiffness difficult ❖ temperature effect ❖ oil effect ❖ no cell attachment w/o additional functionalization ❖ able to be functionalized with fluorescence
Polyacrylamide (PAAm)	<ul style="list-style-type: none"> ❖ stable production and material properties ❖ monodisperse in bead size ❖ no cell attachment w/o additional functionalization ❖ able to functionalize with fluorescently labelled Poly-L-Lysine (PLL)

For all four materials it was possible to adjust the stiffness by changing concentration of the containing components. Stiffness was determined by nano-indentation based measurements with atomic force microscopy. In brief, a small polystyrene bead (diameter: 5 μm or 10 μm) was glued to the tip of tipless cantilevers. The hydrogel beads were then indented with these cantilevers and the apparent Young's Modulus (E) was extracted from recorded force-distance curves by applying the simple Hertz model with additional radius correction by using the double contact model [48,50]. By this, the deformation of a small hydrogel bead at the bottom due to the substrate was also taken into account.

It turned out that the production of non-covalent starPEG-heparin hydrogel beads was not stable enough to ensure reproducible size and stiffness. Also, the material properties changed even though the same batches of initial materials had been used. Thus, the properties of non-

covalent starPEG heparin hydrogel beads were not further investigated at this point. Also covalent starPEG heparin hydrogel beads were not investigated in great detail as their size and stiffness was not reproducible so far and the achieved minimum diameters were 60 μm . For the ultra-low gelling point (ULGP) agarose beads it was observed that the determined stiffness was dependent on temperature (Figure 36A). ULGP agarose beads decreased in stiffness from 230 Pa for 25°C to 120 Pa for 37°C. The agarose hydrogel solidifies at temperatures lower than its gelling temperature and does not depend on any further cross-linker molecule as it is necessary for polyacrylamide or starPEG heparin gels. The decrease of stiffness with increasing temperature was based on the thermosensitive behavior of agarose hydrogels [82,83]. Additionally, the apparent Young's Modulus was affected by the used oil phase during production (Figure 36B). It turned out that hydrogel beads produced in fluorinated oil HFE-7500 with 1.5% Krytox® surfactant [48] led to a 3-fold decrease of stiffness compared to hydrogel beads produced in a commercially available oil supplemented with a surfactant (Picosurf-1, Dolomite). The decrease of stiffness depending on the used oil phase resulted probably from the different molecular weights of the used surfactants (Figure 36C). Molecular transport of agarose molecules from the still liquid agarose over the interface "oil – hydrogel" into the oil phase was favored by smaller surfactant molecules (e.g. 18 000 g/mol vs 7 000 g/mol) as more molecules can fit onto the interface. This is illustrated in Figure 36C by the different distances d between surfactant molecules on the droplet surfaces. Furthermore, the relatively high concentration of small surfactant molecules in the oil phase (total concentration 1.5%) promoted a constant turnover of surfactant molecules on the interface. Thus, more agarose molecules, that were not bound into the hydrogel network yet, were transported from the droplet into the oil phase by exchanged surfactant molecules and thereby decreased the actual agarose concentration in the droplet as illustrated in Figure 36C (correspondence with Dr. Julian Thiele, IPF). If necessary, this problem could be overcome by decreasing the surfactant concentration stepwise down to 0.5% to diminish the transport across the interface.

For ULGP agarose it was not possible to reach stiffness values higher than 2.3 kPa (2% ULGP agarose, produced in Picosurf-1) with the available setup. The 2% ULGP agarose hydrogel started to solidify too fast for higher concentration, which resulted in clogged tubings. Heating the tubing towards the PDMS microfluidic chip could not be achieved with the equipment available, which was also used to heat the vial where the hydrogel was stored. However, with ULGP agarose it was possible to reach very low stiffness values (i.e. 100 Pa and lower). Thus, ULGP agarose beads were further considered to generate hydrogel bead scaffolds.

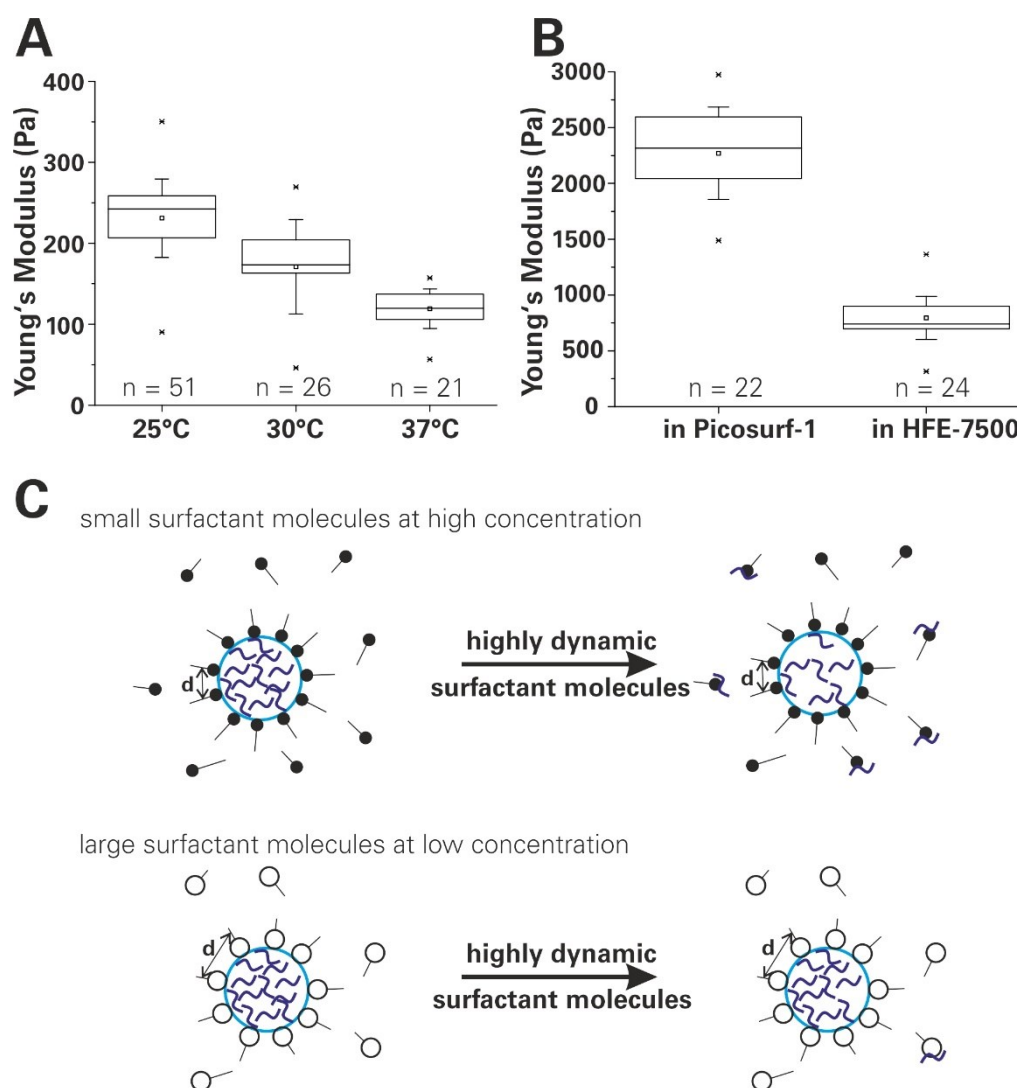


Figure 36: Ultra-low gelling point agarose stiffness and effects influencing it. **A**) Temperature effect on ULGP agarose stiffness (0.5% ULGP agarose in PBS). Young's Modulus was corrected for mean bead diameter. **B**) Oil effect on ULGP agarose stiffness (2% ULGP agarose in PBS). Young's Modulus was corrected individually for each bead diameter. Number of measured beads = n; Box plot whiskers = SD. **C**) Sketch of molecular agarose transport over the interface "oil – droplet" leading to a decrease in agarose concentration followed by a decrease in stiffness. (correspondence with Dr. Julian Thiele, IPF).

By using polyacrylamide (PAAm), it was possible to reproducibly generate stable and small monodisperse hydrogel beads with a wide range of stiffness values [48] (Figure 37) reflecting cell and tissue stiffness [84]. In cooperation with colleagues, these hydrogel beads have been further characterized in depth, e.g. regarding homogeneity, stiffness variation and reproducibility. It also turned out that PAAm hydrogel beads could be easily functionalized with adhesion molecules by incorporating NHS groups during the hydrogel bead production and further addition of adhesion molecules after hydrogel polymerization [48]. This complexity extension of material properties promoted cell adhesion on PAAm hydrogels.

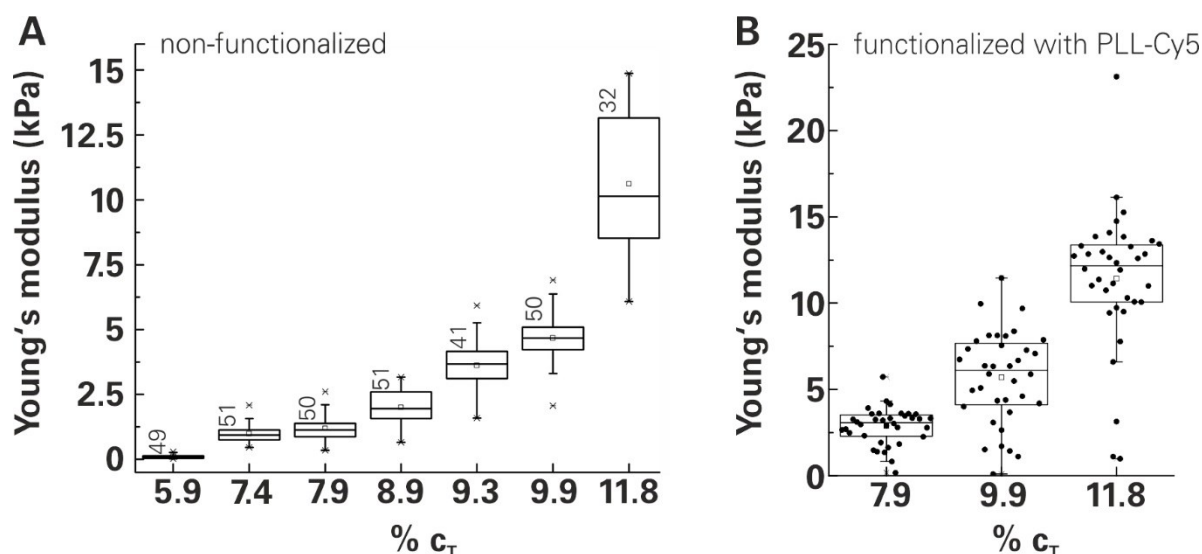


Figure 37: Polyacrylamide (PAAm) hydrogel beads can cover a wide range of stiffness (determined by AFM measurements). **A)** Young's Modulus with varied total monomer concentration (c_T) from 5.9% to 11.8% (n stated in graph, reproduced from [48]). **B)** Young's Modulus of different PAAm hydrogel bead batches (c_T varied) functionalized with PLL-Cy5 (0.3 mg/mL and $\sim 70 \times 10^6$ beads) (n = 34), data points as dots in graph. Whiskers were defined as 1.5x interquartile regime and outliers as data points outside the whiskers.

In order to characterize the amount of bound PLL-Cy5 to the PAAm network for different stiff hydrogel beads, confocal fluorescent images were acquired as well as RT-fDC measurements were performed (Figure 38). Figure 38 demonstrates clearly the dependency of fluorescence intensity to Young's Modulus. The PAAm functionalization, that based on reactive NHS molecules, relied on the polymer network [85]. The more polymer chains are available, the more NHS-groups will be generated in the polymer network during hydrogel bead production. Thus, the amount of covalently bound PLL correlates with stiffness, meaning an increase of bound PLL for stiffer hydrogel beads. A direct correlation between fluorescence intensity and stiffness within one batch has not been observed. However, it seems obvious that the amount of bound PLL varies for differently stiff hydrogel beads.

PAAm hydrogel beads were further considered to obtain hydrogel bead scaffolds as they were easy to produce, stable and reproducible in production and it was possible to functionalize the hydrogel beads and label them fluorescently.

4.4 PAAm hydrogel beads produced by microfluidics are suitable to create compliant 3D scaffolds

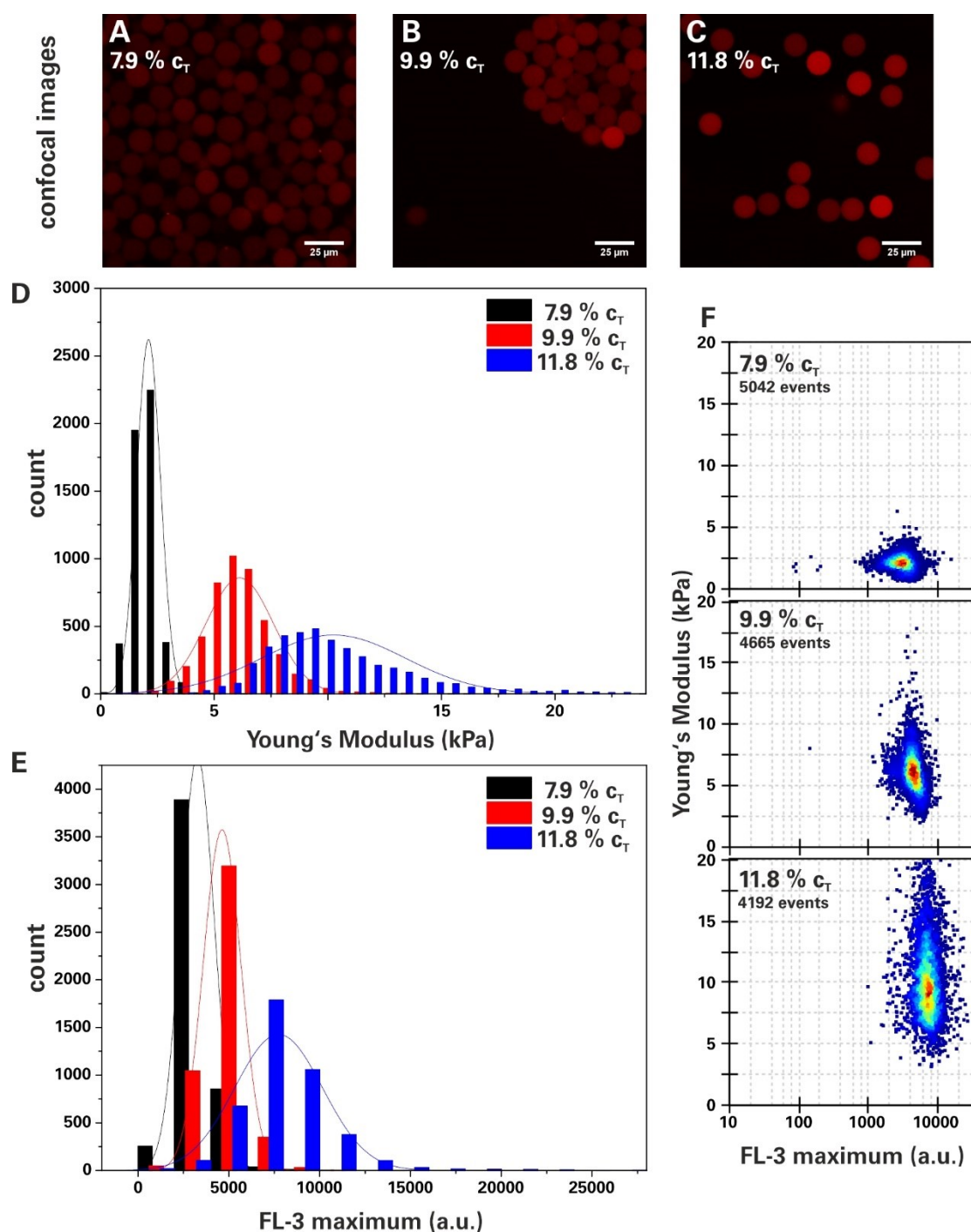


Figure 38 Correlation between PLL-Cy5 fluorescence intensity and PAAm-PLL-Cy5 hydrogel bead stiffness determined by RT-fDC measurement. **A – C** Confocal images of PAAm hydrogel beads (**A**) 7.9% c_T , **B**) 9.9% c_T , **C**) 11.8% c_T) functionalized with PLL-Cy5 (0.3 mg/mL and $\sim 70 \times 10^6$ beads). Image acquisition was done with same settings for all confocal images. Scale bar: 25 μm . **D**) Histogram of Young's Modulus distribution (determined with RT-fDC) with fitted normal distribution for respective PAAm composition. **E**) Histogram of fluorescence intensity distribution (determined with RT-fDC) with fitted normal distribution for respective PAAm composition. RT-fDC scatter plots – FL-Maxima vs Young's Modulus. **F**) RT-fDC scatter plots (Young's Modulus vs. fluorescence intensity) of all three PAAm hydrogel bead samples (flow rates: 7.9% c_T : 0.024 $\mu\text{L/s}$; 9.9% c_T : 0.08 $\mu\text{L/s}$; 11.8% c_T : 0.12 $\mu\text{L/s}$)

4.5 Reproducible, regular and stable 3D scaffolds made of hydrogel beads

After defining potential hydrogel bead candidates (ULGP agarose, PAAm), they were combined with the developed filter combinations to build the actual hydrogel bead scaffolds.

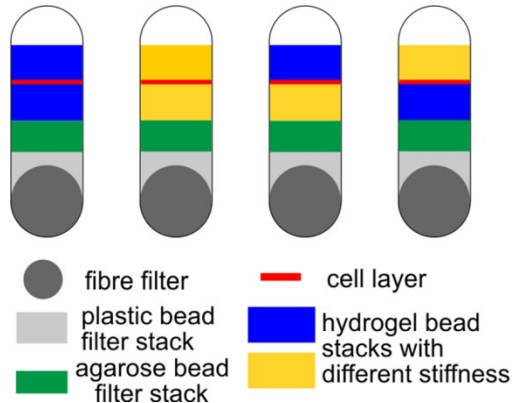


Figure 39: Principle sketch of possible cell culture experiments in hydrogel bead scaffolds (stacks) where cells are introduced as layer between hydrogel bead stacks either with different stiffness or the same stiffness.

It was studied how this hydrogel scaffold could be obtained best and its characteristics (packing/porosity, stability, reproducibility) were determined. Additionally, the possibility to build up layers on top of each other and their stability was investigated. These layers were necessary to build up cell culture experiments as sketched in Figure 39. By generating scaffolds with layers of different stiffness, it was possible to study mechanosensing and durotaxis in 3D as it was done previously in 2D [2].

The hydrogel bead scaffolds were generated by centrifuging the hydrogel beads onto the filter layers. Even though existing covalent and non-covalent starPEG heparin hydrogel beads turned out to be not reproducible in their properties at the studied time point, all four materials were additionally investigated in their ability to form stable 3D hydrogel bead scaffolds. The covalent starPEG heparin hydrogel beads were achieved by a continuous flow setup (Figure 40A). Only polydisperse and large hydrogel beads (minimum size $\sim 60 \mu\text{m}$) were available at that time point, which often contained still oil residuals from the production. They turned out to be very sticky due to the material composition. However, if a hydrogel bead scaffold was once assembled, it was stable. It was easily stained by introduction of $5 \mu\text{g/mL}$ Rhodamine-6G (Rhodamine-6G binds to some molecular parts of the gel) to enable confocal fluorescence microscopy to visualize the 3D structure of the hydrogel bead scaffold (Figure 40B, C). It was observed that especially the large hydrogel beads deformed during stacking and kept this deformation even though the pressure introduced by the pump was released for imaging (Figure 40C).

This could be seen as indication for viscoelastic properties of the covalent starPEG heparin hydrogel, even though the material was previously determined to be almost elastic [86].

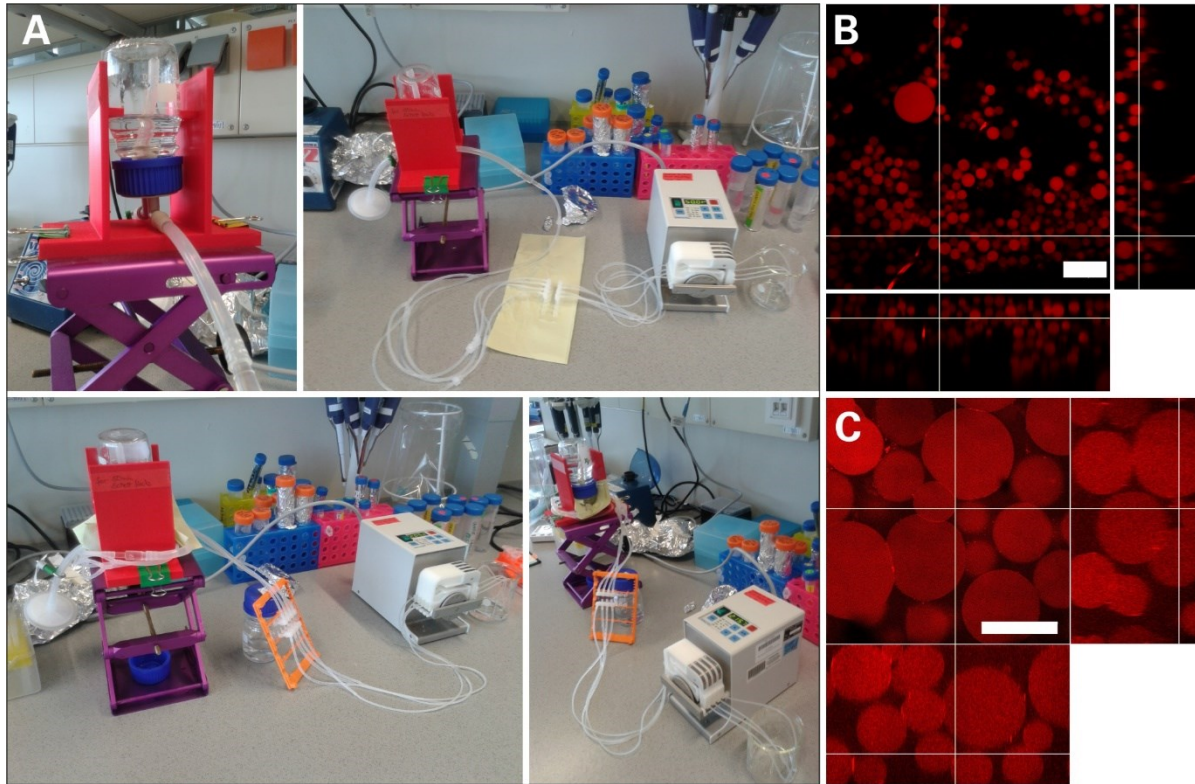


Figure 40: Generation of covalent starPEG heparin hydrogel beads scaffolds. **A)** Continuous flow setup to generate hydrogel bead scaffolds. **B)** Orthogonal view of obtained hydrogel bead scaffold with large hydrogel beads stained with Rhodamine-6G ($\gamma = 1$). **C)** Orthogonal view of obtained hydrogel bead scaffold with intermediate hydrogel beads stained with Rhodamine-6G ($\gamma = 0.5$). Scale bars: 200 μm

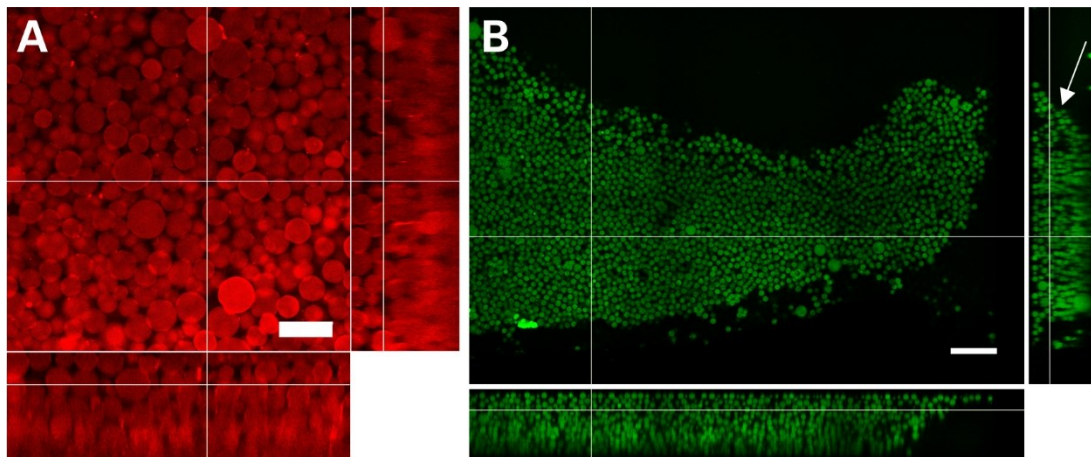


Figure 41: 3D hydrogel bead scaffolds made from non-covalent starPEG heparin hydrogel beads. **A)** Orthogonal view of hydrogel bead scaffold stained with Rhodamine-6G (2.5 mM (KA)₇-RGDSP-starPEG and 0.5 mM heparin). Scale bar: 100 μm . **B)** Orthogonal view of hydrogel bead scaffold (2.5 mM (KA)₇-RGDSP-starPEG+fluorescein and 0.25 mM heparin). White arrow indicates fading out of the scaffold. Scale bar: 300 μm .

The non-covalent starPEG heparin hydrogel beads were assembled both in the continuous flow setup and by centrifugation (Figure 41). The obtained hydrogel bead batches showed a small polydispersity in size with only a few large beads. Also these hydrogel beads were sticky, which resulted in a stable scaffold. However, in Figure 41B a fading out of the hydrogel bead scaffold can be observed (YZ plane, white arrow). This occurred as the hydrogel bead stack was built up while the chamber was positioned vertically, which resulted in a straight border (Figure 42A). This straight border then faded out after the chamber was placed back into its horizontal position (Figure 42B).

As outlook it can be said that for both covalent and non-covalent starPEG heparin hydrogels scaffold generations would be possible, if suitable and reproducible hydrogel beads were available.

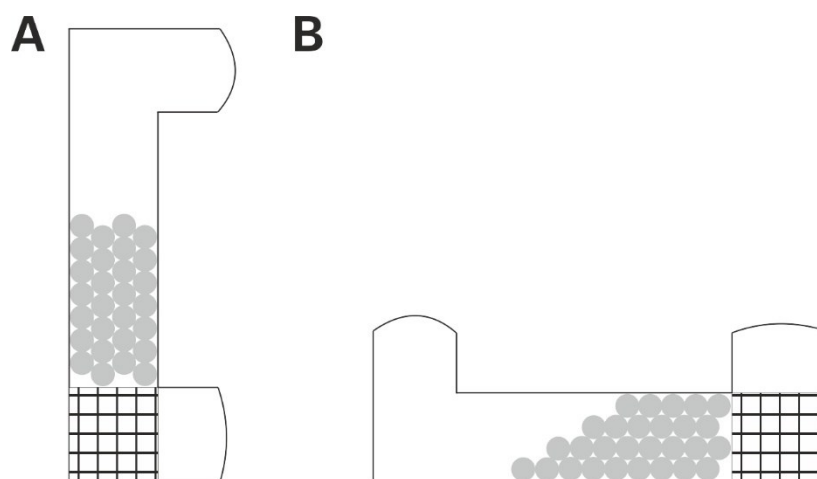


Figure 42: Sketch of fading out of hydrogel bead scaffold after stack generation. **A)** Scaffolds are generated while the chamber is in a vertical position. **B)** Scaffolds fade out after chamber is positioned again horizontally.

Ultralow-gelling point (ULGP) agarose hydrogel beads were assembled in 3D hydrogel bead scaffolds by centrifugation. The 3D structure of the scaffold was only visible for fluorescently labelled ULGP agarose as fluorescent molecules from the liquid surrounding (to stain interstitial space) also diffused into the beads. Thus, a protocol to fluorescently label ULGP agarose was established by adapting a published modification protocol for agarose [51]. The ULGP agarose beads were monodisperse in size and resulted in densely packed hydrogel bead scaffolds (Figure 43). Like this the scaffolds were not very stable resulting in large areas where it faded out over time. To use them, it would be necessary to stabilize the obtained 3D structure in some way. Additionally, a coating with adhesion molecules would enhance the usability of the hydrogel bead scaffold.

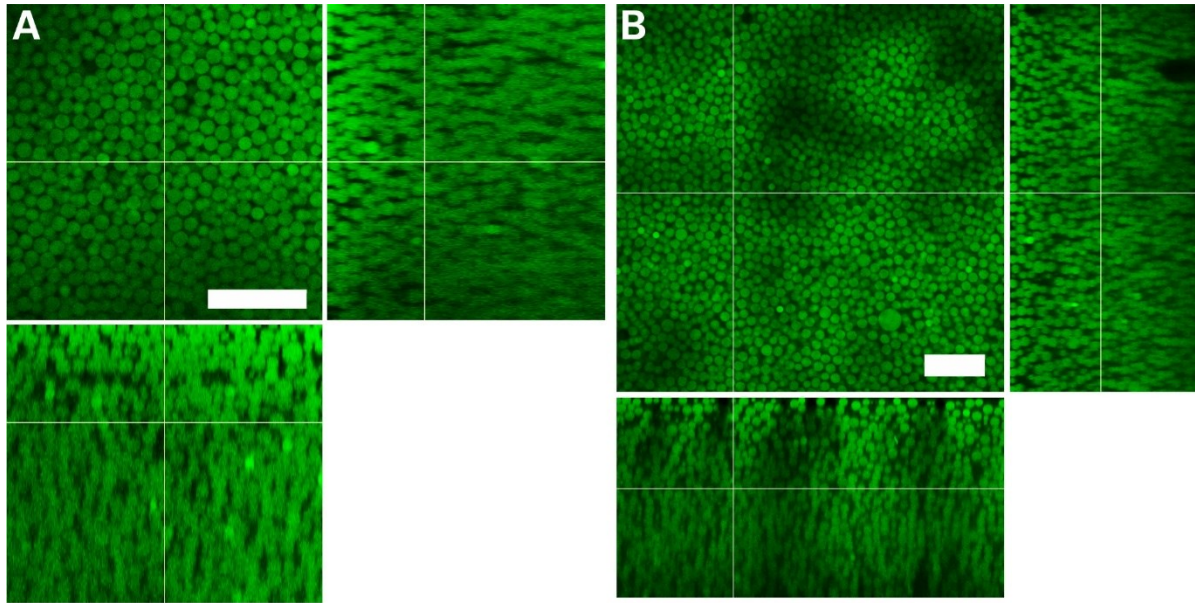


Figure 43: Orthogonal views of 3D hydrogel bead scaffolds made from ultra-low gelling point agarose beads. **A)** 2% ULGP agarose functionalized with Alexa-488 nm. **B)** 1% ULGP agarose functionalized with Cy2. Scale bar: 100 μm .

Polyacrylamide (PAAm) hydrogel beads were also stacked up by centrifugation as 3D hydrogel bead scaffolds. With the monodisperse PAAm hydrogel beads it was possible to generate densely packed 3D scaffolds (Figure 44). For uncoated PAAm hydrogel beads it was already visible with bright field microscopy that they arranged in highly regular structures (Figure 44A). However, 3D imaging of these scaffolds by confocal microscopy was not possible as any dye diffused from the interstitial space of the scaffold into the bulk of the beads due to the large pore size of the polymer mesh compared to tried fluorescence molecules (polymer mesh size: 15 – 60 nm vs. maximum steric diameter of Rhodamine 6G: 1.5 nm [48,87]). The application of large fluorescence molecules, as dextran, to stain the interstitial space would induce the problem of potential osmotic deformation of the beads [88] and could thereby distort the appearance of the scaffold structure. Thus, PAAm hydrogel bead scaffolds presented the same problem regarding visualization as the ULGP agarose bead scaffolds. Their 3D structure could only be visualized by incorporating fluorophores irreversibly into the hydrogel. This was done by functionalizing the PAAm hydrogel with fluorescent Poly-L-Lysine (PLL) [48]. By this, it was possible to image the 3D structure of PAAm hydrogel bead scaffolds.

For the uncoated PAAm hydrogel bead scaffolds, it was observed that they strongly faded out as no sticky PLL was on their surface. If the chamber was tilted the wrong way, the complete scaffold disassembled and rearranged. Also the functionalized PAAm hydrogel bead scaffolds faded out, but not as much as the uncoated PAAm hydrogel bead scaffolds.

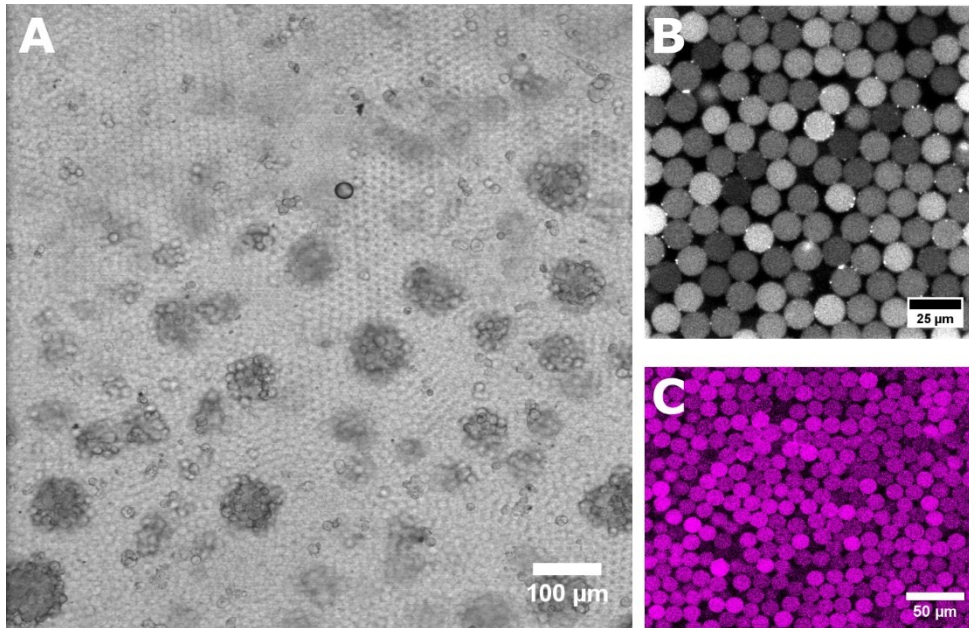


Figure 44: 3D hydrogel bead scaffolds made from PAAm hydrogel beads. **A)** Bright field image of uncoated PAAm hydrogel bead scaffold ($c_T = 13.8\%$; light grey) with NIH3T3/GFP cell clusters incorporated (dark grey clusters) in the scaffold structure. Scale bar: 100 μm . **B)** and **C)** Confocal slices of PLL-Cy5 functionalized PAAm hydrogel bead scaffolds ($c_T = 11.8\%$). Scale bars: 25 μm (B) and 50 μm (C).

An approach to avoid or at least decrease the observed fading out of the 3D hydrogel bead scaffolds was the generation of an additional (sticky) hydrogel bead layer as “stopper layer” on top of the hydrogel bead scaffold to hold the scaffold beads in place. It turned out that this additional layer minimized the movement of the hydrogel bead scaffold. Before imaging (especially for time-lapse imaging) the scaffolds should settle at least two hours after stacking to avoid any large scaffold movement due to rearrangement and fading out during imaging. Another way of holding the scaffolds in place would be the introduction of a fibre filter piece into the channel. However, this approach was not working when tested. An advanced way would be to anneal the hydrogel beads after stacking either by UV light (might be problematic, if cells are already embedded) or chemically, as it has been recently done for hyaluronic acid microporous annealed particle hydrogels [45,46].

One way of characterizing bead scaffolds had been demonstrated with PMMA bead scaffolds (chapter 4.3). However, this characterization was only sufficiently working for highly regular and well stained structures. It was observed that hydrogel bead scaffolds generated from ULGP agarose beads did not arrange in any regular structure as previously observed for PMMA beads (Figure 43 and Figure 45A, B). With functionalized PAAm hydrogel beads regular structures could be achieved, but the staining was irregular (Figure 45C) based on the already observed differences within a batch (compare Figure 38).

To determine the repeatability and porosity, PAAm hydrogel bead scaffolds were imaged with confocal microscopy with a z-step size of 1 μm . The acquired 3D images were further processed (filtering and thresholding to generate binary images) and analyzed with the FIJI plugin "Voxel counter". The plugin calculated beside different areas also the volume fraction, which was used to compare different hydrogel bead scaffolds with each other. Figure 45 compares the volume fractions of regular PMMA bead scaffolds with irregular and regular PAAm hydrogel bead scaffolds. It was possible to generate regular PAAm hydrogel bead scaffolds with a volume fraction comparable to the regular PMMA bead scaffolds. Also the irregular hydrogel bead scaffolds showed volume fractions similar to regular plastic bead scaffolds (Figure 45E). Important for a proper analysis was bright and regular staining of the structure (either hydrogel beads or interstitial space), small step sizes in z-direction as well as a suitable threshold adjustment for the microscopy images to limit data misinterpretation by false-positive pixel determination. Such data misinterpretation can be observed in Figure 45, where a regular PMMA scaffold (Figure 45A) resulted in a volume fraction of 76.9%. Based on necessary volume interpolation during volume fraction determination, the points where the beads were connected with each other appeared either larger or smaller than they actually were (Figure 45A vs B, second part). Volume fractions of randomly close packings vary between 0.60 and 0.74 for spheres of same size [89]. So far, it has been demonstrated that it is not possible to reach a higher volume fraction than $\sim 74\%$ for any packing of monodisperse spheres [90,91]. Thus, a smaller step size in z-direction is recommended for future analysis to diminish the interpolation error during volume fraction calculation resulting in an overestimated volume fraction. Further data misinterpretations were generated by the irregular staining of the PAAm hydrogel beads. Figure 45D compares a filtered confocal slice from the middle of the z-stack with its binary counterpart. The binary image was not able to visualize the boundaries of the hydrogel beads at the connection points adequately. This was based on the initial weak and irregular staining in combination with light scattering during microscopy. Suitable refractive index matching of the medium (e.g. with TDE or iodixanol) to the refractive index of the hydrogel beads should lead to an increase of imaging quality by decreasing loss of detectable photons due to light scattering [92].

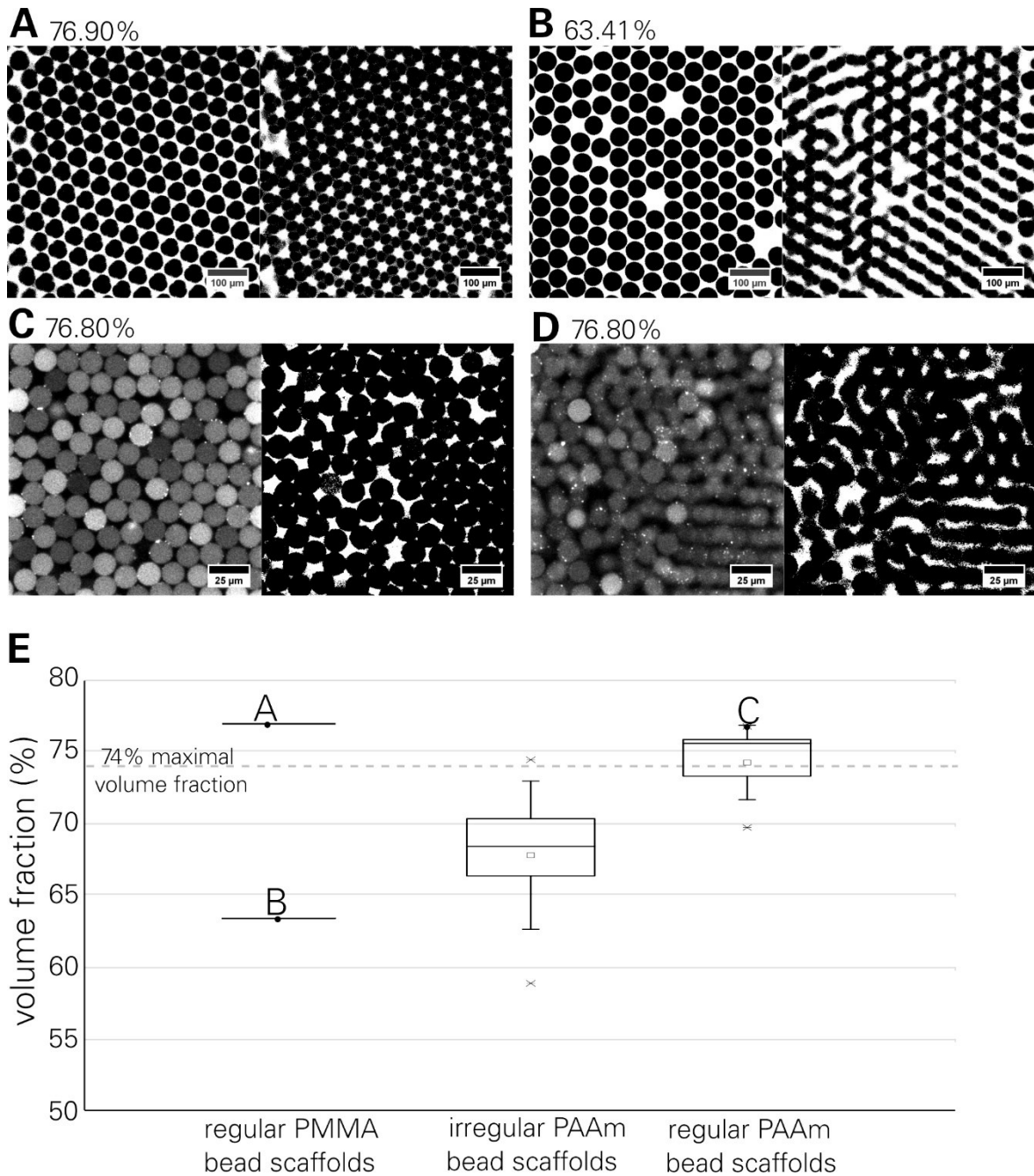


Figure 45: Characterization and comparison of regular, well stained PMMA bead scaffolds and irregular stained PAAm hydrogel bead scaffolds. Volume fractions (%) of binary 3D confocal stacks were determined by FIJI plugin “Voxel counter” **A**) Two exemplary images of a highly regular PMMA scaffold at different z-positions and with volume fraction of 76.9%. Scale bar: 100 μm . **B**) Two exemplary images of a regular PMMA scaffold with defects at different z-positions and a volume fraction of 63.71%. Scale bar: 100 μm . **C**) and **D**) Exemplary confocal images at different z-positions and respective processed binary images of a regular PAAm hydrogel bead scaffold (functionalized with PLL-Cy5) (C and D are from same stack). Scale bar: 25 μm . **E**) Volume fractions of different PMMA bead scaffolds (A, B), irregular PAAm bead scaffolds ($n = 6$) and regular PAAm bead scaffolds ($n = 9$, including C). 74% illustrates the maximal volume fraction that can be achieved based on theory [90,91]. Whiskers were defined as standard deviation and outliers as data points outside the whiskers.

One advantage of the developed scaffold generation method was the ability to create differently stiff layers within one hydrogel bead scaffolds. The scaffold layers were successfully stacked up on top of each other by alternating the centrifugation steps and addition of new hydrogel beads. The scaffold interfaces were stable over night with the help of large stopper layers to hold the scaffolds in place.

Taken together, it was possible to generate reproducible, partly regular and stable hydrogel bead stacks with PAAm hydrogel beads. Due to the material properties of PAAm, a broad stiffness range could be covered and hydrogel beads with and without functionalization were generated. Additionally, the best results in scaffold generation and characterization based on these properties were achieved for PAAm hydrogel beads. Thus, PAAm was the material of choice for first cell culture applications.

4.6 NIH-3T3/GFP cell migration within 3D hydrogel bead scaffolds

After successful scaffold generation and characterization, PAAm hydrogel bead scaffolds were generated with stiffness layers of $\sim 2\text{--}3\text{ kPa}$ ($c_T = 7.9\%$), $5\text{--}6\text{ kPa}$ ($c_T = 9.9\%$) and around $11\text{--}12\text{ kPa}$ ($c_T = 11.8\%$) (Figure 37). Fibroblasts were used to investigate cell survival as well as performing initial cell migration studies within differently stiff hydrogel scaffolds. GFP-labelled fibroblasts (NIH3T3/GFP) were chosen as they are a robust cell type, easy to handle and they already demonstrated distinct reactions to stiffness changes of their microenvironment [2,31].

By random cell seeding into hydrogel bead scaffolds and daily manual medium exchange, cell survival of NIH3T3/GFP fibroblasts was checked. Figure 46 illustrates successful survival of

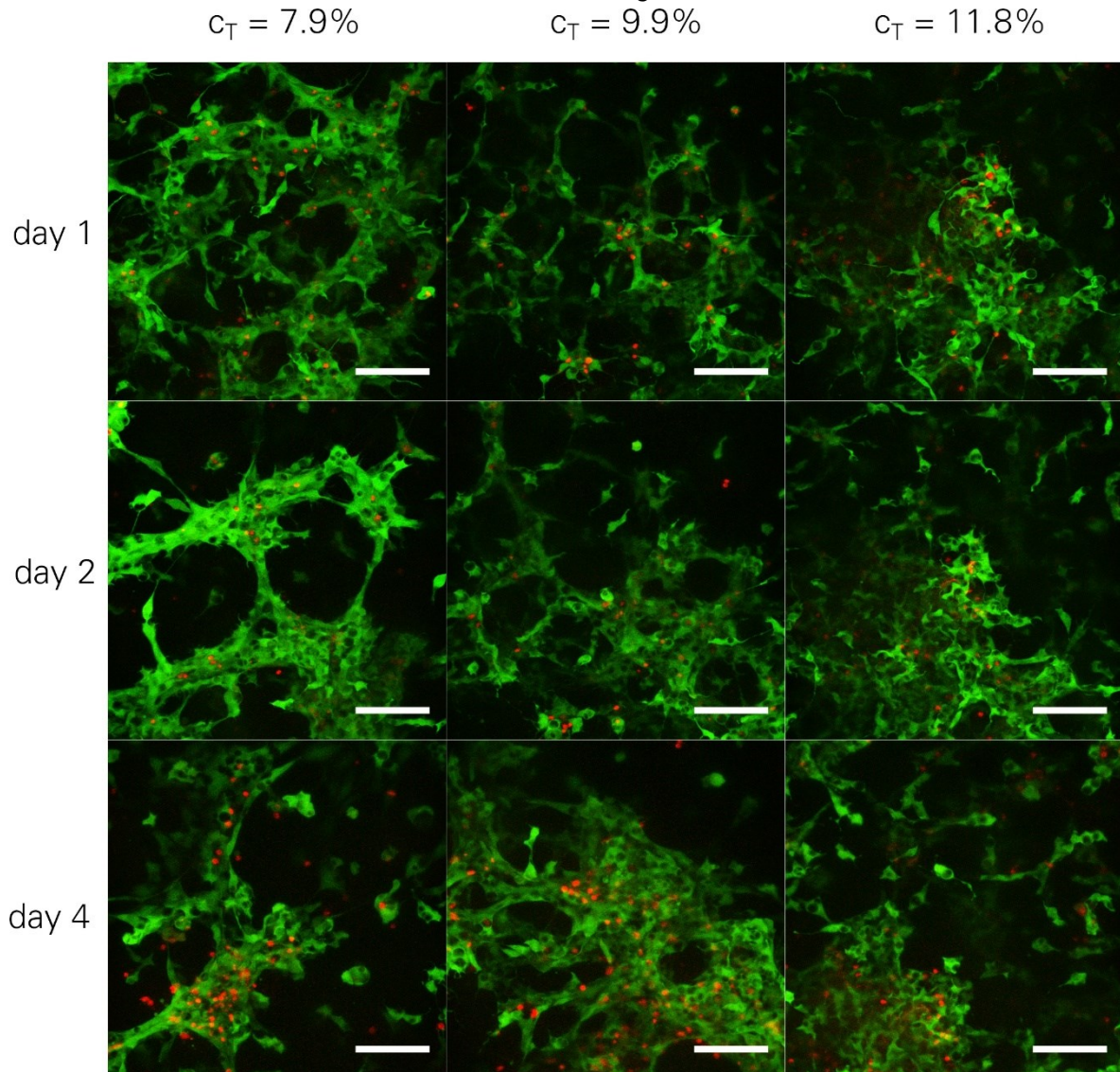


Figure 46: NIH3T3/GFP (green) survival over 4 days in PAAm hydrogel beads with different stiffness ($c_T = 7.9\%$, 9.9% and 11.8% respectively) and functionalized with PLL-Cy5. Dead cells were stained with $5\text{ }\mu\text{g/mL}$ propidium iodide. Maximum projections of representative confocal microscopy stacks, same settings for all images. Scale bar: $100\text{ }\mu\text{m}$.

fibroblasts in 3D over four days in differently stiff hydrogel bead scaffolds ($c_T = 7.9\%$, 9.9% and 11.8% respectively). After four days no massive cell death was observed. The acquired confocal stacks were of the same dimension for all time points for the respective position within the scaffold. Even though the respective imaging positions were initially saved and selected again for the next imaging session by using a motorized microscope table, the exact positions could not be adjusted based on the available slide holder. Thus, quantification of cell death over time based on these images was not representative. Microscopy settings were kept the same during image acquisition and image processing (increase of propidium iodide (PI) intensity) was done the same for all images.

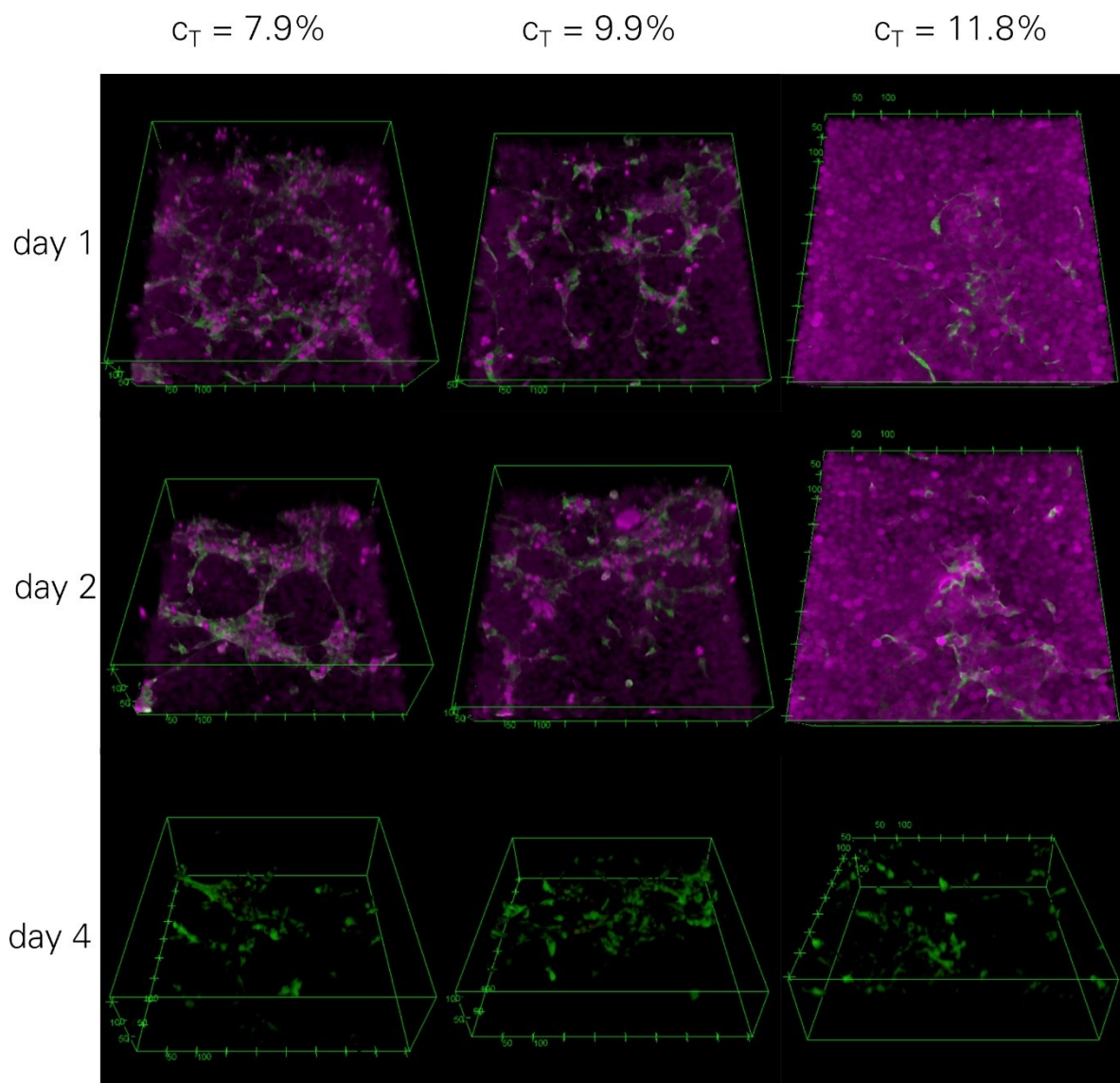


Figure 47: NIH3T3/GFP (green) network formation in PAAM hydrogel bead scaffolds functionalized with PLL-Cy5 (magenta) and different stiffness ($c_T = 7.9\%$, 9.9% and 11.8% respectively). 3D projections. Day 4 does not show beads as the fluorescence intensity was too low to be detected. Dead cells were stained with $5 \mu\text{g/mL}$ propidium iodide (red).

Figure 47 visualizes 3D projections of the same positions and time points already shown in Figure 46, but additionally with PLL-Cy5 functionalized PAAm hydrogel beads in magenta. It turned out that at day 4 the hydrogel beads were not able to be visualized anymore as the Cy5 was apparently bleached at this time point due to daily handling (medium exchange). In the 3D projections the cell network in the hydrogel bead scaffolds formed by NIH3T3/GFP fibroblasts can be seen. The fluorescence intensities of the hydrogel beads were not enhanced manually, resulting in differently bright hydrogel scaffolds for different stiffness, as already observed in chapter 4.4.

However, one can still clearly see how cells elongated and “wrapped” around hydrogel beads and formed connected cell clusters and networks. The bright magenta spots indicate hydrogel beads trapped in the cell clusters. Figure 48 shows more clearly how hydrogel beads were ensheathed by cells. Some hydrogel beads (examples indicated with white arrow) were deformed and compressed by the surrounding cells and resulting in an intensity increase due to the same number of fluorophores in a smaller volume. Deformed hydrogel beads have been observed for all used hydrogel bead compositions. A further characterization of number of deformed beads or the detailed deformation was not done so far.

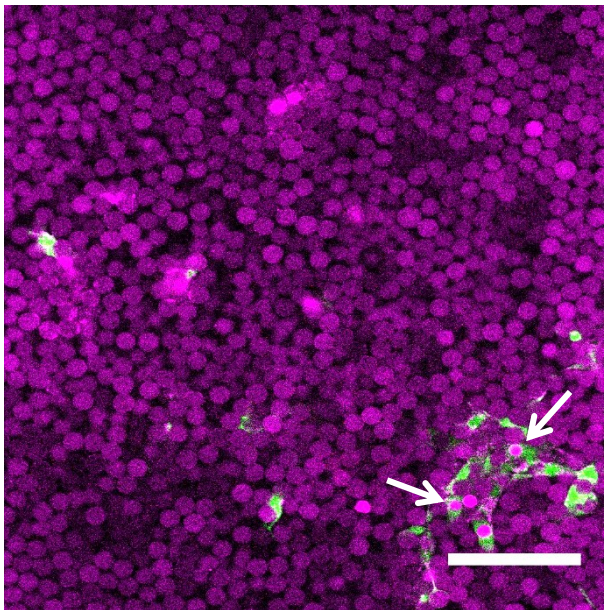


Figure 48: NIH3T3/GFP (green) in 3D PAAm hydrogel bead scaffold ($c_T = 9.9\%$) functionalized with PLL-Cy5 (magenta) after 24 h. Examples of deformed hydrogel beads are indicated with white arrows. Confocal microscopy slice; scale bar: 100 μm .

Initial cell migration studies were performed by seeding fibroblasts as layer between two hydrogel bead scaffolds of functionalized PAAm hydrogel beads with different stiffness ($c_T = 9.9\%$ vs. $c_T = 11.8\%$; 5 – 6 kPa vs. 11 – 12 kPa). Cell migration was then recorded over night by confocal time lapse imaging.

Figure 49 illustrates a single fibroblast migrating through a stiff PAAm hydrogel bead scaffold functionalized with PDL (50 $\mu\text{g}/\text{mL}$) ($c_T = 11.8\%$, 5 kPa). The individual maximum projections demonstrate how the cell interacted with the hydrogel beads and formed protrusion-like structures usually found

during adhesion-based cell migration [93,94]. The hydrogel beads served as 3D environment for the fibroblast indicated by the dark grey spot in the cell maximum projections, where the

cell shaped itself around the beads. The cell explored its environment also in z-direction, but was not visualized in these maximum projections.

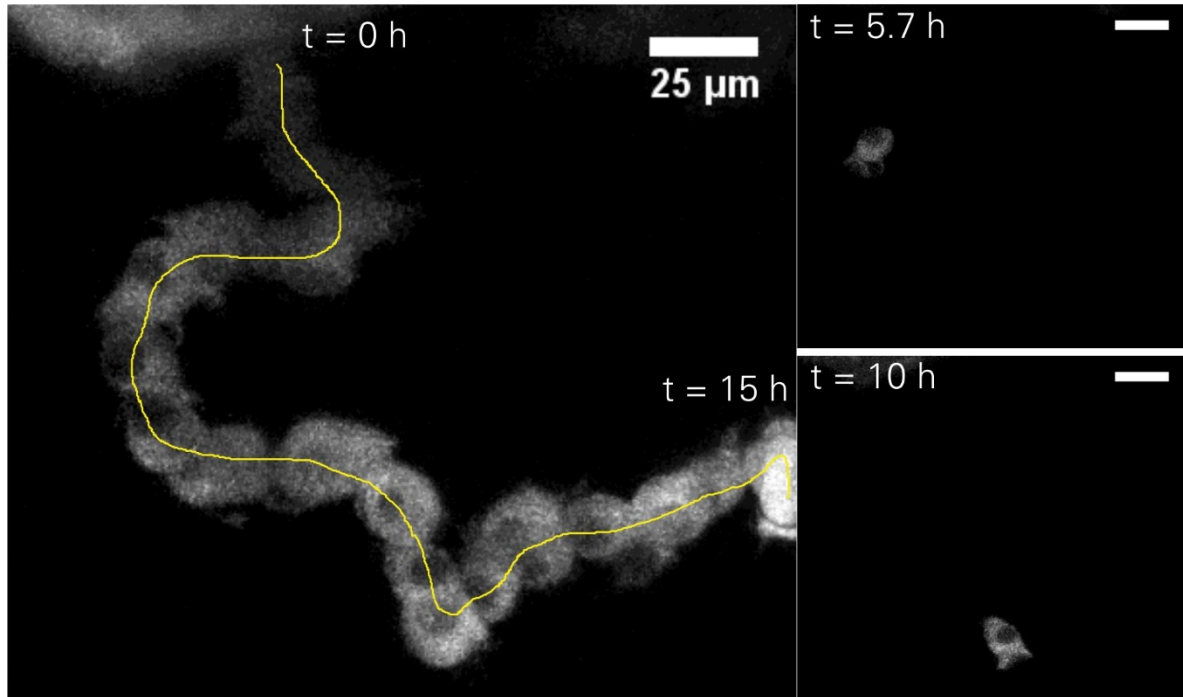


Figure 49: NIH3T3/GFP fibroblast migrating through PAAm hydrogel bead scaffold ($c_T = 11.8\%$) functionalized with PDL. Maximum projection and overlay of all 47 time points (time increment 20 min) with yellow line illustrating migration track as well as individual maximum projections for two selected time points. Scale bar: 25 μm .

While observing fibroblasts migrating through PDL functionalized PAAm hydrogel bead scaffolds, the question occurred how cells interact with the hydrogel beads and if the hydrogel beads were moved by migrating cells. Therefore, PLL-Cy5 functionalized PAAm hydrogel bead scaffolds were generated using the same compositions as before (i.e. $c_T = 9.9\%$ vs. $c_T = 11.8\%$; 5–6 kPa vs. 11–12 kPa). Figure 50A demonstrates how cells migrated at the scaffold interface (indicated by dashed line), when facing scaffolds with either a median Young's modulus of 6 kPa or 12 kPa in close vicinity to each other. The maximum projections were overlaid with each other over time (grey) with the starting point ($t = 0$ min) in green and the end point ($t = 912$ min) in red. So far, no clear migration direction of fibroblasts in these 3D hydrogel bead scaffolds was observed.

To overcome the disadvantages of missing details while overlaying maximum projections and to illustrate how single cells interact with the hydrogel beads, two close up montages were generated from selected areas (Figure 50A insets). Figure 50B and C show the same single confocal slice over time (see respective time stamp). Fibroblasts (green) interacted with the PLL-Cy5 functionalized PAAm hydrogel beads (magenta).

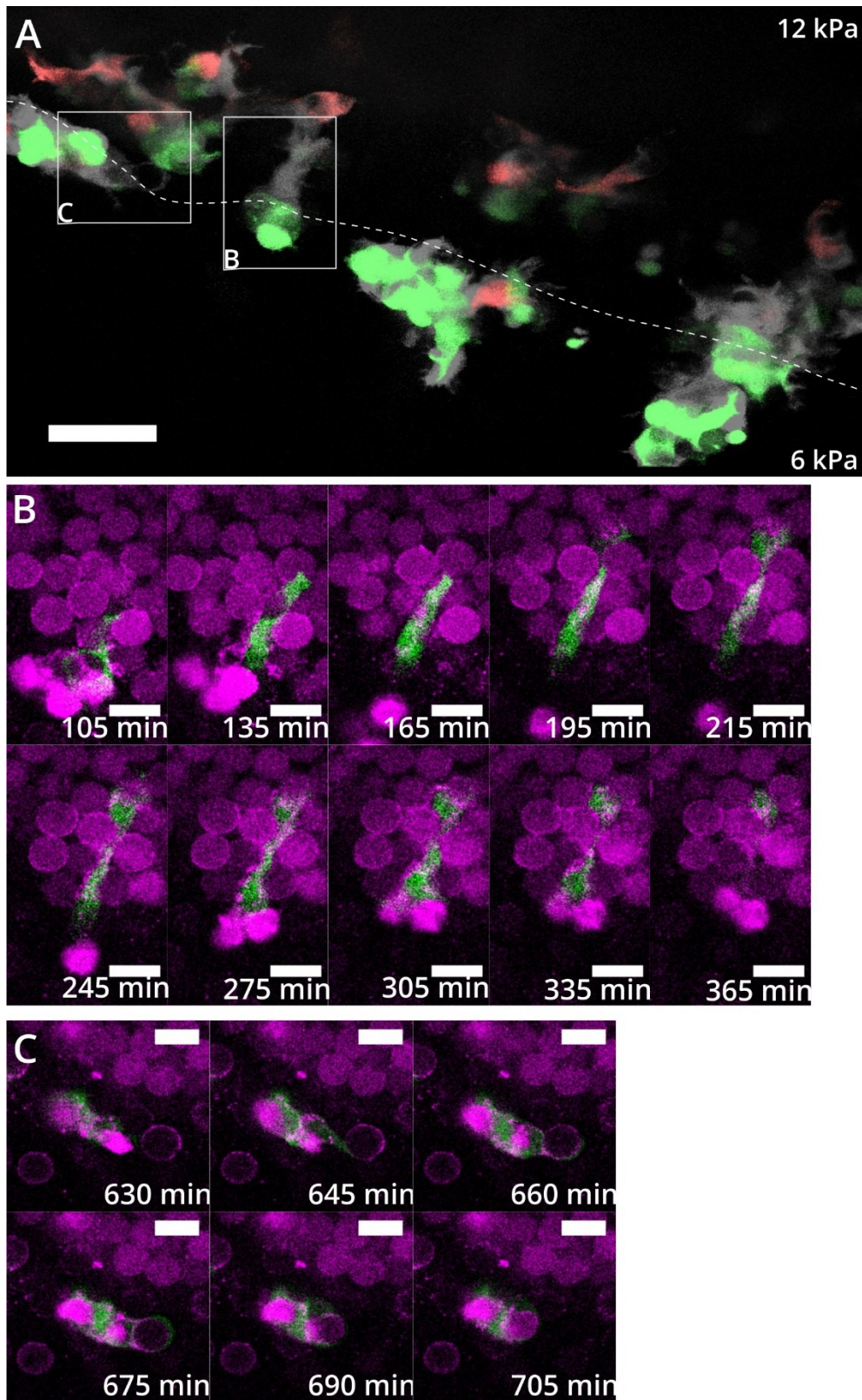


Figure 50: NIH3T3/GFP fibroblasts migrating through 3D PAAm hydrogel bead scaffolds functionalized with PLL-Cy5 (magenta) over 15 h at scaffold interface: $c_T = 9.9\%$ to 11.8% (dashed line) **A)** Maximum projection of fibroblast fluorescence signal for each time point and overlay of all time points (grey; time increment 15 min). $t = 0$ min: green; $t = 912$ min: red. Scale bar: 50 μm . **B, C)** Confocal slices of close ups of indicated areas in A) with fibroblasts (green) migrating through 3D PAAm hydrogel bead scaffold (magenta). Scale bar: 20 μm .

Fibroblasts attached to PAAm hydrogel beads and migrated into the stiff scaffold by elongation and pulling the rear behind them, indicated by the movement of the bright fluorescent hydrogel beads at the bottom of the images (Figure 50B). The cell then detached from these beads at $t = 535$ min as they could not be pulled further into the existing scaffold. Figure 50C illustrates that fibroblasts could also move hydrogel beads around, if the scaffold was not dense enough. Starting at $t = 645$ min a fibroblast attached to a compliant PAAm hydrogel bead (compliance was indicated by the weak fluorescent Cy5-signal) and pulled the bead towards the cell-bead cluster. Comparing the last two shown time points, the fluorescence intensity of the “collected” hydrogel bead increased, indicating a compression of the hydrogel bead by cellular forces. The acting cellular forces were not quantified further. The successful migration experiments demonstrated one difficulty already mentioned in the previous chapter. As soon as the stabilization time of the scaffold after production was below two hours or the stopper layer was too small, the scaffolds moved and the initially selected scaffold area drifted away. Thus, cell migration tracking needed further image processing when the cells of interest were still in the field of view. To re-adjust the time points, the stacks acquired for each position were corrected for a 3D drift over time by using a FIJI registration plugin and the dead cell nuclei stained with propidium iodide as registration points.

Furthermore, it was possible for the first time to demonstrate how fibroblasts migrate in 3D hydrogel bead scaffolds without any adhesion binding sites. NIH3T3/GFP fibroblasts were seeded randomly in PAAm hydrogel bead scaffolds with $c_T = 13.8\%$, $E = 6.6$ kPa (Figure 44A) and observed by confocal microscopy over-night. All cells showed a completely different morphology with their round shape compared to the ones observed in PLL-Cy5 coated, where they appeared elongated and spread. This indicated that fibroblasts were indeed not able to adhere on the PAAm hydrogel beads and a coating of PAAm beads with adhesion molecules was necessary to promote cell adhesions. Nevertheless, fibroblasts survived successfully within the non-functionalized PAAm hydrogel bead scaffolds. Some fibroblasts even used an amoeboid-like migration mode to move from one cell cluster to another (Figure 51). This migration behavior could be compared with already observed migration mode with low adhesion, i.e. absence of focal adhesions, and high cortical contractility [95].

This migration experiment demonstrated another strength of the developed 3D *in vitro* system as no other *in vitro* model is known where cell migration can be studied in 3D without active cell adhesions but defined porosity and stiffness.

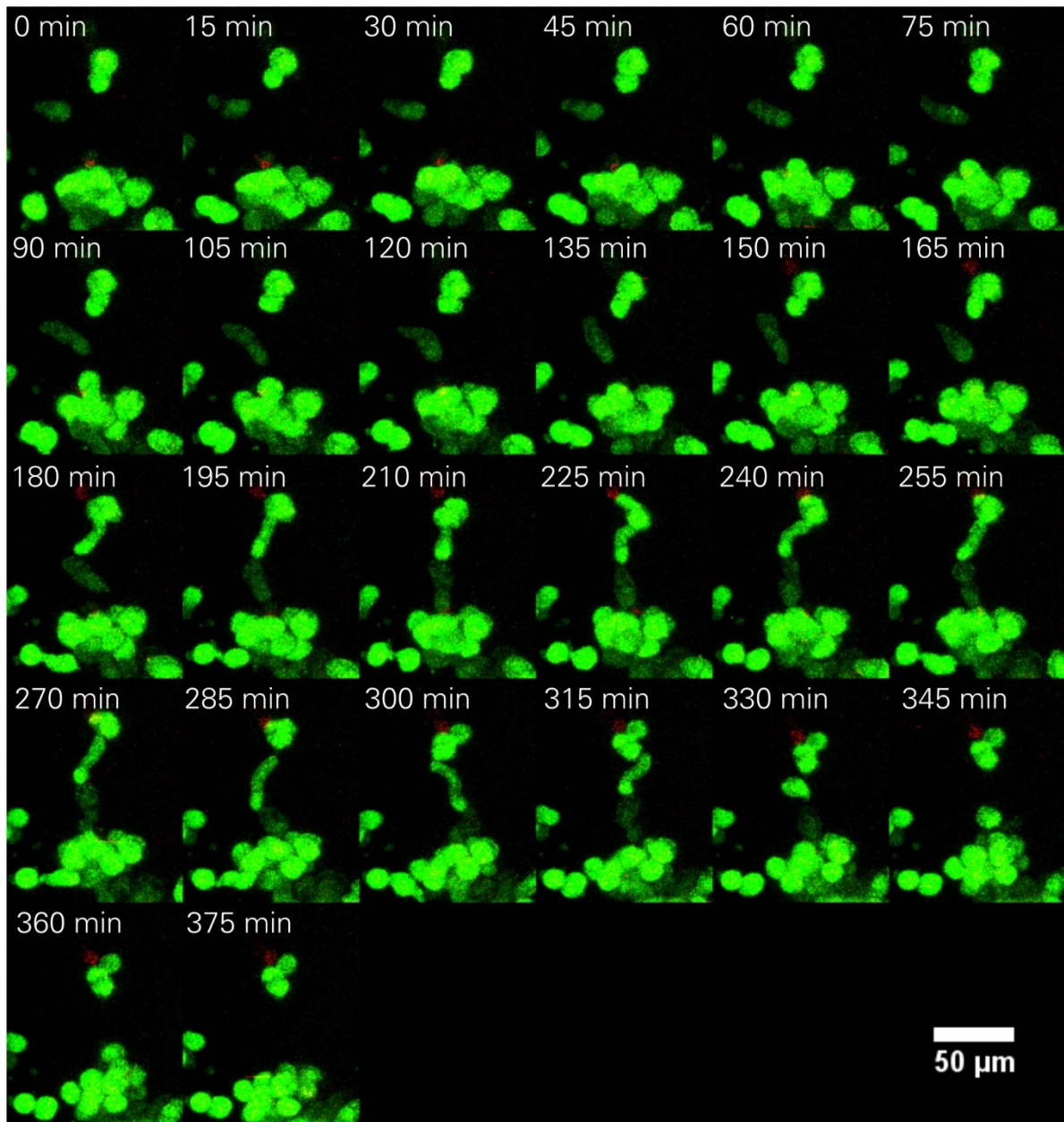


Figure 51: Maximum projection of NIH3T3/GFP (green) fibroblasts migrating in amoeboid-like migration mode through PAAm hydrogel bead stack ($c_T = 13.8\%$, $E = 6.6$ kPa) within a total imaging time of 15 h. Dead cells were stained with 5 $\mu\text{g}/\text{mL}$ PI (red). Scale bar: 50 μm .

5 Discussion and Concluding Remarks

With the aim to develop 3D scaffolds with hydrogel beads as scaffold building blocks and to decouple mechanical properties from porosity (and if possible active binding sites), a new cell culture method was developed from scratch. Necessary parameters for a culture device were defined and based on these, the commercially available ibidi μ -Slide^{IV} was established as suitable culture chamber. With simulations of the theoretical oxygen supply by diffusion and oxygen consumption of cells by maintenance and proliferation, it was determined that oxygen supply would be sufficient theoretically in this device. A filter combination of different materials (cellulose fibre filter, PMMA and agarose beads) was developed to ensure a successful generation of the actual hydrogel bead scaffold in the chosen device. Hydrogel beads of different materials were then investigated (reproducibility, stiffness range, fluorescent visualization, functionalization possibilities) and hydrogel bead scaffolds were generated with them acting as scaffold building blocks. The achieved scaffolds were characterized by fluorescence microscopy (stability, handling, regularity/porosity) and PAAm was chosen as the best material within the investigated ones to generate hydrogel bead scaffolds with tuneable stiffness and constant pore size. With these novel scaffolds that decoupled stiffness and porosity, initial cell culture experiments were successfully performed to check cell survival as well as cell attachment and migration. Differently stiff PAAm hydrogel beads were used to demonstrate the suitable application of the developed system for mechanosensitivity studies in 3D. Additionally, it was possible to generate 3D scaffolds with tuneable stiffness, constant pore size and no active binding sites to prevent cell adhesion. With this combination it was possible for the first time to study mechanosensitivity and cell migration of cells in 3D without active cell adhesions in scaffolds with decoupled porosity and stiffness.

During the development of the 3D *in vitro* cell culture method, two aspects appeared to be very prominent.

It was observed that the hydrogel beads could be moved around by cells when migrating through the scaffold, if the bead packing has not reached the close-packed structures Figure 45C. To generate stable scaffolds with close-packed structures as *in vitro* models, microbeads would either have to be filled into a confined space as done in the here presented project by using a channel geometry and additional "stoppers" or the microbeads have to be annealed in a suitable way. In the last decade it turned out that one of the biggest challenges in microbead based scaffolds was (and still is) the annealing of beads to generate stable

5 Discussion and Concluding Remarks

scaffolds [20]. This statement was as well observed in during the method development, where an intensive protocol optimization was necessary to generate stable PMMA filter scaffolds as well as stable hydrogel bead scaffolds.

One way to stabilize the here presented hydrogel bead scaffolds was to add another filter of either hydrogel beads or a fiber filter on top of the hydrogel scaffolds. By using a large layer of PAAm hydrogel beads with PLL-functionalization, it was tested whether these bead layer ("stopper layer") was already sufficient to hold the actual scaffolds in place. These "stopper layer" faded out as observed before. By using a large amount of beads, the hydrogel bead scaffolds were successfully hold in place and the fading could be prevented.

When different hydrogel beads would be used as scaffold building blocks, this method might not work. If this is the case and the actual scaffold used to study the mechanisms of interest cannot be annealed chemically without harming cells, another possibility would be that the "stopper layer" is chemically or physically annealed. Stiffness as well as exact pore size does not play a role for these layers as their only purpose is to hold the previously generated hydrogel bead scaffold in place. If another fiber filter should be used as stopper, it has to be kept in mind that the scaffold layers need to end at (or even in) the inlet as the fiber filter cannot be directly pushed into the channel due to geometrical limitations.

One example to chemically link hydrogel beads was presented by the group of Tatiana Segura, who developed covalently linked 3D hydrogel scaffolds as injectable scaffolds [45]. The resulting scaffolds were not varied in stiffness and were mainly used for *in vivo* applications (i.e. wound healing). Other gelation strategies that could be used to anneal hydrogel bead scaffolds were reviewed in 2016, also in combination with suitable hydrogel materials [83]. Generally, when choosing a chemical or physical strategy to anneal hydrogel beads, it is important to avoid cytotoxic conditions, if cells are incorporated into the scaffold prior annealing.

The second aspect was, that the chosen hydrogel bead size and the resulting pore size of the scaffold might have an effect on the cell behaviour. It has been shown for implants that an optimal pore size exists for tissue regeneration in dependence of the cell and tissue type [22]. Cell migration can be limited based on cell-scaffold properties to degrade the scaffold and the nucleus as migration-limiting compartment in small-porous scaffolds [77]. For fibroblasts, an optimal implant pore size was determined as 5 – 15 μm [22], which fits to the here presented scaffolds. If other cell types are going to be studied in the developed system, an adjustment of the hydrogel bead diameter and thereby of the scaffold pore size might be necessary.

One big challenge in using hydrogels as scaffold material for mechanosensitivity applications is the effect adhesion molecules have on cell behaviour. It has been shown, that the amount and type of adhesion sites available for cells affected. Migration speed and spreading area varied for fibroblasts growing on PAAm substrates coated with different amounts of RGD-motifs or fibronectin (constant stiffness) [96]. For human mesenchymal stem cells it was observed that adhesion as well as focal adhesion formation was changed when grown on differently stiff PDMS substrates coated with fibronectin [97]. It has also been observed that the amount of laminin on differently stiff PAAm substrates coated with PDL and Matrigel was constant while axonal sprouting was affected by the stiffness change in 2D [35].

Thus, one remaining question is whether adhesion sites (i.e. by PLL coating) remain constant on PAAm hydrogel beads with increasing stiffness. To analyze the amount of bound PLL-Cy5 was to quantify the fluorescence already available by the label of the used adhesion molecule. Confocal images illustrated that PAAm hydrogel beads were completely stained in the bulk with PLL-Cy5 (Figure 38A-C). We demonstrated, that the functionalization started at the surface of the beads [48]. Therefore, it was plausible that the surface polymer chains were saturated with PLL-Cy5, when the bulk of the bead was also stained completely and evenly. By using RT-fDC observations from the confocal microscopy experiments were confirmed that PLL-Cy5 intensity increased with higher total monomer concentration (c_T) (i.e. higher stiffness) (Figure 38). However, it was not possible to quantify a direct correlation within single hydrogel bead batches between stiffness variation and fluorescence intensity variation. Additionally, the number of available adhesion points on the bead surface remained unknown. Another possibility to quantify the amount of available adhesion molecules would be to use western blots together with a suitable antibody. Using this method, Flanagan et al. determined the amount of laminin on Matrigel coatings on differently stiff 2D PAAm gels [35]. However, it would display the total amount of the PLL-Cy5 incorporated into the beads and not only the molecules on the bead surface available for cell adhesions. Thus, the results would be complementary to the RT-fDC results.

Another labelling technique could be to use radioactive adhesion molecules. For 2D gels the number of adhesion molecules per area was defined by using radioactivity labelling of the adhesion molecules [96]. Based on the radioactivity labelling the total amount of radioactivity (i.e. adhesion molecules) was correlated with the gel area, but gel thickness was not taken into account. Thus, the actual adhesion points on the surface remained unknown. Therefore, also the radioactivity labelling appeared not to be suitable for beads or curved objects to determine the molecules bound to the surface.

5 Discussion and Concluding Remarks

In general, the difference between labels on 2D hydrogels and hydrogel beads, where the surfaces serve as attachment area for cells, is, that the number of accessible adhesion points for cells on the bead surface are hard to distinguish due to small curvature of the beads.

The cell survival study demonstrated for compliant PAAm hydrogel beads ($c_T = 7.9\%$) that cells attached well to the beads and formed cell clusters. However, so far it could not be determined whether the different amounts of bound PLL-Cy5 were affecting cell behaviour. To produce PAAm hydrogel beads with the same amount of bound adhesion molecules but different stiffness, it will be necessary to perform hydrogel bead functionalization with different concentrations of PLL-Cy5 and differently stiff beads to generate a standard curve. With this, the amount of bound PLL (determined by fluorescence intensity) can then be correlated with applied PLL concentration and hydrogel bead stiffness. Based on this correlation, hydrogel beads with different stiffness but same PLL amount can be chosen. Furthermore, hydrogel bead scaffolds of the same stiffness but with different PLL amounts could be generated to compare the effect of PLL concentration on cellular behaviour with the developed method of this study.

Successful cell survival and cell migration was demonstrated for fibroblasts within the developed 3D model for scaffolds of different stiffness and same porosity as well as with and without adhesion molecules present.

Fibroblast migration in 3D is known to work in at least three different ways – lobopodial, lamellipodial which is also observed in 2D, and amoeboid mode (also called blebbing [94]) [93]. The first two are integrin-based adhesion modes, which are also called mesenchymal migration modes, whereas the latter one is generally used for integrin-independent or adhesion-independent migration modes [98].

Compared to 2D migratory behaviour where focal adhesions are crucial, it was questioned whether 3D cell migration depended mainly on focal adhesions [99]. In 2011 it was possible to visualize distinct focal adhesion complexes in 3D in collagen gels [100]. On the contrary, others found only a diffuse signal of the proteins involved in forming focal adhesions in 3D collagen gels [101]. Over different adhesion-dependent fibroblast migration experiments, it appeared that a specific durotactic behaviour (i.e. cell accumulation in stiffer environments) is conserved across 2D and 3D [2,31,32,38,99]. In Figure 50A a similar durotactic behavior might be existing when the amount of cells migrating to the stiffer scaffolds are compared with the one migrating to the compliant scaffold (i.e. red marks illustrate final time point). However, this was just an initial successful experiment and repetitions are needed to verify this observation. Additionally, cells might have migrated out of the acquired stack region towards

5 Discussion and Concluding Remarks

the bottom and were thereby not displayed anymore at the end, as the starting height of the z-stack was at least 10 μm above the channel bottom. Figure 50B, C illustrate well that the fibroblasts adhere to the PAAm hydrogel beads (functionalized with PLL-Cy5) and interact with the hydrogel beads. The cell in Figure 50B seems to have squeezed through the pores between the hydrogel beads without moving them around in the dense scaffold, indicating a proper packing and suitable resulting pore sizes for migration [22,77].

The amoeboid-like migration of fibroblasts that was observed within non-functionalized PAAm hydrogel scaffolds (Figure 51), illustrates another application of the developed method. Focal adhesion-independent migration modes are promoted by different cell-intrinsic and -extrinsic factors. Cells lacking integrins or expressing integrins at very low levels as well as high actomyosin contractility favour non-adhesive migration as well as high confinement levels [93,98]. Since the substrate interactions during amoeboid migration are poorly understood, this new method could provide a tool to gain insights. Four possible force transmission mechanisms have been proposed for focal adhesion-independent migration: swimming migration, cell-substrate intercalation, chimneying force transmission and flow-friction-driven force transmission [98]. The migration seen in Figure 51 could not be assigned to any of these as the hydrogel beads were not visible. Thus, it is not known whether the cells pushed the hydrogel beads around or swam through pores in the scaffold.

Other studies for 3D migration without adhesion are usually performed in confinements in stiff PDMS microfluidic channels [102] or in sandwich models [95,103,104]. First known mechanosensitivity studies for non-adhesive migration were performed by Pebworth et al. in 2014. Cancer cells were grown on plastic and overlaid with alginate of different concentration (i.e. different stiffness). The alginate gels did not present any ligands for cell adhesions. The cancer cells migrated less into stiffer alginate layers [105]. However, this method included the already discussed problem that stiffness and porosity are coupled within bulk gels. With the developed 3D scaffolds, this decoupling opens the field to study 3D mechanosensitivity and 3D migration.

Initial cell migration experiments were further analyzed using cell tracking algorithms provided by the FIJI plugin "TrackMate" [106]. With the help of an additional extension "Track analysis", it is possible to determine the total travel distance in 3D as well as migration speeds. The "TrackMate" was developed to track single particles and might have issues with tracking spread cells in 3D, as the algorithms are optimized for spot-like objects.

5 Discussion and Concluding Remarks

So far, cell tracking has only been tested using GFP-labelled fibroblasts, being fluorescent over the entire cell. It would be feasible to use nuclear dyes or other cellular stains that improves discrimination of single cells in 3D and in a cell collective during migration. In this project two nuclear dyes, Hoechst 33258 (3 μM) and Vybrant™ DyeCycle™ Ruby stain (5 μM), have been tested for over-night time-lapse imaging sessions. For Hoechst, cell death was observed already after 3–4 h. This was expected as the fluorophore emitted blue fluorescence when excited with UV light. UV light itself damages DNA and the binding of Hoechst to the DNA inhibits cell processes [107]. For the Vybrant dye, it turned out that cell death was increased drastically for the light-exposed areas of the scaffold compared to the areas that haven't been exposed to light. Imaging frequency was around 3–4 3D stacks per hour with an acquisition time of 3–5 min per stack and the application of a high resonant scanner and a line average of 8 lines per frame. The experiment was performed for 16 h. The intensive light exposure of DNA interacting fluorophores reached apparently the phototoxicity level for the cells [108], although Invitrogen stated a low cytotoxicity (but not explicitly for long-term live imaging). Alternatively, DRAQ5 could be checked, as no photobleaching was observed in a study. However, experiences in long-term live imaging was not reported [107]. To decrease phototoxicity in general, fluorophores of the (far) red spectrum should be preferred as the transported energy of these light waves is lower than for blue light. Another possibility could be SiR-Hoechst as DNA stain that is suitable for long-term live imaging at concentrations below 1 μM in the imaging medium [109]. Even though this staining mechanism is also based on the minor grooves as Hoechst does, it is supposed to be not as cytotoxic as Hoechst is. To decrease cytotoxicity, any staining not interfering with the cellular DNA would be recommended.

Live imaging of cell migration within the developed 3D scaffolds can become problematic for cells deep in the scaffolds as light is scattered a lot in the dense colloidal crystal and thereby areas with depth of more than 200 μm become very blurry. To overcome this problem, refractive index matched cell culture medium could be used by using Iodixanol as supplement to the culture medium [92]. It has been demonstrated that Iodixanol does not affect cell growth or death in cultured HeLa cells. However, it has to be kept in mind that this chemical might alter cell behaviour, even though it is thought not to be likely. Fixation and immunohistochemistry protocols to stain cells in the system are possible without destroying the system. With the help of filter paper to accelerate liquid exchange within the scaffold, washing steps can be performed within appropriate time and only small amounts of liquid

5 Discussion and Concluding Remarks

(~ 150 – 200 μL) are needed to completely exchange the liquid within one channel (i.e. one experimental condition) of the chamber.

For the simulation of the oxygen supply a random cell distribution was assumed. As the cells showed a tendency to form cell clusters by cell migration, this assumption was not valid for longer cultivation times than 24 h. Thus, implementation of large cell clusters might change the resulting oxygen profiles. Peter Buchwald demonstrated necrotic cores for pancreatic islets with a diameter of 150 μm and larger for static culture conditions [62]. The implementation of cell growth took only oxygen limitations into account. Cell growth and proliferation might also be affected due to limited amount of glucose. Cell death was also not considered. This could be done by a step-down function [62]. Different cell types also have different oxygen consumption rates [67]. Implementing a discontinuous flow to supply the system regularly with fresh medium and more oxygen is possible with the developed method. The implementation of a continuous flow, which is necessary for certain cell types (e.g. endothelial cells), is also possible. Further oxygen diffusion simulations could be performed to study the effects of different flow settings on oxygen supply. Additionally, it would be interesting to perform experiments to check the oxygen concentration distribution in the 3D system. This could be done by oxygen-sensitive nanoparticles, that are incorporated into the cells by endocytosis (e.g. NanO₂ from ibidi). Other possibilities to quantify the oxygen distribution in 3D could either be water-soluble molecules or nanobeads embedded in the hydrogel [110]. Oxygen detection can be based on phosphorescence quenching by oxygen [111,112], that will be optically detected by lifetime imaging, or by intensity-based imaging.

For a better understanding of the system, the hydrogel bead scaffold structure needs further optimization to demonstrate its reproducibility, not only for functionalized hydrogel beads, but also for non-functionalized ones (i.e. without adhesion molecules). Therefore, the staining needs to be optimized by using new prepared PAAm hydrogel beads with NHS-functionalization as well as exact refractive index matched medium. For non-functionalized PAAm beads, a way to visualize the 3D structure has to be developed. One possibility would be to use already fluorescently labelled acrylamide monomers to directly produce fluorescent PAAm hydrogel beads. Another way could be to functionalize PAAm beads with fluorescent molecules without adhesion molecules present. Therefore, a fluorescent molecule with amine groups included would be needed, as these are interacting with the activated NHS-

5 Discussion and Concluding Remarks

groups to form covalent bonds. By this, fluorescent PAAm hydrogel beads could be produced to generate PAAm hydrogel bead scaffolds without adhesion sites.

Furthermore, other materials like covalent starPEG heparin gels could be tested as hydrogel bead material to even enhance the broad application range of the developed system.

This innovative new approach of 3D *in vitro* hydrogel bead scaffolds opens multiple opportunities to investigate cell migration and mechanosensitivity in 3D and unravel underlying mechanisms. PAAm hydrogel bead scaffolds with layers of different Young's moduli (e.g. 3 kPa, 6 kPa and 12 kPa and even higher) can be generated to investigate cell mechanosensitivity and cell migration in 3D with constant scaffold porosity. By using non-functionalized and functionalized PAAm hydrogel beads, a direct comparison of mechanosensitivity with and without adhesion molecules present is now possible. Thus, adhesion-independent cell migration studies in defined 3D microenvironments can now be performed to identify and better understand cell migration mechanisms in confinements without adhesive molecules. In addition, these scaffolds can be used to study mechanosensitivity in 3D without integrin-based cell migration.

6 Bibliography

1. Engler AJ, Sen S, Sweeney HL, Discher DE: **Matrix elasticity directs stem cell lineage specification.** *Cell* 2006, **126**:677–689.
2. Lo CM, Wang HB, Dembo M, Wang Y: **Cell movement is guided by the rigidity of the substrate.** *Biophysical Journal* 2000, **79**:144–152.
3. Discher DE, Janmey P, Wang Y: **Tissue cells feel and respond to the stiffness of their substrate.** *Science* 2005, **310**:1139–1143.
4. Moshayedi P, Ng G, Kwok JC, Yeo GS, Bryant CE, Fawcett JW, Franze K, Guck J: **The relationship between glial cell mechanosensitivity and foreign body reactions in the central nervous system.** *Biomaterials* 2014, **35**:3919–3925.
5. Hoarau-Véchet J, Rafii A, Touboul C, Pasquier J: **Halfway between 2D and Animal Models: Are 3D Cultures the Ideal Tool to Study Cancer-Microenvironment Interactions?** *International journal of molecular sciences* 2018, **19**:181.
6. Duval K, Grover H, Han L-H, Mou Y, Pegoraro AF, Fredberg J, Chen Z: **Modeling Physiological events in 2D vs. 3D cell culture.** *Physiology* 2017, **32**:266–277.
7. Liu Z, Tang M, Zhao J, Chai R, Kang J: **Looking into the Future: Toward Advanced 3D Biomaterials for Stem-Cell-Based Regenerative Medicine.** *Advanced Materials* 2018, [no volume].
8. Tibbitt MW, Anseth KS: **Hydrogels as extracellular matrix mimics for 3D cell culture.** *Biotechnology and bioengineering* 2009, **103**:655–663.
9. Pampaloni F, Reynaud EG, Stelzer EH: **The third dimension bridges the gap between cell culture and live tissue.** *Nature reviews Molecular cell biology* 2007, **8**:839.
10. Amelian A, Wasilewska K, Megias D, Winnicka K: **Application of standard cell cultures and 3D in vitro tissue models as an effective tool in drug design and development.** *Pharmacological Reports* 2017, **69**:861–870.
11. Langhans SA: **Three-dimensional in vitro cell culture models in drug discovery and drug repositioning.** *Frontiers in Pharmacology* 2018, **9**:6.
12. Eyckmans J, Chen CS: **3D culture models of tissues under tension.** *J Cell Sci* 2017, **130**:63–70.
13. Simian M, Bissell MJ: **Organoids: a historical perspective of thinking in three dimensions.** *J Cell Biol* 2016, [no volume].
14. Baker BM, Chen CS: **Deconstructing the third dimension - how 3D culture microenvironments alter cellular cues.** *Journal of cell science* 2012, **125**:3015–3024.

15. Griffith LG, Swartz MA: **Capturing complex 3D tissue physiology in vitro**. *Nature reviews Molecular cell biology* 2006, **7**:211.
16. Owen SC, Shoichet MS: **Design of three-dimensional biomimetic scaffolds**. *Journal of Biomedical Materials Research Part A* 2010, **94**:1321–1331.
17. Dado D, Levenberg S: **Cell-scaffold mechanical interplay within engineered tissue**. In *Seminars in cell & developmental biology*. 2009:656–664.
18. Ruprecht V, Monzo P, Ravasio A, Yue Z, Makhija E, Strale PO, Gauthier N, Shivashankar G, Studer V, Albiges-Rizo C, et al.: **How cells respond to environmental cues - insights from bio-functionalized substrates**. *J Cell Sci* 2017, **130**:51–61.
19. Dutta RC, Dutta AK: **Cell-interactive 3D-scaffold; advances and applications**. *Biotechnology advances* 2009, **27**:334–339.
20. Gupta V, Khan Y, Berkland CJ, Laurencin CT, Detamore MS: **Microsphere-Based Scaffolds in Regenerative Engineering**. *Annual review of biomedical engineering* 2017, **19**:135–161.
21. Yang S, Leong K-F, Du Z, Chua C-K: **The design of scaffolds for use in tissue engineering. Part II. Rapid prototyping techniques**. *Tissue Eng.* 2002, **8**:1–11.
22. Yang S, Leong K-F, Du Z, Chua C-K: **The design of scaffolds for use in tissue engineering. Part I. Traditional factors**. *Tissue engineering* 2001, **7**:679–689.
23. *Comprehensive biomaterials*. Elsevier; 2011.
24. Kulicke W-M, Nottelmann H: **Structure and swelling of some synthetic, semisynthetic, and biopolymer hydrogels**. In *Advances in Chemistry*. ACS Publications; 1989.
25. Shan J, Chi Q, Wang H, Huang Q, Yang L, Yu G, Zou X: **Mechanosensing of cells in 3D gel matrices based on natural and synthetic materials**. *Cell biology international* 2014, **38**:1233–1243.
26. Trappmann B, Chen CS: **How cells sense extracellular matrix stiffness: a material's perspective**. *Current opinion in biotechnology* 2013, **24**:948–953.
27. Vincent L, Engler A: **Effect of substrate modulus on cell function and differentiation**. *Comprehensive biomaterials* 2011, **5**.
28. Lee SH, Shim KY, Kim B, Sung JH: **Hydrogel-based three-dimensional cell culture for organ-on-a-chip applications**. *Biotechnology progress* 2017, **33**:580–589.
29. Her GJ, Wu H-C, Chen M-H, Chen M-Y, Chang S-C, Wang T-W: **Control of three-dimensional substrate stiffness to manipulate mesenchymal stem cell fate toward neuronal or glial lineages**. *Acta biomaterialia* 2013, **9**:5170–5180.

30. Kothapalli CR, Kamm RD: **3D matrix microenvironment for targeted differentiation of embryonic stem cells into neural and glial lineages.** *Biomaterials* 2013, **34**:5995–6007.
31. Hadjipanayi E, Mudera V, Brown RA: **Guiding cell migration in 3D: a collagen matrix with graded directional stiffness.** *Cell Motil. Cytoskeleton* 2009, **66**:121–8.
32. Stowers RS, Allen SC, Suggs LJ: **Dynamic phototuning of 3D hydrogel stiffness.** *Proceedings of the National Academy of Sciences* 2015, **112**:1953–1958.
33. Ehrbar M, Sala A, Lienemann P, Ranga A, Mosiewicz K, Bittermann A, Rizzi S, Weber F, Lutolf M: **Elucidating the role of matrix stiffness in 3D cell migration and remodeling.** *Biophysical journal* 2011, **100**:284–293.
34. Georges PC, Miller WJ, Meaney DF, Sawyer ES, Janmey PA: **Matrices with compliance comparable to that of brain tissue select neuronal over glial growth in mixed cortical cultures.** *Biophysical journal* 2006, **90**:3012–3018.
35. Flanagan LA, Ju Y-E, Marg B, Osterfield M, Janmey PA: **Neurite branching on deformable substrates.** *Neuroreport* 2002, **13**:2411–5.
36. Balgude A, Yu X, Szymanski A, Bellamkonda R: **Agarose gel stiffness determines rate of DRG neurite extension in 3D cultures.** *Biomaterials* 2001, **22**:1077–1084.
37. Huang G, Wang L, Wang S, Han Y, Wu J, Zhang Q, Xu F, Lu TJ: **Engineering three-dimensional cell mechanical microenvironment with hydrogels.** *Biofabrication* 2012, **4**:042001.
38. Miron-Mendoza M, Seemann J, Grinnell F: **The differential regulation of cell motile activity through matrix stiffness and porosity in three dimensional collagen matrices.** *Biomaterials* 2010, **31**:6425–6435.
39. Kotov NA, Liu Y, Wang S, Cumming C, Eghtedari M, Vargas G, Motamedi M, Nichols J, Cortiella J: **Inverted colloidal crystals as three-dimensional cell scaffolds.** *Langmuir* 2004, **20**:7887–92.
40. Velev OD, Lenhoff AM: **Colloidal crystals as templates for porous materials.** *Current opinion in colloid & interface science* 2000, **5**:56–63.
41. Da Silva J, Lautenschläger F, Sivaniah E, Guck JR: **The cavity-to-cavity migration of leukaemic cells through 3D honey-combed hydrogels with adjustable internal dimension and stiffness.** *Biomaterials* 2010, **31**:2201–2208.
42. Pautot S, Wyart C, Isacoff EY: **Colloid-guided assembly of oriented 3D neuronal networks.** *Nature methods* 2008, **5**:735–740.
43. Staruch RM, Glass GE, Rickard R, Hettiaratchy SP, Butler PE: **Injectable Pore-Forming Hydrogel Scaffolds for Complex Wound Tissue Engineering: Designing and Controlling Their Porosity and Mechanical Properties.** *Tissue Engineering Part B: Reviews* 2017, **23**:183–198.

44. Smith AW, Segar CE, Nguyen PK, MacEwan MR, Efimov IR, Elbert DL: **Long-term culture of HL-1 cardiomyocytes in modular poly (ethylene glycol) microsphere-based scaffolds crosslinked in the phase-separated state.** *Acta biomaterialia* 2012, **8**:31–40.
45. Griffin DR, Weaver WM, Scumpia PO, Di Carlo D, Segura T: **Accelerated wound healing by injectable microporous gel scaffolds assembled from annealed building blocks.** *Nature materials* 2015, [no volume].
46. Sideris E, Griffin DR, Ding Y, Li S, Weaver WM, Di Carlo D, Hsiai T, Segura T: **Particle hydrogels based on hyaluronic acid building blocks.** *ACS Biomaterials Science & Engineering* 2016, **2**:2034–2041.
47. Nih LR, Sideris E, Carmichael ST, Segura T: **Injection of Microporous Annealing Particle (MAP) Hydrogels in the Stroke Cavity Reduces Gliosis and Inflammation and Promotes NPC Migration to the Lesion.** *Advanced Materials* 2017, **29**.
48. Girardo S, Träber N, Wagner K, Cojoc G, Herold C, Goswami R, Schlußler R, Abuhattum S, Taubenberger A, Reichel F, et al.: **Standardized microgel beads as elastic cell mechanical probes.** *J. Mater. Chem. B* 2018, **6**:6245–6261.
49. Schindelin J, Arganda-Carreras I, Frise E, Kaynig V, Longair M, Pietzsch T, Preibisch S, Rueden C, Saalfeld S, Schmid B, et al.: **Fiji: an open-source platform for biological-image analysis.** *Nature methods* 2012, **9**:676.
50. Glaubitz M, Medvedev N, Pussak D, Hartmann L, Schmidt S, Helm CA, Delcea M: **A novel contact model for AFM indentation experiments on soft spherical cell-like particles.** *Soft matter* 2014, **10**:6732–6741.
51. Spencer LA, Melo RCN, Perez SAC, Weller PF: **A gel-based dual antibody capture and detection method for assaying of extracellular cytokine secretion: EliCell.** *Methods Mol. Biol.* 2005, **302**:297–314.
52. Wieduwild R, Krishnan S, Chwalek K, Boden A, Nowak M, Drechsel D, Werner C, Zhang Y: **Noncovalent Hydrogel Beads as Microcarriers for Cell Culture.** *Angewandte Chemie International Edition* 2015, **54**:3962–3966.
53. Rosendahl P, Plak K, Jacobi A, Kraeter M, Toepfner N, Otto O, Herold C, Winzi M, Herbig M, Ge Y, et al.: **Real-time fluorescence and deformability cytometry.** *Nature Methods* 2018, **15**:355–358.
54. Crusz SA, Popat R, Rybtke MT, Cámara M, Givskov M, Tolker-Nielsen T, Diggie SP, Williams P: **Bursting the bubble on bacterial biofilms: a flow cell methodology.** *Biofouling* 2012, **28**:835–42.
55. Tolker-Nielsen T, Sternberg C: **Growing and analyzing biofilms in flow chambers.** *Current protocols in microbiology* 2011, doi:10.1002/9780471729259.mc01b02s21.
56. Taylor WG, Camalier RF, Sanford KK: **Density-dependent effects of oxygen on the growth of mammalian fibroblasts in culture.** *Journal of Cellular Physiology* 1978,

- 95:33–40.**
57. Csete M: **Oxygen in the cultivation of stem cells.** *Ann. N. Y. Acad. Sci.* 2005, **1049:1–8.**
 58. DIN: *DIN 53380-2: Prüfung von Kunststoffen - Bestimmung der Gasdurchlässigkeit.* [date unknown].
 59. DIN: *DIN 53380-3 Bestimmung der Gasdurchlässigkeit.* [date unknown].
 60. Erwin Baur TAONR: **Saechtling Kunststoff Taschenbuch.** 2013, [no volume].
 61. Guaccio A, Borselli C, Oliviero O, Netti PA: **Oxygen consumption of chondrocytes in agarose and collagen gels: a comparative analysis.** *Biomaterials* 2008, **29:1484–93.**
 62. Buchwald P: **FEM-based oxygen consumption and cell viability models for avascular pancreatic islets.** *Theoretical Biology and Medical Modelling* 2009, **6:5.**
 63. Jamnongwong M, Loubiere K, Dietrich N, Hébrard G: **Experimental study of oxygen diffusion coefficients in clean water containing salt, glucose or surfactant: consequences on the liquid-side mass transfer coefficients.** *Chemical engineering journal* 2010, **165:758–768.**
 64. Richter A, Sanford KK, Evans VJ: **Influence of oxygen and culture media on plating efficiency of some mammalian tissue cells.** *Journal of the National Cancer Institute* 1972, **49:1705–1712.**
 65. Lide DR: *CRC Handbook of Chemistry and Physics, 85th Edition.* CRC Press; 2004.
 66. Buchwald P: **Exploratory FEM-based multiphysics oxygen transport and cell viability models for isolated pancreatic islets.** In *Proceedings of the COMSOL Conference 2008 Boston.* 2008.
 67. Wagner BA, Venkataraman S, Buettner GR: **The rate of oxygen utilization by cells.** *Free Radic. Biol. Med.* 2011, **51:700–12.**
 68. Streeter I, Cheema U: **Oxygen consumption rate of cells in 3D culture: the use of experiment and simulation to measure kinetic parameters and optimise culture conditions.** *Analyst* 2011, **136:4013–4019.**
 69. Colom A, Galgoczy R, Almendros I, Xaubet A, Farré R, Alcaraz J: **Oxygen diffusion and consumption in extracellular matrix gels: implications for designing three-dimensional cultures.** *J Biomed Mater Res A* 2014, **102:2776–84.**
 70. Hulst AC, Hens HJH, Buitelaar RM, Tramper J: **Determination of the effective diffusion coefficient of oxygen in gel materials in relation to gel concentration.** *Biotechnology Techniques* 1989, **3:199–204.**
 71. Croll TI, Gentz S, Mueller K, Davidson M, O'Connor AJ, Stevens GW, Cooper-White JJ: **Modelling oxygen diffusion and cell growth in a porous, vascularising**

- scaffold for soft tissue engineering applications.** *Chemical Engineering Science* 2005, **60**:4924–4934.
72. Monod J: **The growth of bacterial cultures.** *Annual Reviews in Microbiology* 1949, **3**:371–394.
73. Korin N, Bransky A, Dinnar U, Levenberg S: **A parametric study of human fibroblasts culture in a microchannel bioreactor.** *Lab on a Chip* 2007, **7**:611–617.
74. Staudt T, Lang MC, Medda R, Engelhardt J, Hell SW: **2,2'-thiodiethanol: a new water soluble mounting medium for high resolution optical microscopy.** *Microsc. Res. Tech.* 2007, **70**:1–9.
75. Vickreva O, Kalinina O, Kumacheva E: **Colloid crystal growth under oscillatory shear.** *Advanced Materials* 2000, **12**:110–112.
76. Smart L, Moore E: *Solid state chemistry: an introduction.* CRC Press; 2012.
77. Wolf K, te Lindert M, Krause M, Alexander S, te Riet J, Willis AL, Hoffman RM, Figdor CG, Weiss SJ, Friedl P: **Physical limits of cell migration: control by ECM space and nuclear deformation and tuning by proteolysis and traction force.** *The Journal of cell biology* 2013, **201**:1069–1084.
78. Tsurkan MV, Chwalek K, Levental KR, Freudenberg U, Werner C: **Modular StarPEG-Heparin Gels with Bifunctional Peptide Linkers.** *Macromolecular rapid communications* 2010, **31**:1529–1533.
79. Castro-Hernandez E, Gundabala V, Fernández-Nieves A, Gordillo JM: **Scaling the drop size in coflow experiments.** *New Journal of Physics* 2009, **11**:075021.
80. Kadow CE, Georges PC, Janmey PA, Beningo KA: **Polyacrylamide hydrogels for cell mechanics: steps toward optimization and alternative uses.** *Methods Cell Biol.* 2007, **83**:29–46.
81. Roberts JJ, Earnshaw A, Ferguson VL, Bryant SJ: **Comparative study of the viscoelastic mechanical behavior of agarose and poly(ethylene glycol) hydrogels.** *J. Biomed. Mater. Res. Part B Appl. Biomater.* 2011, **99**:158–69.
82. Arnott S, Fulmer A, Scott W, Dea I, Moorhouse R, Rees D: **The agarose double helix and its function in agarose gel structure.** *Journal of molecular biology* 1974, **90**:269–284.
83. Jiang W, Li M, Chen Z, Leong KW: **Cell-laden microfluidic microgels for tissue regeneration.** *Lab on a Chip* 2016, **16**:4482–4506.
84. Swift J, Ivanovska IL, Buxboim A, Harada T, Dingal PDP, Pinter J, Pajerowski JD, Spinler KR, Shin J-W, Tewari M, et al.: **Nuclear lamin-A scales with tissue stiffness and enhances matrix-directed differentiation.** *Science* 2013, **341**:1240104.

85. Mann C, Leckband D: **Measuring traction forces in long-term cell cultures.** *Cellular and Molecular Bioengineering* 2010, **3**:40–49.
86. Freudenberg U, Hermann A, Welzel PB, Stirl K, Schwarz SC, Grimmer M, Zieris A, Panyanuwat W, Zschoche S, Meinhold D, et al.: **A star-PEG-heparin hydrogel platform to aid cell replacement therapies for neurodegenerative diseases.** *Biomaterials* 2009, **30**:5049–5060.
87. Kievsky YY, Carey B, Naik S, Mangan N, ben-Avraham D, Sokolov I: **Dynamics of molecular diffusion of rhodamine 6G in silica nanochannels.** *J Chem Phys* 2008, **128**:151102.
88. Dolega M, Delarue M, Ingremeau F, Prost J, Delon A, Cappello G: **Cell-like pressure sensors reveal increase of mechanical stress towards the core of multicellular spheroids under compression.** *Nature Communications* 2017, **8**:14056.
89. Torquato S, Truskett TM, Debenedetti PG: **Is random close packing of spheres well defined?** *Physical review letters* 2000, **84**:2064.
90. Lagarias JC: *The Kepler Conjecture: The Hales-Ferguson Proof.* Springer Science & Business Media; 2011.
91. Bargiel M, Tory EM: **Packing fraction and measures of disorder of ultradense irregular packings of equal spheres. II. Transition from dense random packing.** 2001, [no volume].
92. Boothe T, Hilbert L, Heide M, Berninger L, Huttner WB, Zaburdaev V, Vastenhouw NL, Myers EW, Drechsel DN, Rink JC: **A tunable refractive index matching medium for live imaging cells, tissues and model organisms.** *eLife* 2017, **6**.
93. Petrie RJ, Yamada KM: **Fibroblasts Lead the Way: A Unified View of 3D Cell Motility.** *Trends in cell biology* 2015, **25**:666–674.
94. Sixt M: **Cell migration: fibroblasts find a new way to get ahead.** *The Journal of cell biology* 2012, **197**:347–349.
95. Liu Y-J, Le Berre M, Lautenschlaeger F, Maiuri P, Callan-Jones A, Heuzé M, Takaki T, Voituriez R, Piel M: **Confinement and low adhesion induce fast amoeboid migration of slow mesenchymal cells.** *Cell* 2015, **160**:659–672.
96. Rajagopalan P, Marganski WA, Brown XQ, Wong JY: **Direct comparison of the spread area, contractility, and migration of balb/c 3T3 fibroblasts adhered to fibronectin-and RGD-modified substrata.** *Biophysical journal* 2004, **87**:2818–2827.
97. Nardone G, Oliver-De La Cruz J, Vrbsky J, Martini C, Pribyl J, Skládal P, Pe\sl M, Caluori G, Pagliari S, Martino F, et al.: **YAP regulates cell mechanics by controlling focal adhesion assembly.** *Nature Communications* 2017, **8**:15321.
98. Paluch EK, Aspalter IM, Sixt M: **Focal Adhesion-Independent Cell Migration.** *Annual review of cell and developmental biology* 2016, **32**:469–490.
99. Tschumperlin DJ: **Fibroblasts and the ground they walk on.** *Physiology (Bethesda)* 2013, **28**:380–90.

100. Kubow KE, Horwitz AR: **Reducing background fluorescence reveals adhesions in 3D matrices.** *Nature cell biology* 2011, **13**:3.
101. Fraley SI, Feng Y, Krishnamurthy R, Kim D-H, Celedon A, Longmore GD, Wirtz D: **A distinctive role for focal adhesion proteins in three-dimensional cell motility.** *Nature cell biology* 2010, **12**:598.
102. Lautscham LA, Kämmerer C, Lange JR, Kolb T, Mark C, Schilling A, Strissel PL, Strick R, Gluth C, Rowat AC, et al.: **Migration in confined 3D environments is determined by a combination of adhesiveness, nuclear volume, contractility, and cell stiffness.** *Biophysical journal* 2015, **109**:900–913.
103. Bergert M, Chandradoss SD, Desai RA, Paluch E: **Cell mechanics control rapid transitions between blebs and lamellipodia during migration.** *Proc. Natl. Acad. Sci. U.S.A.* 2012, **109**:14434–9.
104. Bergert M, Erzberger A, Desai RA, Aspalter IM, Oates AC, Charras G, Salbreux G, Paluch EK: **Force transmission during adhesion-independent migration.** *Nature cell biology* 2015, **17**:524–529.
105. Pebworth M-P, Cismas SA, Asuri P: **A novel 2.5 D culture platform to investigate the role of stiffness gradients on adhesion-independent cell migration.** *PLoS one* 2014, **9**:e110453.
106. Tinevez J-Y, Perry N, Schindelin J, Hoopes GM, Reynolds GD, Laplantine E, Bednarek SY, Shorte SL, Eliceiri KW: **TrackMate: An open and extensible platform for single-particle tracking.** *Methods* 2017, **115**:80–90.
107. Martin RM, Leonhardt H, Cardoso MC: **DNA labeling in living cells.** *Cytometry A* 2005, **67**:45–52.
108. Icha J, Weber M, Waters JC, Norden C: **Phototoxicity in live fluorescence microscopy, and how to avoid it.** *Bioessays* 2017, **39**.
109. Lukinavicius G, Blaukopf C, Pershagen E, Schena A, Reymond L, Derivery E, Gonzalez-Gaitan M, D'Este E, Hell SW, Gerlich DW, et al.: **SiR-Hoechst is a far-red DNA stain for live-cell nanoscopy.** *Nature communications* 2015, **6**:8497.
110. Grist SM, Chrostowski L, Cheung KC: **Optical oxygen sensors for applications in microfluidic cell culture.** *Sensors* 2010, **10**:9286–9316.
111. Kurokawa H, Ito H, Inoue M, Tabata K, Sato Y, Yamagata K, Kizaka-Kondoh S, Kadonosono T, Yano S, Inoue M, et al.: **High resolution imaging of intracellular oxygen concentration by phosphorescence lifetime.** *Scientific reports* 2015, **5**:10657.
112. Weyand B, Nöhre M, Schmäzlin E, Stolz M, Israelowitz M, Gille C, von Schroeder HP, Reimers K, Vogt PM: **Noninvasive oxygen monitoring in three-dimensional tissue cultures under static and dynamic culture conditions.** *BioResearch open access* 2015, **4**:266–277.

List of Figures

Figure 1: Schematic representation of various biochemical and mechanical parameters that characterize the complex *in vivo* microenvironment of cells. The parameters are interacting with each other and represent cues to guide cell function [6,14–18]. The orange-coloured parts illustrate the parameters affecting the mechanical properties of the microenvironment, whereas the blue-coloured parts label other factors guiding cell function. 3

Figure 2: “Structural features of protein gels (a) and synthetic hydrogels (b) at the micron-scale and nano-scale. Substrate mechanics influence matrix density, ligand availability (a) and hydrogel pore size (b).” Reprinted from [26]. 6

Figure 3: Scaffolds generated from hydrogel beads as building blocks with different mechanical properties but same diameter. 7

Figure 4: Agarose aliquot in Thermomixer..... 18

Figure 5: Magnetic stirrer in tube 18

Figure 6: Tube taped on magnetic mixer 18

Figure 7: Mixing of oil and agarose..... 18

Figure 8: After mixing for 20 min 18

Figure 9: Principle sketch of microfluidic droplet generator chip 19

Figure 10: Declaration of inlet and outlet..... 22

Figure 11: Centrifuge preparation. Place the lead in tissue paper into the tube holder, position the chamber on the tube holder with outlets at the bottom and stopper/reservoirs facing outwards. Take care that the holders are properly inserted into the centrifuge. 24

Figure 12: PMMA beads before (A) and after (B) first centrifugation. Beads are not sticking everywhere in the channel. 24

Figure 13: A) Position of chamber in holder before baking. B) First channel is unusable as the bottom part is melted together completely after baking (indicated by transparent appearance). The second channel is ok, but a few beads are in the channel above the stack. C) Perfect channel with no beads in the channel after baking. 25

Figure 14: Gap between channel wall and PMMA filter stack 26

Figure 15: Tilted chamber position during degassing..... 27

Figure 16: Two different experimental plans 27

List of Figures

Figure 17: Flow setup for long-term culture and over night imaging. A) Overview of flow setup for long-term culture. From left to right: medium bottle on stage, inlet tubing connected to flow chamber (on beige tissue), outlet tubing connected to peristaltic pump and waste beaker. B) Close up of medium bottle positioned in bottle holder on stage to avoid air bubbles in the flow setup. C, D) Flow setup that can be used to stack up hydrogel beads. Flow chamber is fixed in slide holder (from Microfluidic ChipShop) to ensure stable position during stacking, but also during cell culturing. E) For live-imaging, medium bottle in red flask holder is placed in the microscope incubator to keep temperature and CO₂ concentration constant. Tubings are placed carefully on the microscope stage (inlets facing towards the user) and the chamber itself is clamped onto the microscope stage to ensure stable positions during stage movement. Outlet tubing (facing to the back to the microscope arm) are connected to the peristaltic pump (F), which is also placed in the microscope incubator to limit tubing length. 30

Figure 18: Concepts to create 3D bead scaffolds. A) shows concept of cell culture inserts where the filter at the bottom serves as barrier to block beads. B) shows a flow chamber with introduced filter in the outlet that serves as barrier to block beads. 32

Figure 19: ThinCert™ from greiner bio-one. Image from <https://shop.gbo.com/en/row/products/bioscience/cell-culture-products/thincert-cell-culture-inserts/> 33

Figure 20: Adapted biofilm flow chambers as potential scaffold devices (design based on [54]. A) Flow chambers with different ways of introducing filter pieces by gluing. B) Flow chamber for cellulose fibre filter introduction. Technical drawings with exact dimensions can be found in Appendix A..... 33

Figure 21: Design and optimization steps during development of scaffold device. Shown devices represent concepts and assemblies, but not in their correct scales (technical drawings can be found in the appendix). A is the adapted biofilm flow chamber manufactured by PTZ-Prototypenzentrum Dresden GmbH. B - E show different designs produced by envisionTEC GmbH. F shows the commercially available flow chamber "ibidi μ-Slide VI^{0.4}". Technical drawings of A and E with exact dimensions can be found in Appendix A..... 34

Figure 22: Schematic diagram of cross-section of ibidi μ-Slide VI^{0.4} (channel width B , channel height H_1 , bottom height H_2) with oxygen diffusion parameters (initial oxygen concentration c_0 , ambient partial pressure of oxygen p_g , mole fraction solubility for oxygen in water X_{O_2} , diffusion coefficient D_{O_2} and permeability of plastic bottom P_{O_2}), inward flux $N_{O,c}$ and oxygen consumption rate R_i 35

Figure 23: Simulation of oxygen concentration (mol/m³) with cell maintenance. A) Evolution of oxygen concentration over time and channel height (μm) with D_1 , 20 000 cells and P . B) Evolution of oxygen concentration over time for a random point within the channel with D_1 , 20 000 cells and P . C) Starting point ($t = 0$ s) and end point ($t = 72 000$ s) of oxygen concentration evolution over time for complete channel cross-section. D) Evolution of oxygen

List of Figures

concentration over time and channel height (μm) with $D_{1,\text{small}}$, 20 000 cells, and P. Colour scales are for all images the same.	38
Figure 24: Simulation of oxygen concentration (mol/m^3) over time and channel height with cell growth implemented for different diffusion constants (D), cell numbers (n) and permeabilities (P). A) D_1 , n, P. B) D_2 , n, P. C) $D_{1,\text{small}}$, n, P. D) D_1 , 2n, P. E) D_1 , n/2, P. F) D_1 , n, P_1 . G) D_1 , n, P_2 . H) D_1 , n, P_3 . All parameters were defined in Table 9.....	40
Figure 25: Principle of creating a regular scaffold in the chosen device.....	41
Figure 26: Refractive index matching of 17 μm PMMA beads with 2,2-Thiodiethanol water mixtures with defined refractive index n_D . The refractive index of PMMA beads is defined by the switch of bead appearance from dark to bright in phase contrast. Scale bar 50 μm	43
Figure 27: Stable regular PMMA bead scaffolds stained with Rhodamine-6G-TDE solution. 50 μm PMMA beads were used to create these scaffolds. In the close-up six random stacks are shown, demonstrating also small defects and grain boundaries in regular scaffolds. The right end demonstrates irregular structures resulting from the fibre filter. Scale bar 2000 μm	44
Figure 28: Work flow of regularity characterization a) Amount of available data of a bead stack per channel. b) Work flow of Fiji script to obtain all necessary data from fluorescent microscopy images of the z-stacks. c) Work flow of the Python script (written by Paul Müller) to obtain the fitting parameter (variance σ and amplitude A) of the first 7 peaks (red and green peaks) that are used to characterise the regularity of perfectly ordered bead stacks.1.....	45
Figure 29: Chamber position in slide holder to generate regular scaffolds.....	46
Figure 30: Effect of sedimentation time and ultrasonic treatment time on PMMA bead stack regularity, where a value of 7 represents a perfectly ordered bead stack. Median distribution of n bead stacks from 2-3 independent experiments are analysed by Mann-Whitney Test. The boxes represent 25% to 75% interquartile of the distribution. n represents the number of analysed stacks. * $p < 0.05$, ** $p < 0.01$. Whiskers are defined as 1.5x interquartile regime and outliers as data points outside the whiskers.....	46
Figure 31: Generation of gap between PMMA bead (50 μm) scaffold and channel wall over time by bead shrinkage, when replacing EtOH with PBS. Scale bar: 200 μm	47
Figure 32: Principle of generating bead scaffold with different stiffness (E) and the applied filter layers (i.e. cellulose fibre filter, PMMA bead filter and agarose bead filter).	48
Figure 33: Theoretical pore size dimensions in regular colloidal crystals with the largest sphere (red) that fits into the void. A) Tetrahedral pore. B) Octahedral pore.....	49
Figure 34: Mesofluidic approach to produce hydrogel beads with a Co-Flow device at the Institute for Polymer Research (IPF), Dresden. Image courtesy: Steffen Vogler.....	50

List of Figures

Figure 35: Hydrogel bead production with microfluidic approach (i.e. flow-focusing PDMS-microfluidic device). A) Demonstration of flow focussing principle. Scale bar: 100 μm . B) Production frequency and droplet diameter depend on the used pressure of the oil phase at constant hydrogel flow pressure (700 mBar) (scale bar in inset: 50 μm). Reprinted from [48].
..... 50

Figure 36: Ultra-low gelling point agarose stiffness and effects influencing it. A) Temperature effect on ULGP agarose stiffness (0.5% ULGP agarose in PBS). Young's Modulus was corrected for mean bead diameter. B) Oil effect on ULGP agarose stiffness (2% ULGP agarose in PBS). Young's Modulus was corrected individually for each bead diameter. Number of measured beads = n; Box plot whiskers = SD. C) Sketch of molecular agarose transport over the interface "oil – droplet" leading to a decrease in agarose concentration followed by a decrease in stiffness. (correspondence with Dr. Julian Thiele, IPF).
..... 53

Figure 37: Polyacrylamide (PAAm) hydrogel beads can cover a wide range of stiffness (determined by AFM measurements). A) Young's Modulus with varied total monomer concentration (c_T) from 5.9% to 11.8% (n stated in graph, reproduced from [48]). B) Young's Modulus of different PAAm hydrogel bead batches (c_T varied) functionalized with PLL-Cy5 (0.3 mg/mL and $\sim 70 \times 10^6$ beads) (n = 34), data points as dots in graph. Whiskers were defined as 1.5x interquartile regime and outliers as data points outside the whiskers. 54

Figure 38 Correlation between PLL-Cy5 fluorescence intensity and PAAm-PLL-Cy5 hydrogel bead stiffness determined by RT-fDC measurement. A – C) Confocal images of PAAm hydrogel beads (A) 7.9% c_T , B) 9.9% c_T , C) 11.8% c_T) functionalized with PLL-Cy5 (0.3 mg/mL and $\sim 70 \times 10^6$ beads). Image acquisition was done with same settings for all confocal images. Scale bar: 25 μm . D) Histogram of Young's Modulus distribution (determined with RT-fDC) with fitted normal distribution for respective PAAm composition. E) Histogram of fluorescence intensity distribution (determined with RT-fDC) with fitted normal distribution for respective PAAm composition. RT-fDC scatter plots – FL-Maxima vs Young's Modulus. F RT-fDC scatter plots (Young's Modulus vs. fluorescence intensity) of all three PAAm hydrogel bead samples (flow rates: 7.9% c_T : 0.024 $\mu\text{L/s}$; 9.9% c_T : 0.08 $\mu\text{L/s}$; 11.8% c_T : 0.12 $\mu\text{L/s}$) 55

Figure 39: Principle sketch of possible cell culture experiments in hydrogel bead scaffolds (stacks) where cells are introduced as layer between hydrogel bead stacks either with different stiffness or the same stiffness. 56

Figure 40: Generation of covalent starPEG heparin hydrogel beads scaffolds. A) continuous flow setup to generate hydrogel bead scaffolds. B) Orthogonal view of obtained hydrogel bead scaffold with large hydrogel beads stained with Rhodamine-6G ($\gamma = 1$). C) Orthogonal view of obtained hydrogel bead scaffold with intermediate hydrogel beads stained with Rhodamine-6G ($\gamma = 0.5$). Scale bars: 200 μm .
..... 57

Figure 41: 3D hydrogel bead scaffolds made from non-covalent starPEG heparin hydrogel beads. A) Orthogonal view of hydrogel bead scaffold stained with Rhodamine-6G (2.5 mM (KA)₇-RGDSP-starPEG and 0.5 mM heparin). Scale bar: 100 μm . B) Orthogonal view of

List of Figures

hydrogel bead scaffold (2.5 mM (KA)₇-RGDSP-starPEG+fluorescein and 0.25 mM heparin). White arrow indicates fading out of the scaffold. Scale bar: 300 μ m. 57

Figure 42: Sketch of fading out of hydrogel bead scaffold after stack generation. A) Scaffolds are generated while the chamber is in a vertical position. B) Scaffolds fade out after chamber is positioned again horizontally. 58

Figure 43: Orthogonal views of 3D hydrogel bead scaffolds made from ultra-low gelling point agarose beads. A) 2% ULGP agarose functionalized with Alexa-488 nm. B) 1% ULGP agarose functionalized with Cy2. Scale bar: 100 μ m. 59

Figure 44: 3D hydrogel bead scaffolds made from PAAm hydrogel beads. A) Bright field image of uncoated PAAm hydrogel bead scaffold ($c_T = 13.8\%$; light grey) with NIH3T3/GFP cell clusters incorporated (dark grey clusters) in the scaffold structure. Scale bar: 100 μ m. B) and C) Confocal slices of PLL-Cy5 functionalized PAAm hydrogel bead scaffolds ($c_T = 11.8\%$). Scale bars: 25 μ m (B) and 50 μ m (C). 60

Figure 45: Characterization and comparison of regular, well stained PMMA bead scaffolds and irregular stained PAAm hydrogel bead scaffolds. Volume fractions (%) of binary 3D confocal stacks were determined by FIJI plugin "Voxel counter" A) Two exemplary images of a highly regular PMMA scaffold at different z-positions and with volume fraction of 76.9%. Scale bar: 100 μ m. B) Two exemplary images of a regular PMMA scaffold with defects at different z-positions and a volume fraction of 63.71%. Scale bar: 100 μ m. C) and D) Exemplary confocal images at different z-positions and respective processed binary images of a regular PAAm hydrogel bead scaffold (functionalized with PLL-Cy5) (C and D are from same stack). Scale bar: 25 μ m. E) Volume fractions of different PMMA bead scaffolds (A, B), irregular PAAm bead scaffolds (n = 6) and regular PAAm bead scaffolds (n = 9, including C). 74% illustrates the maximal volume fraction that can be achieved based on theory [89,90]. Whiskers were defined as standard deviation and outliers as data points outside the whiskers. 62

Figure 46: NIH3T3/GFP (green) survival over 4 days in PAAm hydrogel beads with different stiffness ($c_T = 7.9\%$, 9.9% and 11.8% respectively) and functionalized with PLL-Cy5. Dead cells were stained with 5 μ g/mL propidium iodide. Maximum projections of representative confocal microscopy stacks, same settings for all images. Scale bar: 100 μ m. 64

Figure 47: NIH3T3/GFP (green) network formation in PAAm hydrogel bead scaffolds functionalized with PLL-Cy5 (magenta) and different stiffness ($c_T = 7.9\%$, 9.9% and 11.8% respectively). 3D projections. Day 4 does not show beads as the fluorescence intensity was too low to be detected. Dead cells were stained with 5 μ g/mL propidium iodide (red). 65

Figure 48: NIH3T3/GFP (green) in 3D PAAm hydrogel bead scaffold ($c_T = 9.9\%$) functionalized with PLL-Cy5 (magenta) after 24 h. Examples of deformed hydrogel beads are indicated with white arrows. Confocal microscopy slice; scale bar: 100 μ m. 66

Figure 49: NIH3T3/GFP fibroblast migrating through PAAm hydrogel bead scaffold ($c_T = 11.8\%$) functionalized with PDL. Maximum projection and overlay of all 47 time points

List of Tables

(time increment 20 min) with yellow line illustrating migration track as well as individual maximum projections for two selected time points. Scale bar: 25 μm 67

Figure 50: NIH3T3/GFP fibroblasts migrating through 3D PAAm hydrogel bead scaffolds functionalized with PLL-Cy5 (magenta) over 15 h at scaffold interface: $c_T = 9.9\%$ to 11.8% (dashed line) A) Maximum projection of fibroblast fluorescence signal for each time point and overlay of all time points (grey; time increment 15 min). $t = 0$ min: green; $t = 912$ min: red. Scale bar: 50 μm . B, C) Confocal slices of close ups of indicated areas in A) with fibroblasts (green) migrating through 3D PAAm hydrogel bead scaffold (magenta). Scale bar: 20 μm . . 68

Figure 51: Maximum projection of NIH3T3/GFP (green) fibroblasts migrating in amoeboid-like migration mode through PAAm hydrogel bead stack ($c_T = 13.8\%$, $E = 6.6$ kPa) within a total imaging time of 15 h. Dead cells were stained with 5 $\mu\text{g}/\text{mL}$ PI (red). Scale bar: 50 μm 70

List of Tables

Table 1: Summarized advantages and disadvantages of natural and synthetic hydrogels as scaffolds for 3D <i>in vitro</i> cell culture models. Lee et al. listed these for individual hydrogels [8,25,28].....	4
Table 2: General materials.....	9
Table 3: Solutions.....	10
Table 4: Equipment.....	10
Table 5: Material for fluorescent labelling of ULGP agarose	16
Table 6: Material for polydisperse ULGP agarose beads	17
Table 7: Material to create 3D hydrogel bead scaffolds.....	22
Table 8: Design considerations for 3D hydrogel bead scaffold device	32
Table 9: Parameters for oxygen simulation performed in COMSOL	37
Table 10: Rigid beads and their corresponding refractive index n.....	42
Table 11: Investigation of hydrogel bead qualification as scaffold building blocks for covalent starPEG heparin (produced at IPF [77]), non-covalent starPEG heparin (material provided from Dr. Robert Wieduwild, BCube, Dresden [51]), ultra-low gelling point agarose and polyacrylamide.....	51

Eigenständigkeitserklärung

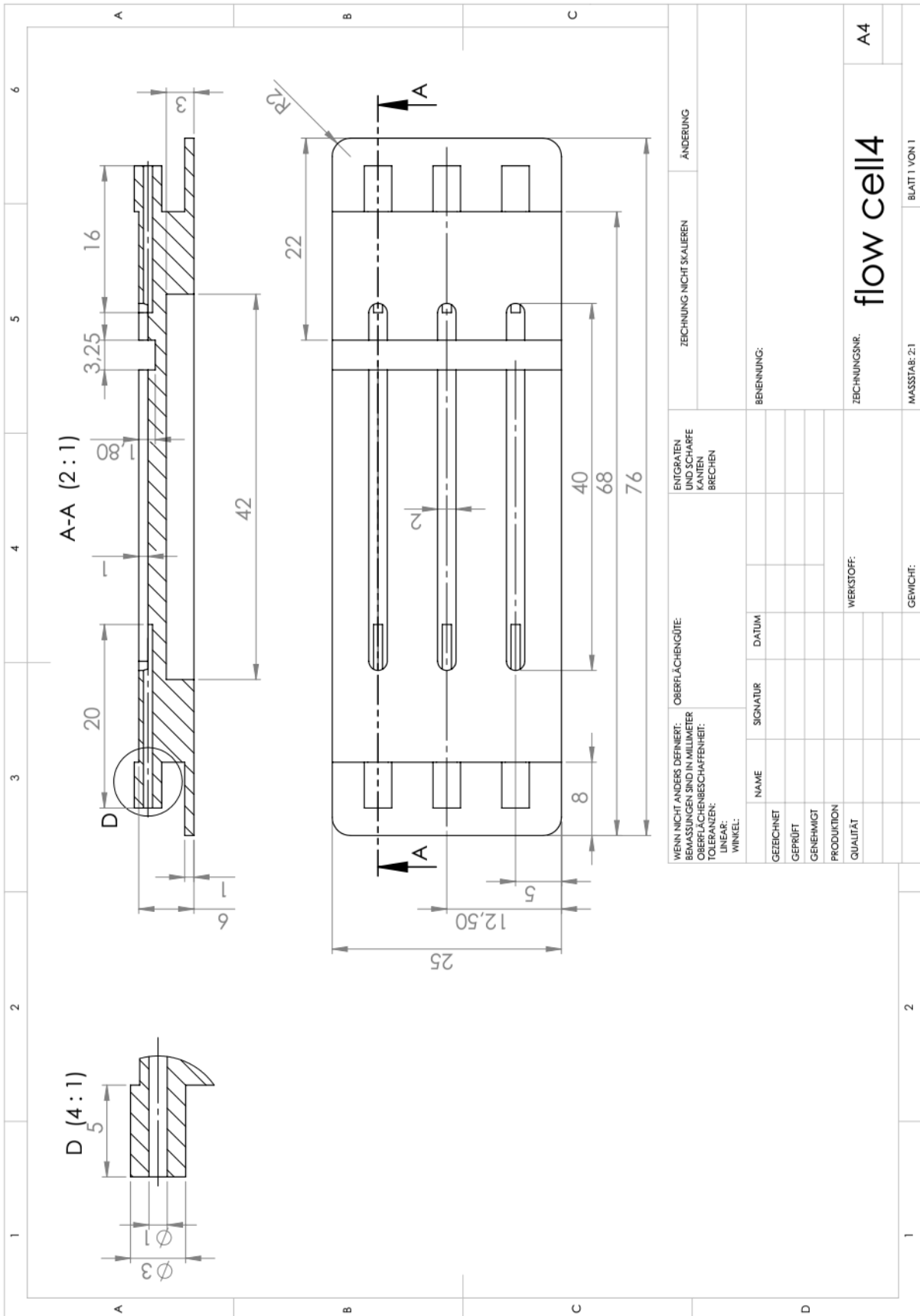
Hiermit versichere ich, dass ich die vorliegende Arbeit ohne unzulässige Hilfe Dritter und ohne Benutzung anderer als der angegebenen Hilfsmittel angefertigt habe; die aus fremden Quellen direkt oder indirekt übernommenen Gedanken sind als solche kenntlich gemacht. Weitere Personen waren an der geistigen Herstellung der vorliegenden Arbeit nicht beteiligt. Insbesondere habe ich nicht die Hilfe eines kommerziellen Promotionsberaters in Anspruch genommen. Dritte haben von mir keine geldwerten Leistungen für Arbeiten erhalten, die in Zusammenhang mit dem Inhalt der vorgelegten Dissertation stehen. Die Arbeit wurde bisher weder im Inland noch im Ausland in gleicher oder ähnlicher Form einer anderen Prüfungsbehörde vorgelegt und ist auch noch nicht veröffentlicht worden. Die gültige Promotionsordnung wird anerkannt.

I hereby declare that the present work has been produced without undue help of third parties and without use of any other than the indicated resources. The thoughts stemming directly or indirectly from external sources have been indicated as such. Additional persons were not involved in the intellectual production of the present work. In particular, I did not enlist the help of a commercial consultant. Third parties have not received monetary benefits from me connected with the content of the present thesis. This work has not been submitted to another examination board domestically and abroad in equal or similar form and has not been published yet. The doctorate regulations are respected.

Katrin Wagner

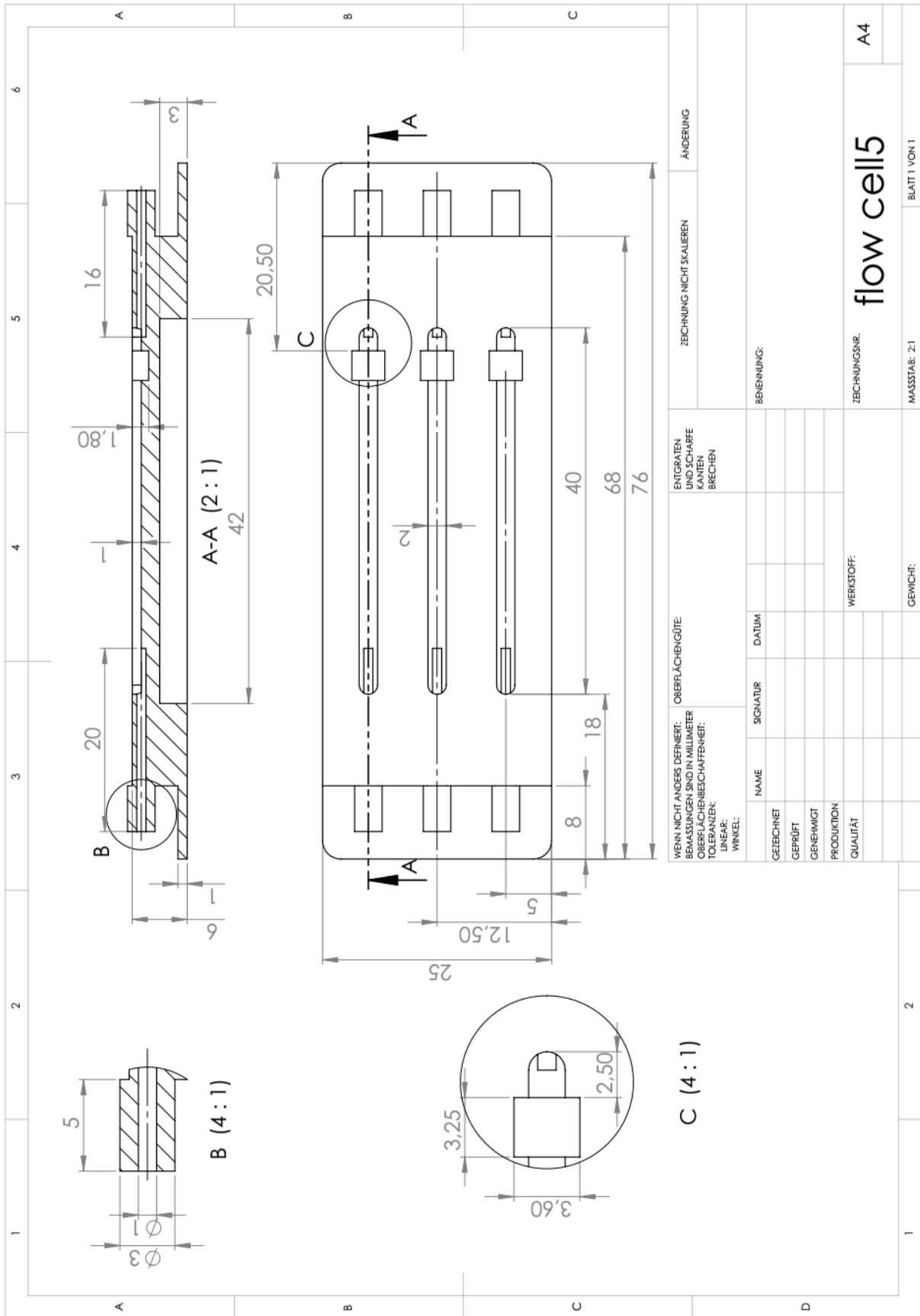
Dresden, 13.04.2018

Appendix A

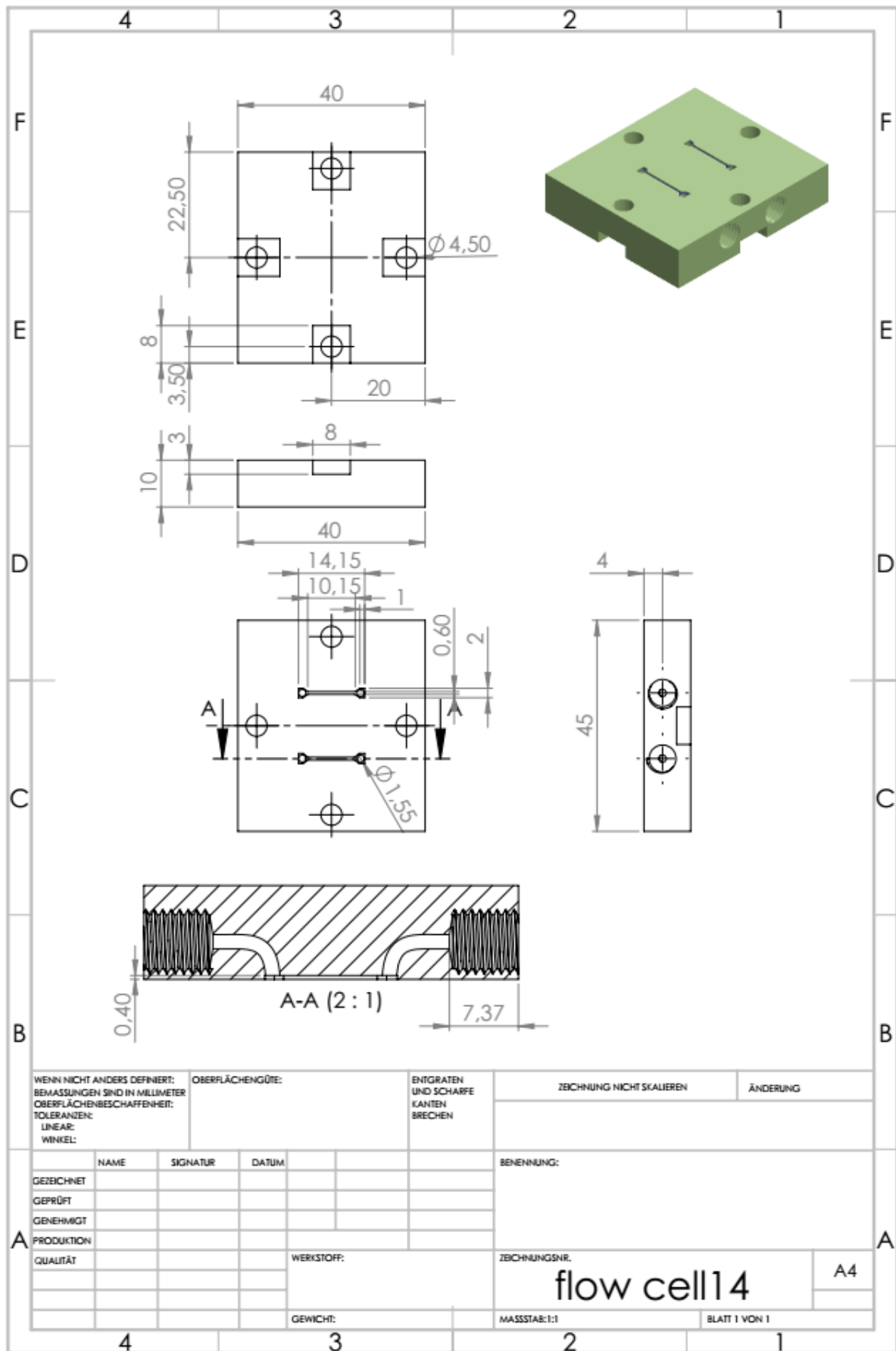


WENN NICHT ANDERS DEFINIERT: BEMASSUNGEN SIND IN MILLIMETER		OBERFLÄCHENGÜTE:		ENTGRATEN UND SCHÄRFE KANTEN BRECHEN		ZEICHNUNG NICHT SKALIEREN		ÄNDERUNG	
OBERFLÄCHENBESCHAFFENHEIT:									
TOLERANZEN:									
LÄNGE:									
WINKEL:									
NAME		SIGNATUR		DATUM		BENENNUNG:			
GEZEICHNET									
GEPRÜFT									
GENEHMIGT									
PRODUCTION									
QUALITÄT									
				WERKSTOFF:		ZEICHNUNGSNR.:		A4	
						flow cell4			
						MASSTAB: 2:1		BLATT 1 VON 1	
						GEWICHT:			

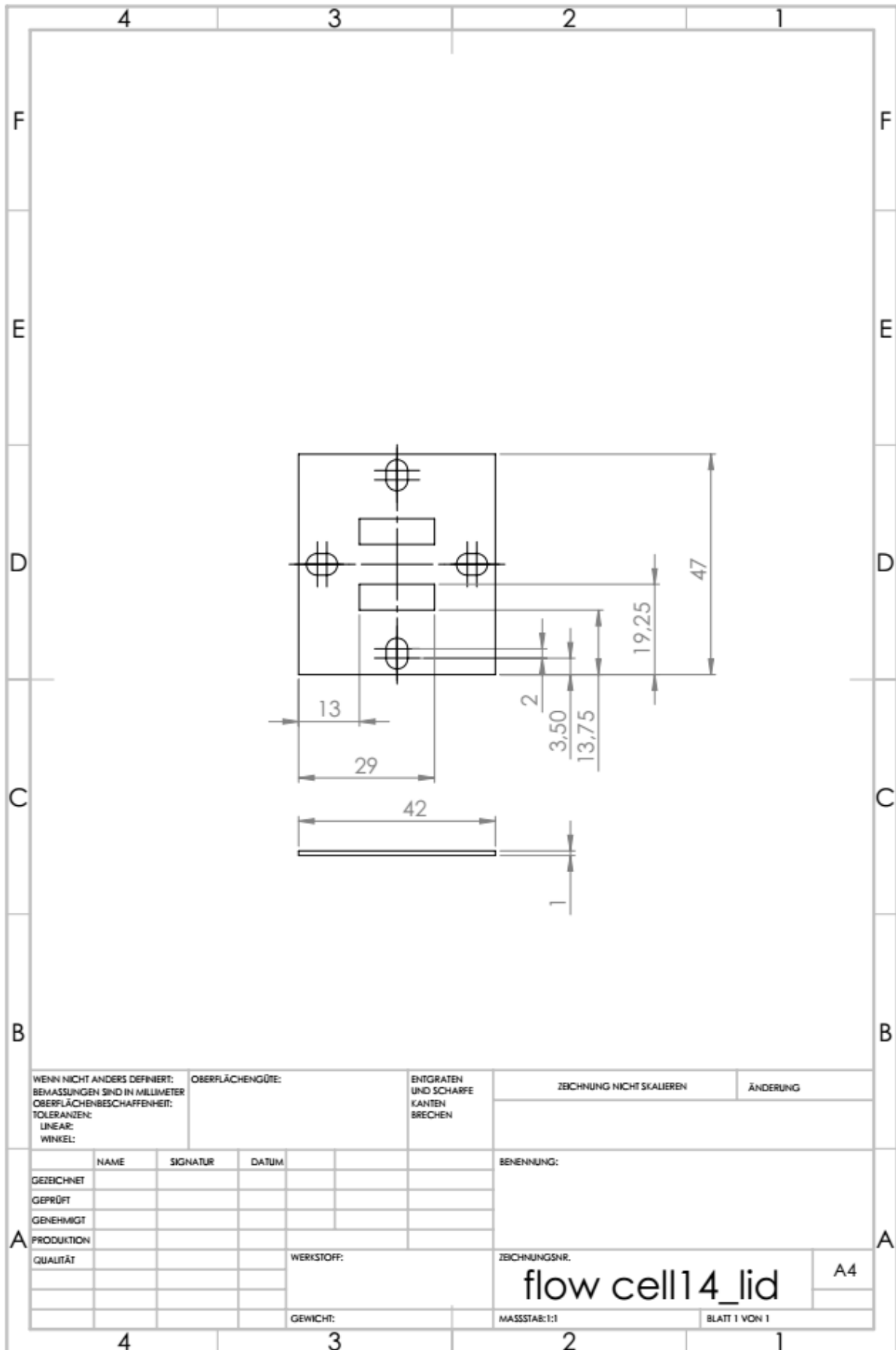
Appendix A



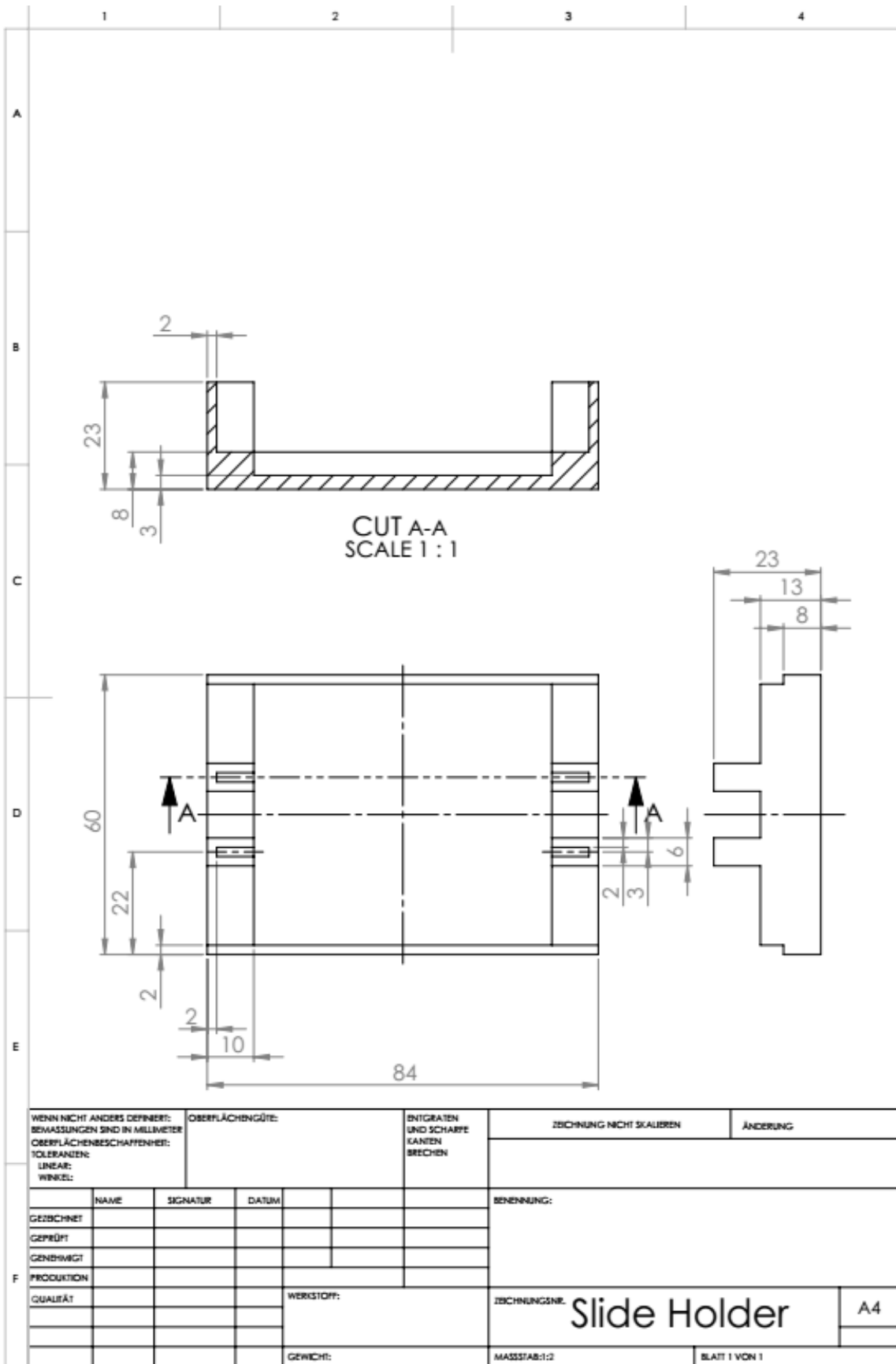
Appendix A



Appendix A



Appendix A



Appendix B

FIJI macro for FFT analysis maxima:

```
run("FFT Options...", "fft complex");
run("Set Measurements...", " shape redirect=None decimal=1");
input="E:\\folder of input data \\";
output="E:\\folder for output data\\";

setBatchMode(true);
list=getFileList(input);
for(i=0; i<list.length; i++){
    open(input+list[i]);
    run("Set Scale...", "distance=0 known=0 pixel=1 unit=pixel"); //scale in pixel and not in
    µm. results defaults in Phytton program
    stacksize=nSlices;
    for (j=1; j<=stacksize; j++) {
        run("Next Slice [>]");
        resetMinAndMax();
        run("Enhance Contrast", "saturated=0.35");
        run("FFT");
        selectWindow("Complex of "+list[i]);
        saveAs("Text Image", output+list[i]+"_"+j+"_FFT_real");
        run("Next Slice [>]");
        saveAs("Text Image", output+list[i]+"_"+j+"_FFT_imag");
        close();
        selectWindow("FFT of "+list[i]);
        run("Find Maxima...", "noise=25 output=[Point Selection] exclude");
        run("Measure");
        close();
        selectWindow("Results");
        saveAs("Text", output+list[i]+"_"+j+"_results");
        selectWindow("Results");
        run("Clear Results"); //necessary to save only the actual measurements from
        the actual FFT image
    }
}
close();
setBatchMode(false);
```

Python script to determine regularity of PMMA bead scaffolds

HexPeakAmpl.py

Analysis of beads. Given are Fourier transform ("*_FFT_real/imag.txt") and the position of peaks ("*_results.txt"). Assuming a hexagonal lattice and interpolating missing peak locations, finds Amplitude and standard deviation of Gaussian fit to every peak in the image (even those not detected).

What this script does:

1. Make a list of all files ending with "_results.txt" in this directory
-load_peak_loc
2. From each file, use the position of peaks to extrapolate for all positions on a hexagonal lattice. In lattice fitting, weights are used that are linear proportional to their distance from the origin.
-find_lowest_7 (the center peaks)
If these are not found correctly (also because the particle detection algorithm might not have succeeded), tune the `STANDARD_R` and `STANDARD_PHI` parameters with expected values.
-find_grid (fit a hexagonal lattice to the peaks using magic)
-make_hex_grid (lattice-creator)
-reduce_lattice (fit function, has `weighting` parameter)
-zero_modulus (like modulus, but with abs())
3. Identify the lattice peaks with the particle detected peaks and distribute ids.
-match_peaks
4. Find the actual center of each lattice point using center of mass COM and then fit a gaussian on the radial pixel profile for each peak. (This takes the longest time)
-load_FFT (loads FFT data from *_FFT_real.txt and *_FFT_imag.txt)
-center_of_mass
-fit_gauss_to_peak
-fit_gauss_to_multiple_peaks
5. Exported files are:
*_bead_image.png (The inverse (disc-filtered) Fourier transform)
*_peak_plot.png (A plot of the peaks in Fourier space)
- black crosses: particle-detected peaks
- blue circles: hexagonal grid
- black circles with white interior: COM peaks from lattice
*_all_peaks.txt (Full output of all peaks)
id
lattice_x : lattice x coordinate
lattice_y : lattice y coordinate
part_det_dx : distance between lattice point and particle (x)
part_det_dy : distance between lattice point and particle (y)
COM_dx : distance between lattice point and COM (x)

Python script to determine regularity of PMMA bead scaffolds

COM_dy : distance between lattice point and COM (y)
sigma : standard deviation of Gauss fit
amplitude : amplitude of Gauss fit
offset : zero-offset for Gauss fit

Author: Paul Müller

Version: 0.3.9

Changelog

0.3.9

- do not use matplotlib "Agg" renderer by default

"""

```
from __future__ import division, print_function
```

```
import gc
import matplotlib
from matplotlib import pylab as plt
import numpy as np
import os
from scipy import optimize as spopt
import sys
import warnings
```

```
# Is used if not (STANDARD_R - R_PM < R0 < STANDARD_R + R_PM)
STANDARD_R = 14.9
R_PM = 1.0
STANDARD_PHI = np.pi/4
```

```
def center_of_mass(a, threshold = 0.2, inverted=False):
```

```
    """ Find weighted center coordinates of array.
```

```
    Paramteres
```

```
    -----
```

```
    a : ndarray
        input array
    threshold : float
        threshold b/w min and max of array for weighting
    inverted : bool
        compute the center of mass of inverted image
```

```
    Returns
```

```
    -----
```

```
    (x,y) : tuple
        center coordinates
```

Python script to determine regularity of PMMA bead scaffolds

```
"""
b = a.copy()
if inverted:
    b *= -1
b -= np.min(b)

b[np.where(b <= 0.2*b.max())] = 0

x = np.arange(b.shape[1]).reshape(1,-1)
y = np.arange(b.shape[0]).reshape(-1,1)

btot = np.sum(b)
SPx = np.sum(x*b) / btot
SPy = np.sum(y*b) / btot

return (SPy,SPx)

def find_grid(peaks, N, no_offset=True, fname=None):
    """ given peaks, find lattice orientation and constant

    Returns list
    [xoffset, yoffset, rotation angle, R]
    """
    p = np.array(peaks)
    #p[:,1] -= N/2
    #p[:,2] -= N/2
    # Compute radius
    rad = np.sqrt(p[:,1]**2+p[:,2]**2)
    minids = find_lowest_7(rad)

    minids2 = np.unique(minids)

    if len(minids2) != len(minids):
        warnings.warn("{}: There are only {}".format(fname,len(minids2))+\
            "datapoints. Finding the grid is very unaccurate!")
        minids = minids2
        # turn off weighting in fitting the grid
        weighting = False
    else:
        weighting = True

    ## first approximation for lattice constant
    # first peak is the center peak
    # compute distance from all other peaks
    distances = np.zeros(len(minids)-1)
```


Python script to determine regularity of PMMA bead scaffolds

```
for i in range(1,len(minids)):
    distances[i-1] = np.sqrt( (p[minids[i],1] - p[minids[0],1])**2 +
                             (p[minids[i],2] - p[minids[0],2])**2 )
R0 = np.average(distances)

pc = np.zeros(p.shape)

# Move offset coordinates to center
if no_offset:
    pc = 1*p
else:
    (pc[:,1], pc[:,2]) = (p[:,1]-p[minids[0],1], p[:,2]-p[minids[0],2])

## first approximation for lattice angle
# compute all angles modulo PI/3
angles = np.zeros(len(minids)-1)
for i in range(1,len(minids)):
    angles[i-1] = np.arctan2((pc[minids[i],2]),
                            (pc[minids[i],1]) )
A0 = np.average(angles % (np.pi/3))

### ! R0 should stay around STANDARD_R for Katrins beads.

if R0 > STANDARD_R + R_PM or R0 < STANDARD_R - R_PM:
    warnings.warn("{}: I assume that the center peaks were not".format(fname)+\
                  " correctly detected in first stage."+ \
                  " Trying with `STANDARD_R`!")
    R0 = STANDARD_R
    A0 = STANDARD_PHI

pcr = np.zeros(p.shape)

# Rotate input coordinates with A0
(pcr[:,1], pcr[:,2]) = (p[:,1]*np.cos(A0) + p[:,2]*np.sin(A0),
                       - p[:,1]*np.sin(A0) + p[:,2]*np.cos(A0))

data = (pcr[:,1], pcr[:,2])

if no_offset:
    x0 = (0, 0, A0, R0)
else:
    x0 = (p[minids[0],1], p[minids[0],2], A0, R0)
##
#res = reduce_lattice(x0, data)

# brutal way of determining correct orientation
```

Python script to determine regularity of PMMA bead scaffolds

```
N = 200
ress = list()
minps = list()
angles = A0 + np.arange(N) * np.pi / N

for i in range(N):
    if no_offset:
        # no offset as of v. 0.3.1
        #x0 = (0, 0, angles[i], R0)
        x0 = (angles[i], R0)
    else:
        # no offset as of v. 0.3.1
        #x0 = (p[minids[0],1], p[minids[0],2], angles[i], R0)
        x0 = (angles[i], R0)
    with warnings.catch_warnings():
        warnings.simplefilter("ignore")
        minparms = spopt.leastsq(reduce_lattice, x0, (data,no_offset,weighting))
    res = reduce_lattice(minparms[0], data, weighting=weighting)
    ress.append(np.sum(res))
    minps.append(minparms)

idmin = np.argmin(ress)
theminsps = minps[idmin]

while theminsps[0][1] < STANDARD_R-R_PM:
    theminsps[0][1] *= 2
    warnings.warn("{}: I assume that the center peaks were not".format(fname)+\
        " correctly detected in second stage (fitting)."+\
        " Doubling lattice constant to {:.2f}!".format(theminsps[0][1]))

while theminsps[0][1] > STANDARD_R+R_PM:
    theminsps[0][1] /= 2
    warnings.warn("{}: I assume that the center peaks were not".format(fname)+\
        " correctly detected in second stage (fitting)."+\
        " Halving lattice constant to {:.2f}!".format(theminsps[0][1]))

print("...Found lattice. Residuals: worst={:.2f} best={:.2f}".format(
    np.max(ress), np.min(ress)))
print("...Lattice constant: {} 1/px".format(theminsps[0][1]))
print("...Lattice rotation: {} rad".format(theminsps[0][0]))

return theminsps[0]

def find_lowest_7(a):
    """ Find lowest seven numbers in array and return sorted ids
```

Python script to determine regularity of PMMA bead scaffolds

```
"""
b = a.copy()
ids = np.zeros(7, dtype=int)
for i in range(7):
    ids[i] = b.argmax()
    b[ids[i]] = b.max()+1

return ids

def fit_gauss_to_peak(image,x,y,R):
    """ Fit gaussian function on fraction of image

    (x,y) : coordinates in image
    R : cut-off radius

    Returns two tuples:
    1 : sigma0, N0, offset
    2 : x0, y0 (center of mass)
    """
    x,y = y,x
    N = len(image)
    X = np.arange(N)-N/2
    X = X.reshape((-1,1))
    Y = X.reshape((1,-1))
    data = image*((X-x)**2 + (Y-y)**2 < R**2)
    (x0,y0) = center_of_mass(data)

    #fig = plt.figure()
    #ax = fig.add_subplot(111, aspect=1)
    #ax.set_aspect("equal")
    #plt.imshow(data)
    #plt.show()

    # get radius of each pixel
    radii = list()
    values = list()

    coo = np.where( data != 0 )

    for i in range(len(coo[0])):
        xi = coo[0][i]
        yi = coo[1][i]
        r = np.sqrt( (xi-x0)**2 + (yi-y0)**2 )
        radii.append(r)
        values.append(data[xi,yi])
```

Python script to determine regularity of PMMA bead scaffolds

```
radii = np.array(radii)

# Fit gaussian to that radius.
Gauss = lambda p, r: p[2] + p[1]/np.sqrt(2*np.pi*p[0]**2) * np.exp(-r**2/(2*p[0]**2))
Minimize = lambda p, r: Gauss(p,r) - values

sigma0 = 2
offset = np.min(data)
N0 = np.max(data) - offset

p0 = (sigma0, N0, offset)
res = spopt.leastsq(Minimize, p0, (radii,))

if res[1] in [1,2,3,4]:
    parms = res[0]
    # no negative sigma
    parms[0] = abs(parms[0])
else:
    parms = [np.nan]*3

#plt.figure()
#plt.plot(radii, values, "kx")
#plt.plot(radii, values + Minimize(res[0], radii), "bo")
#radi2 = np.linspace(0, np.max(radii), 100)
#plt.plot(radi2, Gauss(res[0], radi2), "r-")
#print(x,y,x0-len(image)/2,y0-len(image)/2)
del data

return (parms, (y0-len(image)/2-y, x0-len(image)/2-x))

def fit_gauss_to_multiple_peaks(image, peaks, grid):
    """ Does what fit_gauss_to_peak does for many peaks

    peaks : array with 2nd column x and 3rd column y values
    grid : 4th element contains lattice constant

    """
    out = list()

    for i in range(len(peaks)):
        #for i in range(2,30):
            #print(i)
            print("...Fitting peaks - {:.2f}%".format((i+1)/len(peaks)*100), end="\r")
            sys.stdout.flush()
            with warnings.catch_warnings():
                warnings.simplefilter("ignore")
```

Python script to determine regularity of PMMA bead scaffolds

```
(parms, loc) = fit_gauss_to_peak(image,
                                peaks[i,1],peaks[i,2],grid[1]/2)
outval = list(peaks[i]) + list(loc) + list(parms)
out.append(outval)

print(".")
return np.array(out)

def load_FFT(fname, res=["_FFT_real.txt", "_FFT_imag.txt"]):
    """ Load FFT image
    """
    fr = open(fname+res[0], "r")
    datar = fr.readlines() # header
    # id, X, Y, Circ., AR, Round, Solidity, R, Theta
    fr.close()

    fi = open(fname+res[1], "r")
    datai = fi.readlines() # header
    # id, X, Y, Circ., AR, Round, Solidity, R, Theta
    fi.close()

    clist = []
    for i in range(len(datar)):
        clist.append(np.array(datar[i].split(), dtype=np.dtype(float))+
                    1j*np.array(datai[i].split(), dtype=np.dtype(float))
                    )

    carr = np.array(clist)

    if carr.shape[0] != carr.shape[1]:
        warnings.warn("Input FFT image is not square shaped.")

    return carr

def load_peak_loc(fname, res="_results.txt", filterrad=None, size=None):
    """ Peak coordinates (id, x, y) from *_results.txt files

    filterrad (float) defines a circle around freq=(0,0) of points
    that are kept. All others will be removed.

    size is the image size (row/column) of the fft image in pixels
    """
    f = open(fname+res, "r")
    data = f.readlines() # header
    data.pop(0)
```

Python script to determine regularity of PMMA bead scaffolds

```
# id, X, Y, Circ., AR, Round, Solidity, R, Theta

peaks = np.array([ (int(i.split()[0]),
                  float(i.split()[1]),
                  float(i.split()[2])) for i in data ])
f.close()

if size is not None:
    peaks[:,1] -= size/2
    peaks[:,2] -= size/2
else:
    warnings.warn("Did not center the peak coordinates."+
                "This might lead to alignment/filtering errors!")

if filterrad is not None:
    peaks = peaks[np.where(
        (peaks[:,1]**2 + peaks[:,2]**2) < (filterrad)**2)]

return peaks

def make_hex_grid(griddata, N):
    """ Return coordinates of hexagonal grid on square cart coord system

    Input data: [xoffset, yoffset, rotation angle, R]
    N is size of the image
    """
    # Create vertical coordinate list first

    (A, R) = griddata

    # no offset as of v. 0.3.1
    xoff = yoff = 0

    num = int(np.floor((2*N)/R))

    if num %2 == 0:
        num+=1

    # Coordinates for center vertical line
    y = R*np.linspace(-(num-1)/2, (num-1)/2, num, endpoint=True)
    x = 2*R*np.cos(np.pi/6)*np.linspace(-(num-1)/2, (num-1)/2, num, endpoint=True)

    # Coordinates for side lines
    y2 = y + R*np.sin(np.pi/6)
    x2 = x + R*np.cos(np.pi/6)
```

Python script to determine regularity of PMMA bead scaffolds

```
X,Y = np.meshgrid(x,y)
X2,Y2 = np.meshgrid(x2,y2)

## Rotate
Xr, Yr = X*np.cos(A) + Y*np.sin(A), -X*np.sin(A) + Y*np.cos(A)
X2r, Y2r = X2*np.cos(A) + Y2*np.sin(A), -X2*np.sin(A) + Y2*np.cos(A)

## Offset
Xro = Xr + xoff
X2ro = X2r + xoff

Yro = Yr + yoff
Y2ro = Y2r + yoff

#fig = plt.figure()
#ax = fig.add_subplot(111, aspect=1)
#ax.set_aspect("equal")
#plt.plot(Xro.flatten(), Yro.flatten(), ".")
#plt.plot(X2ro.flatten(), Y2ro.flatten(), ".")

coordx = np.array([Xro, X2ro]).flatten()
coordy = np.array([Yro, Y2ro]).flatten()

coo = np.zeros((len(coordx),2))
coo[:,0] = coordx
coo[:,1] = coordy

## Filter with image size
c = coo
d = c[np.where((c[:,0]**2 + c[:,1]**2) < (N/4)**2)]
return d

def match_peaks(peaks, coords, grid, struct=False):
    """ Create new array for all peaks with full information

    peaks : measured coordinates of peaks (id, x, y)
    coords : coordinates of hexagonal grid (x,y)
    grid : determined grid [xoffset, yoffset, rotation angle, R]

    Returns array (id, x, y, dx, dy) with length of `coords`
    First three rows describes peaks as in `peaks`. dx and dy are
    distances to the matched peaks in `coords`.

    struct: bool, return structured array
    """
```

Python script to determine regularity of PMMA bead scaffolds

```
out = list() #np.zeros((len(coords), 5))

# go through coords
rad = grid[1]/2

idcounter = np.max(peaks[:,0]) + 1

peakcounter = 0

for i in range(len(coords)):
    x = coords[i,0]
    y = coords[i,1]

    # find closest peak within Radius R/2
    a = (peaks[:,1]-x)**2 + (peaks[:,2]-y)**2
    minid = np.argmin(a)
    if a[minid] <= rad**2:
        dx = peaks[minid,1]-x
        dy = peaks[minid,2]-y
        idp = peaks[minid,0]
        peakcounter += 1
    else:
        dx = np.nan
        dy = np.nan
        idp = idcounter
        idcounter += 1
    out.append(( idp, x, y, dx, dy))
# out[i,0] = idp
# out[i,1] = x
# out[i,2] = y
# out[i,3] = dx
# out[i,4] = dy

dtype = [("id", int), ("x", float), ("y", float), ("dx", float), ("dy", float)]
arra = np.array(out, dtype = dtype)
arra.sort(order="id")

if len(peaks) > peakcounter:
    warnings.warn("A total number of {} peaks were not within".format(len(peaks) -
peakcounter)+\
        " the radius of a hex lattice point and will be ignored!")

if struct:
    return arra
else:
    return np.array(arra.tolist())
```


Python script to determine regularity of PMMA bead scaffolds

```
def reduce_lattice(parms, data, no_offset=True, weighting=True):
    """
    Map all points of a hexagonal lattice to one and return total
    mean square distance.

    For cartesian coordinates, calculate most-likely superposition in
    new discrete base (k,l,m) with s0, s1, and s2.

    s0 = R*(    0,    1)
    s1 = R*(cos(PI/6), sin(PI/6))
    s2 = R*(cos(PI/6), -sin(PI/6))

    As of version 0.3.1, the option `no_offset` does not do anything.
    Default is now no offset.

    If weighting is set to false, there will be boundaries for R between
    STANDARD_R - 2*R_PM and +2*R_PM.
    """
    (x, y) = data

    if weighting:
        weights = np.sqrt(x**2+y**2)
        weights -= np.min(weights)
        weights /= np.max(weights)
        weights = 1-weights
    else:
        weights = 1

    # As of version 0.3.1 we do not use offsets anymore
    #(xoff, yoff, angle, R) = parms
    (angle, R) = parms

    if weighting is False:
        # Set boundaries for R, because we have very few data points
        if R > STANDARD_R + 2*R_PM:
            R = STANDARD_R + 2*R_PM
        if R < STANDARD_R-2*R_PM:
            R = STANDARD_R-2*R_PM

    xoff = yoff = 0
    ## Correct for offset:
    if no_offset:
        (xc, yc) = (x,y)
    else:
        (xc, yc) = (x+xoff, y+yoff)
```

Python script to determine regularity of PMMA bead scaffolds

```
## Rotate lattice
xcr, ycr = ( xc*np.cos(angle) - yc*np.sin(angle),
            xc*np.sin(angle) + yc*np.cos(angle))

## Reduce in y-direction
ycrr = zero_modulus(ycr,R)

## Reduce in x-direction
xcrr = zero_modulus(xcr,2*R*np.cos(np.pi/6))

## compute distance of all coordinates from center point and four
## surrounding points (y-axis is symmetry axis).
##
## (x)
## 4 1
## 0
## 3 2
## (x)
##

rx = R*np.cos(np.pi/6)
ry = R*np.sin(np.pi/6)

# minimal distances from center 0
d0 = np.sqrt(xcrr**2 + ycrr**2) * weights
# minimal distances from corner 1
d1234 = np.sqrt((np.abs(xcrr)-rx)**2 + (np.abs(ycrr)-ry)**2) * weights
#d0 = (np.abs(xcrr) + np.abs(ycrr**2)) * weights
#d1234 = (np.abs(xcrr-rx) + np.abs(ycrr-ry)) * weights

D = np.array([d0,d1234])

return np.min(D, axis=0)

def zero_modulus(a,m):
    """ Compute modulus of array with values closest to zero
    """
    c = a % m
    c[np.where(c>m/2)] -= m
    return c

for line in __doc__.split("\n"):
    if line.startswith("Version:"):
        __version__ = line.split("Version:")[1].strip()
```

Python script to determine regularity of PMMA bead scaffolds

```
if __name__ == "__main__":
    mysysargs = {
        "numpeaks" : 0
    }

    for arg in sys.argv:
        if arg.count("=") == 1:
            arg = arg.split("=")
            if arg[0] == "numpeaks":
                mysysargs[arg[0]] = int(arg[1])
            else:
                print("UNKNOWN PARAMETER: {}".format(arg))

    doc = __doc__.split("\n")
    for line in doc:
        if line.startswith("Version:"):
            print("..." + line)
        elif line.startswith("Author:"):
            print("..." + line)

    DIR = os.path.split(os.path.realpath(__file__))[0]
    os.chdir(DIR)

    resid = "_results.txt"

    fs = os.listdir(DIR)
    files=list()
    for f in fs:
        if f.endswith(resid):
            files.append(f)
    #files.pop(0)
    for f in files:

        name = f.split(resid)[0]
        print("...processing file '{}'.format(name))
        fft = load_FFT(name)
        N=len(fft)

        peaks = load_peak_loc(name, filterrad=N/4, size=N)

        try:
            grid = find_grid(peaks, N=N, fname=os.path.split(name)[1])
        except TypeError:
            warnings.warn("Could not process {} - ".format(name)+\
                "probably because not enough peaks were detected.")
            # go to next file
```

Python script to determine regularity of PMMA bead scaffolds

```
continue

coords = make_hex_grid(grid, N=N)

newpeaks = match_peaks(peaks, coords, grid, struct=False)

## Plot image
im = np.fft.ifft2(np.fft.ifftshift(fft))
fig = plt.figure(dpi=150, figsize=(10,10))
ax = fig.add_subplot(121)
ax.set_title("original image")
ax.imshow(im.real, cmap=matplotlib.cm.gray_r, interpolation="nearest")

x = np.linspace(-N/2, N/2, N, endpoint=False)
x = x.reshape(-1,1)
y = x.reshape(1,-1)
fftfilt = fft*(x**2+y**2<=(N/4)**2)
im2 = np.fft.ifft2(np.fft.ifftshift(fftfilt))
ax2 = fig.add_subplot(122)
ax2.set_title("disc filter, max_freq={}".format(N/4))
fig.tight_layout(pad=1.0)

ax2.imshow(im2.real, cmap=matplotlib.cm.gray_r, interpolation="nearest",
           vmin=np.min(im.real), vmax=np.max(im.real))
fig.savefig(name+"_bead_image.png")

# Plot a ring filtered image, filtered out from the first peaks.
fmin = grid[1]*.9
fmax = grid[1]*1.1
fftfilt = fft*(x**2+y**2<=(fmax)**2)*(x**2+y**2>=(fmin)**2)
#fftfilt =
fft*(x**2<=fmax**2)*(y**2<=fmax**2)*(x**2>=(fmin)**2)*(y**2>=(fmin)**2)
im2 = np.fft.ifft2(np.fft.ifftshift(fftfilt))
ax2.set_title("ring filter, min_freq={:.2f}, max_freq={:.2f}".format(fmin,fmax))
fig.tight_layout(pad=1.0)
ax2.imshow(im2.real, cmap=matplotlib.cm.gray_r, interpolation="nearest")
fig.savefig(name+"_bead_image_bandpass_rescaled.png")
del im2, fig, ax2
plt.close()

#np.savetxt(name+"_all_peaks.txt",newpeaks,
#          fmt=["%04d", "%.4f", "%.4f", "%.4f", "%.4f"])
##          id   x   y   dx   dy
##          (particle detection)

# Sort peaks according to distance from center
```


Python script to determine regularity of PMMA bead scaffolds

```
plt.savefig(name+"_peak_plot.png")

# Cleanup
del fft, fftfilt, peaks, newpeaks, logfft, full_data
del fig, ax
plt.close()

gc.collect()
```

Excel macro to determine number of peaks for regularity analysis

Analysis.xlsm – Excel macros to work further on Regularity data analysis

Modul3 (saved as "excelmacro_7peaks_sigmadistribution.bas")

Private Sub Transform_7_peaks_txt_in_xls_determine_sigma_distribution()

'This file transfers the 7 peak.txt from the Fourier transformation into a .xls file, it adds the filename and determines the sigma distribution

'It adds the lattice constant and uses the amplitude as additional parameter

'It also takes into account, that the .txt is english style and the excel worked with in german style

Dim MyFolder As String

Dim myfile As String

Dim folderName As String

With Application.FileDialog(msoFileDialogFolderPicker)

.AllowMultiSelect = False

If .Show = -1 Then

folderName = .SelectedItems(1)

End If

End With

myfile = Dir(folderName & "*_7_peaks.txt")

Do While myfile <> ""

'open the txt.file and change decimal separator from english "," to german "." as the used Excel is in german language
Workbooks.OpenText Filename:=folderName & "\" & myfile, Origin:=xlMSDOS, StartRow:=1, DataType:=xlDelimited,
TextQualifier:= _

xlDoubleQuote, ConsecutiveDelimiter:=False, Tab:=True, Semicolon:=False, _

Comma:=False, Space:=False, Other:=False, DecimalSeparator=".", ThousandsSeparator=" ",

TrailingMinusNumbers:=True

'change the format of lattice_x and _y to numbers

Range("B4:C10").NumberFormat = "0"

'no screen update

Application.ScreenUpdating = False

'Insert Name of File

Range("K5").Select

DateiName = ActiveWorkbook.Name

ActiveCell.FormulaR1C1 = DateiName

'Determine Sigma Distribution

Range("L4").Select

ActiveCell.FormulaR1C1 = "x<=1"

Range("M4").Select

ActiveCell.FormulaR1C1 = "x<2"

Range("N4").Select

ActiveCell.FormulaR1C1 = "2<=x<3"

Range("O4").Select

ActiveCell.FormulaR1C1 = "3<=x<4"

Range("P4").Select

ActiveCell.FormulaR1C1 = "4<=x<5"

Range("Q4").Select

ActiveCell.FormulaR1C1 = "5<=x<10"

Range("R4").Select

ActiveCell.FormulaR1C1 = "10<=x<20"

Range("S4").Select

ActiveCell.FormulaR1C1 = "20<=x<30"

Range("T4").Select

ActiveCell.FormulaR1C1 = "x>=30"

Range("V4").Select

ActiveCell.FormulaR1C1 = "nan"

Range("W4").Select

ActiveCell.FormulaR1C1 = "sum"

Range("Y4").Select

ActiveCell.FormulaR1C1 = "x<2 + A<0"

Excel macro to determine number of peaks for regularity analysis

```
Range("Z4").Select
ActiveCell.FormulaR1C1 = "x<2 + A>0"
Range("AB4").Select
ActiveCell.FormulaR1C1 = "Lattice constant"
Range("L5").Select
ActiveCell.FormulaR1C1 = "=COUNTIF(R[-1]C[-4]:R[10050]C[-4], "<=1")"
Range("M5").Select
ActiveCell.FormulaR1C1 = _
    "=COUNTIF(R[-1]C[-5]:R[10050]C[-5], "<2")"
Range("N5").Select
ActiveCell.FormulaR1C1 = _
    "=COUNTIF(R[-1]C[-6]:R[10050]C[-6], "<3")-COUNTIF(R[-1]C[-6]:R[10050]C[-6], "<2")"
Range("O5").Select
ActiveCell.FormulaR1C1 = _
    "=COUNTIF(R[-1]C[-7]:R[10050]C[-7], "<4")-COUNTIF(R[-1]C[-7]:R[10050]C[-7], "<3")"
Range("P5").Select
ActiveCell.FormulaR1C1 = _
    "=COUNTIF(R[-1]C[-8]:R[10050]C[-8], "<5")-COUNTIF(R[-1]C[-8]:R[10050]C[-8], "<4")"
Range("Q5").Select
ActiveCell.FormulaR1C1 = _
    "=COUNTIF(R[-1]C[-9]:R[10050]C[-9], "<10")-COUNTIF(R[-1]C[-9]:R[10050]C[-9], "<5")"
Range("R5").Select
ActiveCell.FormulaR1C1 = _
    "=COUNTIF(R[-1]C[-10]:R[10050]C[-10], "<20")-COUNTIF(R[-1]C[-10]:R[10050]C[-10], "<10")"
Range("S5").Select
ActiveCell.FormulaR1C1 = _
    "=COUNTIF(R[-1]C[-11]:R[10050]C[-11], "<30")-COUNTIF(R[-1]C[-11]:R[10050]C[-11], "<20")"
Range("T5").Select
ActiveCell.FormulaR1C1 = "=COUNTIF(R[-1]C[-12]:R[10050]C[-12], ">=30")"
Range("V5").Select
ActiveCell.FormulaR1C1 = "=COUNTIF(R[-1]C[-14]:R[10050]C[-14], "nan")"
Range("W5").Select
ActiveCell.FormulaR1C1 = "=SUM(RC[-1]:RC[-10])"
'Use Amplitude as additional criterion for sigma < 2
Range("Y5").Select
ActiveCell.FormulaR1C1 = "=COUNTIFS(R[-1]C[-17]:R[10050]C[-17], "<2", R[-1]C[-16]:R[10050]C[-16], "<0")"
Range("Z5").Select
ActiveCell.FormulaR1C1 = "=COUNTIFS(R[-1]C[-18]:R[10050]C[-18], "<2", R[-1]C[-17]:R[10050]C[-17], ">0")"
'Copy value from lattice constant from A2 into F2 and copy value w/o unit into R5.
Range("F2").Select
ActiveCell.FormulaR1C1 = "=RIGHT(RC[-5], LEN(RC[-5])-19)"
Range("AB5").Select
ActiveCell.FormulaR1C1 = "=LEFT(R[-3]C[-22], LEN(R[-3]C[-22])-5)"
'save as excel file
ActiveWorkbook.SaveAs Filename:=folderName & "\" & Replace(myfile, ".txt", ".xls")
'use below 3 lines if you want to close the workbook right after saving, so you dont have a lots of workbooks opened
Application.DisplayAlerts = False
ActiveWorkbook.Close
Application.DisplayAlerts = True
myfile = Dir
Loop
Application.ScreenUpdating = True
End Sub

Private Sub variance_merge_all_distri_7peaks_data_in_one_file()
'this file merges all the distri_#_7peaks-data from the script above into Worksheet1 to analyse the sigma and amplitude further
On Error GoTo errExit
Dim WBQ As Workbook
Dim WBZ As Workbook
Dim varDateien As Variant
Dim lngAnzahl As Long
Dim lngLastQ As Long

Set WBZ = ActiveWorkbook
'Altdaten auf Zielblatt löschen
```


Excel macro to determine number of peaks for regularity analysis

```
WBZ.Worksheets(1).Range("A5:IV65536").ClearContents

varDateien = _
Application.GetOpenFilename("Datei (*.xls),*.xls", False, "Select file(s) (Bitte gewünschte Datei(en) markieren)", False, True)

With Application
    .ScreenUpdating = False
    .EnableEvents = False
    .Calculation = xlCalculationManual
End With
'K5 until AB is copied in the file
For lngAnzahl = LBound(varDateien) To UBound(varDateien)
Set WBQ = Workbooks.Open(Filename:=varDateien(lngAnzahl))
    lngLastQ = WBQ.Worksheets(1).Range("A65536").End(xlUp).Row
    WBQ.Worksheets(1).Range("K5:AB" & lngLastQ).Copy _
        Destination:=WBZ.Worksheets(1).Range("A" & WBZ.Worksheets(1).Range("A65536").End(xlUp).Row + 1)
WBQ.Close
Next

With Application
    .ScreenUpdating = True
    .EnableEvents = True
    .Calculation = xlCalculationAutomatic
End With

MsgBox "" & UBound(varDateien) & " files were merged.", 64

Exit Sub

errExit:
With Application
    .ScreenUpdating = True
    .EnableEvents = True
    .Calculation = xlCalculationAutomatic
End With

If Err.Number = 13 Then
MsgBox "No files selected"
    Else
MsgBox "Error occurs!" & vbCrLf _
    & "Fehlernummer: " & Err.Number & vbCrLf _
    & "Fehlerbeschreibung: " & Err.Description
End If

End Sub
```

Excel macro to determine number of peaks for regularity analysis

Modul4 (saved as "excelmacro_7peaks_absolute_lattice.bas")

```
Private Sub Transform_7_peaks_txt_in_xls_and_add_filename()
'This file transfers the 7 peak.txt from the Fourier transformation into a .xls file, it adds the filename and defines the absolute
'values for lattice_x and lattice_y. It also takes into account, that the .txt is english style and the excel worked with in german
style
    Dim MyFolder As String
    Dim myfile As String
    Dim folderName As String

    With Application.FileDialog(msoFileDialogFolderPicker)
        .AllowMultiSelect = False
        If .Show = -1 Then

            folderName = .SelectedItems(1)
        End If
    End With

    myfile = Dir(folderName & "\*_7_peaks.txt")

    Do While myfile <> ""
        'open the txt.file and change decimal separator from english "," to german "." as the used Excel is in german language
        Workbooks.OpenText Filename:=folderName & "\" & myfile, Origin:=xlMSDOS, StartRow:=1, DataType:=xlDelimited,_
        TextQualifier:=xlDoubleQuote, ConsecutiveDelimiter:=False, Tab:=True, Semicolon:=False, Comma:=False, Space:=False,
        Other:=False, DecimalSeparator=".", ThousandsSeparator=" ", TrailingMinusNumbers:=True
        'change the format of every cell to numbers
        Range("B4:D10").NumberFormat = "0"
        'Inserting a column at Column A
        Range("A1").EntireColumn.Insert

        'Insert Name of File
        Range("A5").Select
        Dateiname = ActiveWorkbook.Name
        ActiveCell.FormulaR1C1 = Dateiname

        'Inserting a column after lattice_x
        Range("D1").EntireColumn.Insert
        Range("D3").Select
        ActiveCell.FormulaR1C1 = "absolute lattice_x"

        'Inserting a column after lattice_y
        Range("F1").EntireColumn.Insert
        Range("F3").Select
        ActiveCell.FormulaR1C1 = "absolute lattice_y"

        'creating absolute values of lattice_x and lattice_y
        Range("D4").Select
        ActiveCell.FormulaR1C1 = "=ABS(RC[-1])"
        Selection.AutoFill Destination:=Range("D4:D10"), Type:=xlFillDefault
        Range("F4").Select
        ActiveCell.FormulaR1C1 = "=ABS(RC[-1])"
        Selection.AutoFill Destination:=Range("F4:F10"), Type:=xlFillDefault

        ' Remove duplicates from absolute lattice_x and absolute lattice_y
        Range("B5:M10").Select
        ActiveSheet.Range("$B$5:$M$10").RemoveDuplicates Columns:=Array(3, 5), Header _
            :=xlNo

        'save as excel file
        ActiveWorkbook.SaveAs Filename:=folderName & "\" & "distri_" & Replace(myfile, ".txt", ".xls")
        'use below 3 lines if you want to close the workbook right after saving, so you dont have a lots of workbooks opened
        Application.DisplayAlerts = False
        ActiveWorkbook.Close
        Application.DisplayAlerts = True
        myfile = Dir
    Loop
```

Excel macro to determine number of peaks for regularity analysis

```
Application.ScreenUpdating = True
End Sub

Private Sub merge_all_single_peaks_in_worksheet2()
'this file merges all single peaks (with the reduced peaks due to duplicates) from the above script in worksheet2
  On Error GoTo errExit
  Dim WBQ As Workbook
  Dim WBZ As Workbook
  Dim varDateien As Variant
  Dim lngAnzahl As Long
  Dim lngLastQ As Long

  Set WBZ = ActiveWorkbook
  'Altdaten auf Zielblatt löschen
  WBZ.Worksheets(2).Range("A2:IV65536").ClearContents

  varDateien = _
  Application.GetOpenFilename("Datei (*.xls),*.xls", False, "Select file(s) (Bitte gewünschte Datei(en) markieren)", False, True)

  With Application
    .ScreenUpdating = False
    .EnableEvents = False
    .Calculation = xlCalculationManual
  End With
  'A5 until M7 is copied in the file; (2) indicates worksheet 2 in analysis-file; last used cell in column by
  range("A65536").End(xlUp)..
  For lngAnzahl = LBound(varDateien) To UBound(varDateien)
  Set WBQ = Workbooks.Open(Filename:=varDateien(lngAnzahl))
  lngLastQ = WBQ.Worksheets(1).Range("A65536").End(xlUp).Row
  WBQ.Worksheets(1).Range("A5:M7" & lngLastQ).Copy _
  Destination:=WBZ.Worksheets(2).Range("A" & WBZ.Worksheets(2).Range("A65536").End(xlUp).Row + 3)
  WBQ.Close
  Next

  With Application
    .ScreenUpdating = True
    .EnableEvents = True
    .Calculation = xlCalculationAutomatic
  End With

  MsgBox "" & UBound(varDateien) & " files were merged.", 64
  Exit Sub

errExit:
  With Application
    .ScreenUpdating = True
    .EnableEvents = True
    .Calculation = xlCalculationAutomatic
  End With

  If Err.Number = 13 Then
  MsgBox "No files selected"
  Else
  MsgBox "Error occurs!" & vbCrLf _
  & "Fehlernummer: " & Err.Number & vbCrLf _
  & "Fehlerbeschreibung: " & Err.Description
  End If

  End Sub
```